ISSN: 2583-5459
Volume-1 Issue- 4
April, 2023

Journal of ISAS

An open access peer reviewed quarterly e-journal by
Indian Society of Analytical Scientists

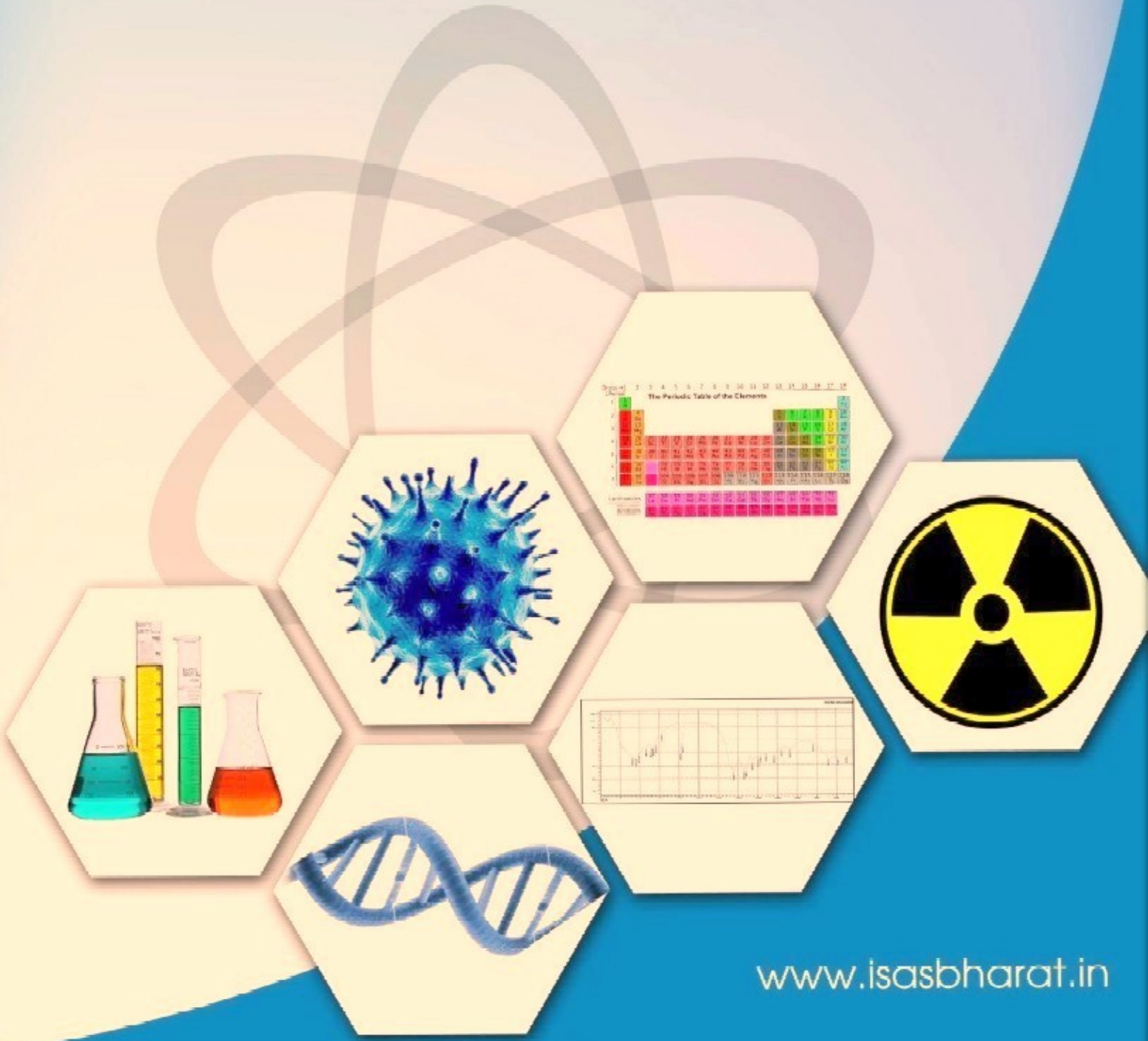

www.isasbharat.in

Journal of ISAS
An open access peer reviewed quarterly e-journal published by Indian Society of Analytical Scientists

Published by: Indian Society of Analytical Scientists (ISAS)
Address: C/o REDS, BARC, Mumbai 400085
Email: isasjournal@isasbharat.in

President ISAS: Dr. Raghaw Saran

J. ISAS

Cover page images- curtsey Pixabay.com

Instruction to Authors

- The Manuscript should be typed in **MS word** (times new roman) with **1.5 spacings** and **font size 12**
- The **title** of the paper should be clear and concise(**font size 14 and bold**), the first letter of each noun and adjective in the title must be in capital letter. It will be followed by names of authors(initials followed by surname) with their affiliation **(font size 12)**
- Corresponding author should be indicated by * with email ID
- The text should be divided into following sections:
- **Abstract : up to 300 words**
- **Key words: 5-6**
- **Introduction**
- **Experimental**
- **Results and Discussion**
- **Conclusions**
- **Acknowledgement**
- Figures and Tables should be before references with a caption **Figures:** Followed by **Tables:**
- **References**

- Divisions within the section should be indicated as subheadings
- The figures and tables should be numbered with Roman numerals and must be mentioned in the text at appropriate places
- Standard abbreviations for technical terms and journals should be used
- All constants should be expressed in **SI units**
- References should be numbered consecutively and should appear in the text as superscript at appropriate places.
- References should be in following pattern
  For research paper:
  Authors' initials and surname, Journal abbreviation, Volume, Page, Year.
  For book:
  Authors' initials and surname, Book name, Publisher, Place, Year.
  For proceedings:
  Authors' initials and surname Proceedings' of the conference name, place, Page, Month and Year.

- The paper is to be submitted in word file and PDF file to isasjournal@isasbharat.in
- After getting the acceptance of the paper, authors have to submit **signed copyright form and undertaking** before publishing the article

ISAS

Indian Society of Analytical Scientists

Message from President ISAS

It is a great pleasure that our Journal, Journal of ISAS dealing with borderless analytical sciences comprising of the hybrid interfaces of analytics is going to complete one year of release of its open access, peer reviewed, quarterly electronic version with ISSN and universal id of research works, their digital object identification (doi). We are committed to play a major role in scientific arena involving research and development, their proper application utilising pertinent technology and to create due awareness leading to excellence with relevance.

I am thankful to Head, publication group and Editor in Chief Dr. Nilima Rajurkar and her highly efficient team for the devotion which she imbibes in bringing the journal successfully.

The basic objective of the Journal is to provide utmost exposure to novel research work and it's promotion to the scientific world as far as possible. This would be a reality if we utilise the Journal to the maximum, make it our first choice for publishing our research works. The day won't be too long when the Journal would become first choice by our due support.

Dr. Raghaw Saran
President ISAS and

Advisor J.I SAS

ISAS
Indian Society of Analytical Scientists.

Editorial

It is a largely undisputed fact that analytical chemistry has been developed tremendously in recent years. No experimental science can avoid analytical chemistry today, since it strongly contributes to the achievements and progress of the various disciplines. Indian Society of Analytical Scientists (ISAS) is one of the prime scientific societies working in the field of analytical sciences. It aims towards excellence and relevance in science and technology and is committed to the dissemination of knowledge, expertise, and improved scientific temperament of the entire community of analytical scientists. Keeping this in mind ISAS started its own journal "Journal of ISAS " in July 2022 and we have successfully published three issues until now and I am delighted to present the readers fourth issue of first volume of **"Journal of ISAS"** which is an open access peer reviewed quarterly e-journal with ISSN number as well as DOI. It is having free access to all. We have **a substantive in-depth assessment of the manuscripts received having f**ast and transparent processing without compromising the peer-review standard. Short reviewing time, quick editorial decision, rapid editing of the proofs and helpful communications are the specialities of our journal. As evidenced from our earlier issues, our journal is committed to bring high quality research papers which showcase an integrated approach of all branches of science. This fourth issue contains research articles and review in the field of minerology, nanoscience, adsorption, ayurveda and nuclear industry.

I would like to express my sincere gratitude towards Dr. Raghaw Saran, president ISAS and Chairman, Advisory board of Journal of ISAS for his constant active involvement in the development of this journal which helped timely release of all the issues. I will like to acknowledge editorial and advisory board members as well as the reviewers for extending their cooperation in bringing this issue up to the mark. My special thanks are due to Dr. Vijayalaxmi Adya and Dr. Vinay Bhandari for their continuous association in this valuable task. I congratulate all the contributory authors for their scholarly articles in this issue. My sincere thanks are due to Maharshi Pandya, Shivani Kantak and Vaibhav Parse for the technical support.

Dr. Nilima Rajurkar
Editor in Chief, Journal of ISAS
..

Journal o ISAS

1(4), Pages 1 to 91, (2023)

ISSN : 2583-5459, DOI: 10.59143/isas.jisas.1.4

(An open access Peer reviewed quarterly e- journal by Indian Society of Analytical Scientists)

Contents

X-Ray Diffraction in Mineralogical Research

Yamuna Singh

Centre for Earth, Ocean and Atmospheric Sciences, University of Hyderabad, Gachibowli, Hyderabad-500046

E-mail: yamunasingh1957@gmail.com

Received: 13.4.23, Revised: 16.4.23, 20.4.23 Accepted: 25.4.23

Abstract

A brief account of role of X-ray diffraction (XRD) in mineralogical research with special reference to radioactive and atomic minerals is given. Aspects of research methodology such as sample preparation, analysis time, limitations, search match methods for identification, and complimentary techniques are also given. The most common applications of XRD in mineralogical researches related to radioactive/atomic minerals include identification of primary and secondary uranium and associated ore and gangue minerals, determination of the oxidation grade of uraninites, identification of Th, Nb, Ta, Sn, Be, Li, Zr, Hf, Ti, rare-earth elements (REE) minerals, investigations on degree of structural disordering in Nb-Ta minerals, X-ray crystallographic and substitutional solid solution studies, clay minerals, triclinicity of K-feldspar, metamict minerals and influence of the degree of metamictisation on uranium beneficiation, characterisation of leached residue, beneficiated, heat-treated products, metallurgical slags and other mineralogical studies. The results of mineralogical research are used for elucidating physicochemical conditions and geologic processes that prevailed during mineral formation.

Keywords: *X-Ray Diffraction, Atomic Minerals, Metamict, Oxidation Grade, Triclinicity, Structural Disordering.*

1. Introduction

The X-ray diffraction (XRD) finds wide-ranging applications in different types of researches. Common applications of XRD are (i) Crystal structure determination, (ii)

Phase identification and identification of unknowns, (iii) Quantitative phase analysis, (iv) Quality control in run of mine, (v) Characterisation of polycrystalline and epitaxial thin films, (vi) Textural and stress analysis, (vii) Measurements related to texture and orientation in metals and polymers, (viii) Measurement of thermal expansion, stability and phase diagrams under changing-temperature and changing-pressure conditions, (ix) Pharmaceuticals, (x) Biophysics, and (xi) Forensic science.

Mineralogical study plays a dominant role in addressing several geological issues like genesis of rocks, ores, minerals, mineral systems, tectonic settings and many more. Several laboratory techniques are routinely employed in performing this type of study. Notably, petrological study (Fig. 1), transmitted and reflected microscopy, scanning electron microscopy (SEM), electron probe microanalysis (EPMA), neutron activation analysis (NAA), automated SEM-EDS mineralogy (QEMSCAN), X-ray fluorescence (XRF), X-ray diffraction (XRD), laser induced breakdown spectroscopy (LIBS) and Raman spectroscopy play dominant role. More advanced analytical techniques are also used for mineralogical study. In this paper various applications of X-ray diffraction (XRD) technique, which is a non-destructive and physical analytical method, in mineralogical researches are briefly outlined.

2. Experimental

2.1 Condition

Crystalline solids in the form of powders, single crystals, sheets, foils or filters.

2.2 Amount

Powder - Several hundred milligrams.

Single crystal - an un-cracked, un-twinned crystal of 0.1 to 0.5 mm on a side.

2.3 Sample Preparation

Single crystal - mounting on a fiber or in a glass capillary.

Powder – Crushed solids to 200#.

2.4 Mineral Separation

Rock is aggregate of minerals (Fig. 1). To study each mineral, they need to be separated from the host rocks (Fig. 1) in solid/powder form. The steps involved in this process are outlined

below[1-25].

The rock specimen (Fig. 1) is initially examined using ultra violet lamp for the presence of secondary uranyl minerals. If secondary uranium minerals are present, they would exhibit fluorescence. Such fluorescent minerals are extracted and taken up for XRD study. Discrete coloured grains (Fig. 1) are also scooped up and mounted separately and investigated. The remaining sample is crushed in between 85-100 microns size fraction as per nature of sample. The sieved grain sample and the powder sample are subjected to sequential separation using heavy liquid media.

For separation, commonly used liquids are Bromoform ($CHBr_3$) and Methylene Iodide (CH_2I_2). Bromoform has a specific gravity (SG) of 2.88 and those minerals with specific gravities <2.88 would float in this media. Thus, gangue minerals such as quartz, feldspar, mica would separate out in this media. The bromo-heavies are further separated with the help of methylene iodide (MI).

The SG of methylene iodide (MI) being 3.31, minerals like biotite, apatite, tourmaline, hornblende and some pyroxenes, having SG between 2.88 and 3.31, will come in the light fraction. The MI heavy mineral fraction, comprising minerals of interest, is further separated using Isodynamic magnetic separator.

Thus, various minerals come at different magnetic field strengths, namely, ilmenite (0.2 amps), garnet (0.35 amps), xenotime (0.45 amps), monazite (0.6 amps), uraninite (0.95 amps) and zircon (non-magnetic fraction). Each fraction is then powdered to about 200#, diffracted and diffraction pattern so obtained is studied independently.

Another part of the crushed sample is also centrifuged using bromoform and MI. Various fractions so obtained are studied for mineral phases including clays. This procedure of separation is undertaken to enrich and isolate minerals occurring as discrete phases in minute/trace quantity.

Thus, for instance, say uraninite with concentration levels of 0.04 to 0.06% in a sample can be separated into a fraction with concentration levels reaching as high as 50% to 75% and in a few cases to as high as 95 % in the separated fraction. Accordingly, this combination of separation procedure helps in the concentration of these scarce minerals much above to detection limit.

Various separates obtained are powdered to abut 200#. This power is slowly poured in sample holder groove. After that sample is pressed with glass slide to obtain smooth diffracting surface. This sample-filled holder is mounted in slot within the XRD unit and diffracted.

2.5 Analysis Time

The analysis time ranges from a few minutes to days depending on speed and nature of study. High-capacity X-ray generators and PSDs decrease analysis time. Contrasting this, poorly crystalline samples increase duration of analysis. Phase quantification requires more count time to attain statistical precision.

2.6 Instrument and Standard Used

Siemens D-500 diffractometer was used in most of the studies. NIST supplied Silicon standard was used for checking data of interplanar spacings.

2.7 Operating Conditions

The accelerating voltage was generally kept at 35 kV and tube current at 22 mA. The CuKα radiation (1.5418 Å), monochromatised using curved graphite monochromator, was used for diffraction.

2.8 Mineral Identification Using Search Match Methods

Diffraction pattern of various separates form set of inter planar spacings (d_{hkl}). The d_{hkl} for all crystalline materials have been grouped by the International Center for Diffraction Data (formerly the Joint Committee on Powder Diffraction and Standards) using procedures helpful in their identification. The Fink and Hanawalt are the two well-known search match methods.

Certain isostructural minerals give a powder pattern that are undistinguishable on initial diffraction. Such minerals when subjected to heat-treatment convert to a

different form. The pattern of each of these heat-treated-product would be different depending on the composition of the initial mineral. As an example, fluorite, uraninite, pyrite and sphalerite are isostructural and give their respective reflections at the same angle. When these minerals are heated, they transform to their stable oxide phase whose powder patterns are different from one another, thus leading to their identification.

Minerals containing uranium and thorium as essential constituents are irradiated internally by alpha and beta particles and gamma radiation released during the radioactive decay. The alpha particle has the mass of a helium nuclei and moves in a recoiling trajectory. When the alpha particle encounters an atom, it dislocates the atom from its mean position. As a result, the mineral loses its crystallinity and becomes optically isotropic. This process is called metamictisation and the mineral is said to be metamict.

The original or the near original structure can be restored by heating the sample in a muffle furnace below the temperature of their phase transformation. Thus, the metamict mineral is heated in a series of steps starting from about 500^0 C onwards for a period ranging from 3 to 24 hours and examined each heat-treated fraction for restoration of their structure. In general, heating the sample would result in the restoration of its original structure.

2.9 Limitations

2.9.1 General

In XRD study, only crystalline phases can be identified. Overlapping of peaks may restrict mineral analysis and quantification. Nature of matrix also influences diffraction pattern. For example, strongly diffracting minerals may mask poorly diffracting phases. Preferred orientation, as exhibited by mica, increases intensity of diffracted beam, which limits quantitative phase analysis. Fluorescent material may enhance background of diffraction pattern. It may also cause saturation in low-capacity detectors.

2.9.2 Accuracy

Quantitative study of powder mixtures with <1% accuracy and higher precision is achieved under favourable conditions with appropriate standards.

2.9.3 Sensitivity and Detection Limits.

In practice, detection limit changes with the type of XRD unit. Whereas, in principle, the limiting factor is the given duration of analysis.

3. Results and Discussion

3.1 Mineralogical Research

The most common applications of XRD in mineralogical researches related to radioactive/atomic minerals are as follows[1-31].

Identification of primary (uraninite, coffinite, brannerite, davidite) and a host of secondary uranium (uranyl phosphates, silicates, carbonates, vanadates, etc.) and other ore (and associated gangue) minerals in uranium ore deposits/occurrences. Due to the soft nature, flaky habit and fine-size nature, common occurrence as fillings, coating, encrustations, of secondary uranium minerals, XRD is of immense help in identifying such mineral phases, which otherwise pose severe problems in their identification by conventional optical mineralogical techniques.

Determination of the oxidation grade of polygenetic uraninites for elucidating genesis of uranium ores from diverse geological settings is done. This data is useful in distinguishing genetic aspects of uranium deposits formed in various geological settings, namely, Pegmatitic, Proterozoic unconformity-related, Metamorphic, Metasomatic, Metasediments, Sedimentary, French Veins, and Hydrothermal. Apart from these, prevalence of temperature (range) during formation of uranium deposits is also inferred. Characteristics of clay minerals hosted in diverse types of uranium ore deposits/occurrences also reveals about genesis of uranium deposits.

Identification of Th, Nb, Ta, Sn, Be, Li, Zr, Hf, Ti, rare-earth element (REE), and other associated ore and gangue mineral assemblages is routinely done. Investigations on degree of structural disordering in primary minerals of niobium and tantalum are

done to unravel the attendant physicochemical conditions during ore genesis. X-ray crystallographic and substitutional solid solution studies are performed, mainly on U, Th, Nb, Ta, Sn, Zr ore-minerals.

Determination of triclinicity of K-feldspar from rare-metal and rare-earth-mineralised granites and pegmatites is done to elucidate the evolutionary history of parent rocks and hosted mineralization. K-Feldspar cooled slowly under falling temperature in plutonic conditions will be reflected by maximum value of triclinicity (close to unity).

Fingerprinting of metamict minerals and investigations of influence on the degree of metamictisation on uranium beneficiation are done (Fig. 2). This study revealed that highly metamictised phases are more amenable for uranium leaching (Fig. 2). Characterisation of leached residue, beneficiated, and heat-treated products of uranium ores is also done (Fig. 2). Identification of metallurgical slags for mineral, heat-treated products and chemical phases are also routinely done.

Identification and structural study of atomic (monazite, rutile, zircon, ilmenite) and associated industrial (andalusite, sillimanite, garnet) minerals in beach sand and off-shore mineral deposits are performed. Several other mineralogical studies include determination of composition of olivine, garnet, feldspar, identification of new phases, and so on.

3.2. Complimentary Techniques

Neutron diffraction is more suitable for location of light atoms in a crystal structure, whereas gamma-ray diffraction is useful for structural and defect studies of crystals. Thermogravimetric analysis (TGA), differential thermal analysis (DTA), and differential scanning calorimetry (DSC) are additionally useful for mineral identification and quality control and on unraveling reactions in solid-state. X-ray fluorescence (XRF) gives compositional data, which helps in mineral identification[26-31].

4. Conclusion

The X-ray diffraction is a versatile nondestructive analytical technique and finds wide ranging applications in mineralogical research for elucidating physicochemical conditions and geologic processes that prevailed during mineral genesis.

5. Acknowledgements

This is a slightly modified version of the invited talk delivered in Indian Analytical Science Congress-2022, organized by ISAS at Munnar, Kerala during 10-12 March, 2022, for which I am very grateful to Dr. V.R Nair and Dr. P.P. Chandrachoodan for extending invitation to me for delivering this talk and to Prof. (Dr.) Nilima Rajurkar for motivating me to contribute. Two anonymous reviewers of the Journal are thanked for useful suggestions that improved manuscript.

Figures:

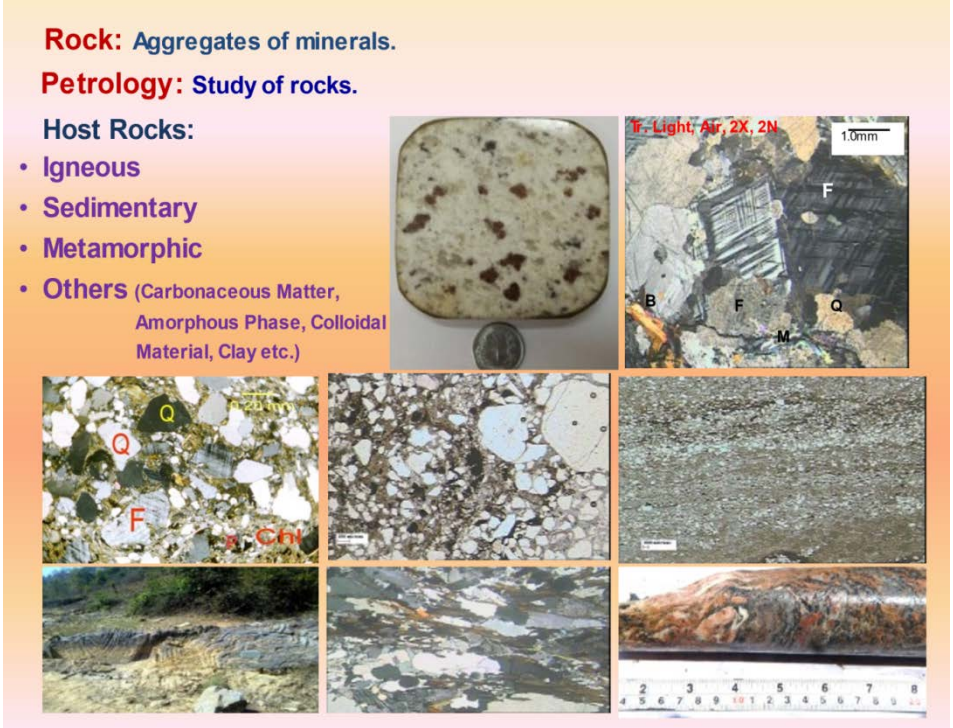

Fig. 1. Igneous, metamorphic and sedimentary rocks and other geological materials with their constituent mineral aggregates. Individual minerals are separated physically using heavy media liquids (bromoform and methyline iodide) and isodynamic magnetic separator from such mineral aggregates from samples of interest and studied independently using X-ray diffraction for various types of mineralogical researches. Q – Quartz, F – Feldspar, Chl – Chlorite, B – Biotite, M – Muscovite.

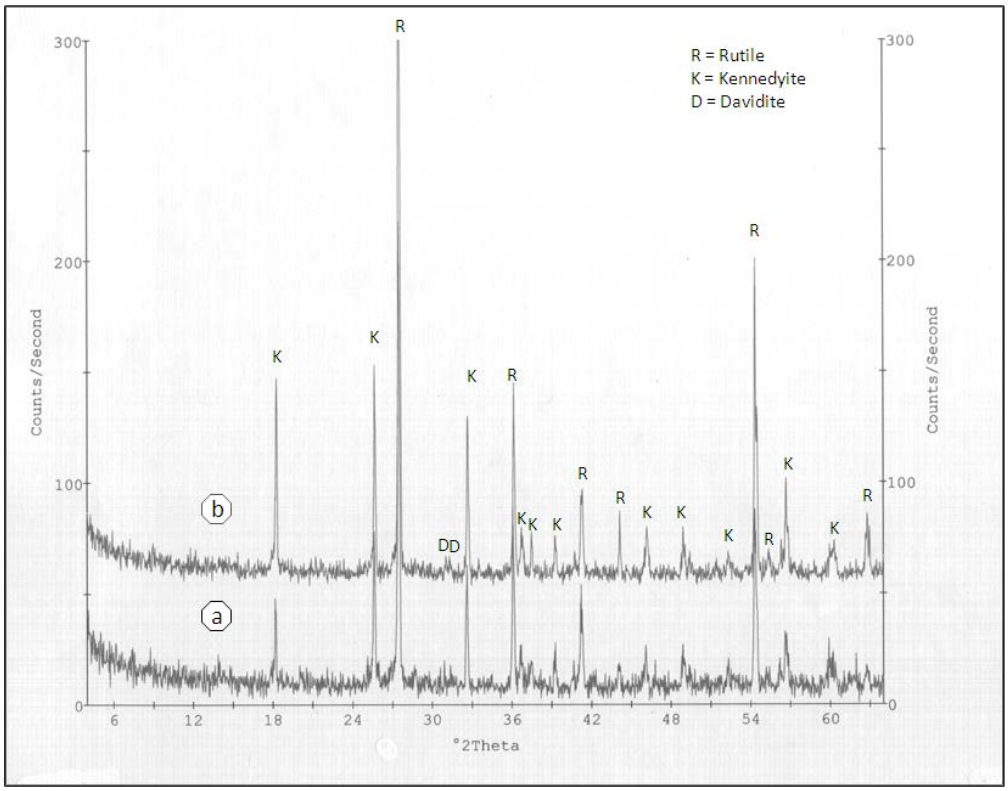

Fig. 2. X-ray powder pattern of successively heat-treated fractions of leached residue of feed ore from albitite belt, western India. Note only two minor reflections of davidite (marked D) and complete absence of brannerite. Also, note very prominent reflections of kennedyite (marked K) and rutile (marked R). Formation of kennedyite (K) and also additional (and hence enhancement of intensity of) rutile (R) is due to breaking and conversion of anatase in to another high-temperature polymorph of Ti on account of heat treatment.

References

1. Y. Singh, K.K. Pandey, R. Viswanathan, Explor. Res. At. Minerals, 20, 167, 2010.
2. R. Viswanathan, Y. Singh and S. Thangavel, Explor. Res. At. Minerals, 20, 159, 2010.
3. R. Viswanathan, Y. Singh, M. Sai Baba, A. Som, K. Shiv Kumar, K., and K. Umamaheswar, Explor. Res. At. Minerals, 19, 178, 2009.
4. Y. Singh, R. Viswanathan, P.S. Parihar, and P.B. Maithani, Ind. Mineral., 45 (2), 1, 2011.

5. Y. Singh, R. Viswanathan and A. Chaki, Gond. Geol. Mag., Spl. Vol. No. 12, 21, 2010.
6. Y. Singh, R. Viswanathan, P.S. Parihar, and P.B. Maithani, Gond. Geol. Mag., Spl. Vol. No. 13, 53, 2012.
7. Y. Singh, K.K. Pandey, P.K. Gupta, S.D. Rai and G.B. Joshi Proc. International Seminar on Mineral Processing Technology (MPT-2017), 1-3 February, 2017, Mahabalipuram, Chennai, pp. 130, 2017.
8. Y. Singh and K.K. Pandey, Explor. Res. At. Minerals, 18, 125, 2008.
9. Y. Singh and R. Viswanathan, Explor. Res. At. Minerals, 21, 41, 2011.
10. R. Viswanathan and Y. Singh, Ind. Mineral., 45 (1), 130, 2011
11. Y. Singh, Jour. Geol. Soc. India, 79 (6), 664, 2012.
12. Y. Singh. and R. Viswanathan, Explor. Res. At. Minerals, 22, 109, 2012.
13. Y. Singh, R. Viswanathan, P.S. Parihar, and P.B. Maithani, Jour. Geol. Soc. India, 81 (1), 79, 2013.
14. Y. Singh and P.S. Parihar, Ind. Mineral., 48 (1), 73, 2014.
15. Y. Singh, G. Nagendra Babu, R. Viswanathan, M. Sai Baba, A.K. Rai, and P.S. Parihar, Cent. Euro. Jour. Geosciences, 6 (4), 492, 2014.
16. R. Viswanathan, Y. Singh, G. Nagendra Babu, M. Sai Baba and K. Shiv Kumar, Jour. Applied Geochemistry, 17(2), 130, 2015.
17. Y. Singh, R. Viswanathan, L.S.R. Reddy and M. Sai Baba, Jour. Applied Geochemistry, 17 (4), 404, 2015.
18. Y. Singh and R. Viswanathan, Explor. Res. At. Minerals, 25, 105, 2015.
19. Y. Singh, R. Viswanathan, P. Jagadeesan, K.L. Mundra, A.K. Bhatt, P.K. Gupta, S.D. Rai and G.B. Joshi, Jour. Geosciences Research, Spl. Vol. No. 1, 139, 2017.
20. Y. Singh, A. Saxena, A.K. Bhatt, R. Viswanathan, T. S. Shaji and L.K. Nanda, J. Earth Sys. Science, 127:4, 2018.
21. B.N. Tikoo, A. Chaki, Y. Singh and S. Viswanathan, Explor. Res. At. Minerals, 19, 172, 2009.
22. S. Viswanathan, A. Chaki, and Y. Singh, Ind. Mineral., 44 (1), 130, 2010.
23. B.N. Tikoo, A. Chaki, Y. Singh and S. Viswanathan, Ind. Mineral., 44 (1), 137, 2010.

24. Y. Singh, A.R. Mukhopadhyay and R. Viswanathan, Ind. Mineral., 44 (1), 182, 2010.
25. Y. Singh, R. Viswanathan, N. Goyal, B. Panigrahi, P.K. Jain, and M.K. Khandelwal, Ind. Mineral., 44 (1), 167, 2010.
26. S. Viswanathan, A. Chaki, and Y. Singh, Jour. Geol. Soc. India, 76, 171, 2010.
27. S. Viswanathan, P.B. Maithani, and Y. Singh, Jour. Applied Geochemistry, 14 (3), 289, 2012.
28. V. Madakkaruppan, H. Basu, B. Sunilkumar, T.S. Sunil Kumar and Y. Singh, Atomic Spectroscopy, 39 (2), 90, 2018
29. B.N. Tikoo, A. Chaki, Y. Singh and S. Viswanathan, Geol. Soc. India, Mem. 73, 311, 2008.
30. C. Sarbajna, S. Durani, S. Pandey, and Y. Singh, Proc. International Symposium on Emerging Trends in Analytical Chemistry (ETAC – 2016), September PP 21, 2016, Organised jointly by AMD & ISAC, Bangalore Chapter, at AMD, Bangalore, pp. 139, 2016.
31. S. Viswanathan, R. Rangaswamy, B.N. Tikoo, P. Krishnamurthy, S.P. Balakrishnan, K. Shivkumar, Y. Singh, S.C. Sehgal, and T. Narsimha, Geol. Soc. India, Mem. 73, 325, 2008.

Plant-extract-assisted green synthesis of silver nanoparticles using *Macaranga Indica* bark extract for antimicrobial and photocatalytic activity

G. Hegde[1,3], S. Yallappa[2*], T. Khadre[3], Sudha Joseph[4], J. Manjanna[5]

1. Environmental Lab, Indian Institute for Human Settlements, Bengaluru-560060, Karnataka, India
2*.Department of Chemistry, AMC Engineering College, Bangalore-560083, Karnataka, India.
3.Department of Chemistry, Dr. A.P.J Abdul Kalam University, Indore-452010, Madhya Pradesh, India
4. Department of Mechanical Engineering, Cambridge Institute of Technology, Bangalore 560036, Karnataka, India
5. Dept. of Chemistry, Rani Channamma University, Belagavi 591156, Karnataka, India

Email: yallappashiralgi5@gmail.com (S. Yallappa)

Received: 24.3.23, Revised: 27.4.23 Accepted: 28.4.23

Abstract: A rapid and environment-friendly green synthesis of silver nanoparticles (AgNPs) using *Macaranga Indica (M. Indica)* plant extracts was explored in this study. The obtained AgNPs were characterized by UV–Vis, XRD, FTIR, and SEM for antimicrobial and photocatalytic activities. The typical surface plasmon resonance peak around 440 nm confirmed the formation of AgNPs. The particles were found to be very tiny in the range of 15–20 nm size and showed *fcc* crystal symmetry. The FT-IR study showed the presence of bio-molecules on the surface of AgNPs and acting as capping agents. The *in vitro* antibacterial screen of AgNPs showed the bio-capped AgNPs have a higher inhibitory action for *E. coli* and *S. aureus* followed by *C.albicans.* The degradation property of the AgNPs towards Rhodamine B (RhB)under different conditions revealed that the degradation efficiency of phytochemicals-coatedAgNPs on RhB was found to be high and around 88.8% within 70 min.

Key Words: AgNPs, *Macaranga Indica*, Rhodamine B, Antimicrobial activity

Introduction

M. indica has been traditionally used in Indian Ayurvedic and Siddha medicine to treat anemia, paralysis, tumors, cuts, wounds, colon cancer, and other related ailments[1–3]. Plants of this genus have been reported to produce a range of phenolic compounds, most notably prenylated flavonoid sand stilbenes[4]. *M. indica* is a species of tree that grows to about 25 meters in height. Previous phytochemical studies on *M. indica* led to the isolation and identification of flavonoids, isoflavones and their prenylated derivatives[1, 5]. Although plant extracts are used in traditional medicine, the lack of sustained potency of the extract becomes a major obstacle in drug development[6], hence new methods are required. Bio-inspired AgNPs offer mutation-resistant antibacterial properties and are used as filters in water treatment plants, wound healing ointments, HIV prevention and treatment, food packaging, cosmetic products as well as coatings on medical devices[7–9]. Different plant extracts derived from the leaves, bark, seeds, flowers, and fruits have demonstrated various advantages as both reducing and capping agents[10–12]. Phytochemicals, the bioactive components of the plant extract are known for their role in reducing Ag^+ ions and stabilizing NPs over a long period of time increasing biological and environmental applications.

In recent years, photocatalysis has been viewed as an alternative, cost-effective method to eliminate hazardous chemicals[13]. The photocatalytic process for breaking down organic pollutants has attracted a great deal of interest due to its exceptional advantages. Therefore, it is imperative to find a suitable and effective photocatalyst during the degradation process. The performance of a photo decolorization reaction is affected by the quality and properties of the photocatalyst, which is typically a semiconducting material with the ability to generate electron-hole pairs in the presence of light[14, 15]. There were no reports on the biosynthesis of AgNPs using the aqueous bark extract of *M. Indica* which is a traditionally used ethnomedicinal plant as described here. The objective of the present work is to synthesize AgNPs by a green approach using the medicinally important *M. Indica* plant and to screen for bacterial and fungal activity against *E. coli*, *S. aureus*, and *C. albicans.* Moreover, the application of synthesized Ag NPs in photocatalytic degradation of RhB dye under UV light irradiation was investigated. The rate constant in photocatalytic degradation with respect to RhB dye concentration was also estimated. The rhodamine B is a toxic dye

widely used in traces and colorants, and is carcinogenic and mutagenic to humans and organisms. Microplastics can accumulate with RhB in the aquatic system leading to high environmental risks. Hence, it is necessary to remove it from the aquatic system by using sustainable methods.

2. Experimental

2.1. Materials

M. Indica bark was collected from the village of Siddapur Taluk, Bilgi in Karnataka, India in the Western Ghats. Hi-media Laboratory supplied analytical grade silver nitrate ($AgNO_3$) (Mumbai, India). The *M. indica* extract was prepared in distilled water using a microwave oven (LG MJEN326UH, 2.45 GHz) for subsequent AgNPs synthesis.

2.2. Green synthesis of AgNPs

To extract the phytochemicals, 6 g of freshly chopped, finely ground *M. Indica*bark was mixed with 250 mL of distilled water in a beaker. The mixture was then microwave-irradiated for around 300 seconds. In a heated environment, it was filtered using a 0.45-micron membrane filter. After cooling to room temperature (RT), it was used for the synthesis of AgNPs.In a typical synthesis of AgNPs, 50 mL of a 0.001M aqueous solution of $AgNO_3$ was mixed with 20 mL of bark extract. The mixture was exposed to microwave radiation for different intervals of time. The pale yellow to dark brown colour within 300 seconds indicates the formation of AgNPs. The prepared solution was stored for two days prior to characterization.

2.3. Characterization of solid AgNPs

The UV–vis spectra were recorded with a UV–Vis spectrometer (UV-2450, Shimadzu). The size and morphology of AgNPs were investigated using scanning electron microscopy (SEM) (JEOL-JSM 6701-F, Japan) operated at an accelerated voltage of 200 kV. The elemental composition was determined using the EDX analysis. With Cu-Kα radiation from 10° to 60° (2θ) with a step size of 0.01°, the X-ray diffraction patterns were recorded with an X-ray diffractometer (D8 Focus, Bruker, Germany). To identify the potential biomolecules capping on AgNPs, an FTIR (Perkin Emler) spectrum was obtained in the KBr pellet.

2.4. *In vitro* antimicrobial activity AgNPs

The *in vitro* antibacterial activity of AgNPs was evaluated using the agar well diffusion method as follows[16]. Test pathogens included *E. coli* (ATCC 25922), *S. aureus* (ATCC 11682), and *C. albicans* (MTCC 3017). Mueller Hinton Agar (MHA) and Potato Dextrose Agar (PDA) were usedfor antimicrobial assays. A cork borer was used to create 6mm wells in the agar plates. In the wells, 100µL of AgNPs (50 µg/mL) were added. Ciprofloxacin and fluconazole were used as standards for both antibacterial and antifungal activity, respectively. Dimethyl sulfoxide (DMSO) was used as a control. The bacterial plates were incubated at 37 °C for 24 hours, while the fungal plates were incubated at 30 °C for 48 hours. The zone of inhibition (ZOI) was observed with a measuring scale after the incubation period. All tests were performed in triplicate.

2.5. Photocatalytic activity of green synthesized AgNPs

The photocatalytic activity of the green synthesized AgNPs was studied for the RhB dye under sunlight irradiation. To every 80 mg/L solution of the dye, 5 mg AgNPswere added and stirred in the dark for 30 minto reach adsorption/desorption equilibrium. Then, the reaction wasmoved outside to be carried out under sunlight. The progress of their action was monitored by measuring the absorbance of the reaction mixtures at intervals of 10, 20, 30, 40, 50, 60 and 70 mins after theinitiation ofthe reaction under sunlight. The dye adsorption percentage is calculated using the following formula:

$$\%\ \text{of RhB dye adsorption} = \frac{\text{Initial absorption -Final absorption}}{\text{Initial absorption}} \qquad (1)$$

3. Results and Discussion

3.1. Green synthesis and characterization of AgNPs

After 10-300 seconds of microwave irradiation, the reaction mixture (50 mL of 1 mM $AgNO_3$ plus 20 mL of bark extract) changed color from pale yellow to black in about 60 seconds. With increasing irradiation time, the intensity of the reaction mixture increased until it reached saturation in about 300 seconds. The broad peak occurring in the region of 430–440 nm (Fig. 1a) depending on the exposure time is considered to be the Surface Plasmon Resonance (SPR) of AgNPs[17]. The inset of the figure shows the photocopy of the color of the

aqueous bark extract and AgNPs formation. This finding demonstrates that *M. Indica* bark extract reduces Ag^+ to Ag^0. The increase in particle size and yield of AgNPs with irradiation time is likely the reason for the redshift of SPR from 430 nm to 450 nm. A similar UV-Visible spectrum was observed for AgNPs synthesized from *Cucumis prophetarum* aqueous leaf extract[18] and *Cannabis sativa* leaf extract[19].

The optical band gap of synthesized AgNPs was calculated according to the Tauc relation (αhv) is 2.8 eV.

$$ahv = A(hv - Eg)n \qquad (2)$$

where α is the absorption coefficient, A is constant, v is the frequency, h is the plank's constant, Eg is bandgap energy, and n = 1/2 is for a direct bandgap of the NPs. Fig. 1b shows an SEM image of as-synthesized AgNPs. The majority of bio-capped AgNPs are spherical, mono-dispersed particles with a diameter (ϕ) of between 15 and 20 nm. The SEM image shows a type of foam on the particles, which is most likely the result of the bio-capping of organic moieties from the plant extract. The EDX profile (Fig.1c) confirmed the presence of Ag as the main element with 53.47 atomic %. Traces of C, O, and Cl are also seen due to the presence of plant residue and other organic materials with AgNPs acting as bio-capping. The AgNPs are stabilized by bio-capping, and these bio-capping AgNPs, especially in combination with pharmacological plant extracts, have shown improved biological and photocatalytic activity[20, 21]. The putative bio-molecules of *M. indica* bark extract involved in $AgNO_3$ reduction and AgNPs stabilization were identified by FTIR spectroscopy. The FTIR spectrum in Fig. 1(d) shows the major bands at 3265, 2935, 1568 and 1288cm^{-1}. The bands at 3265 cm^{-1} and 2935 cm^{-1} correspond to the OH stretch of the polyphenols group and the C–H stretching of the methylene group or a characteristic peak of triterpenoid saponins [22]. The bands at 1568 cm^{-1} and 1288 cm^{-1} may be assigned to the C-H bending of the aromatic and the C-N stretching of the amine group or the OH bending of the phenol respectively. A band appears at 1708 cm^{-1} corresponding to C=O bond formation[23]. This could be due to the oxidation of the OH group to the CO group[8]. This further indicates the role of polyphenolic compounds and proteins in the reduction of Ag^+ to Ag^0. The capping of the AgNPsby the bio-molecules is also evident from the presence of the major bands in FTIR spectra. A typical XRD pattern of synthesized AgNPs is shown in the inset of Fig. 2. All peaks in the XRD pattern can be indexed as a face-centered cubic (*fcc*) structure of Ag (JCPDS No. 89-3722) [24]. The XRD pattern shows the presence of diffraction peaks corresponding to (111), (200), (220), (311), and (331) planes. The mean particle size determined using the Scherrer

method at the prominent (111) diffraction peak is 18±3 nm, agreeing with the size of isolated NPs observed in the SEM analysis.

3.2. Antimicrobial Activity of AgNPs

The bio-molecules coated AgNPs were tested for antibacterial activity against Gram-positive bacteria, Gram-negative bacteria, and a fungus. An antimicrobial test was carried out using the agar well diffusion assay[25] and the results showed high antimicrobial activity of AgNPs against all tested pathogens. **Table 1** shows the results for the mean zone of inhibition (ZOI) and minimum inhibitory concentration (MIC) for all pathogens tested. The MIC is the lowest concentration of drug that prevents visible microbial growth. The negative control, DMSO, showed no zone of inhibition. According to the ZOI, Gram-negative bacteria have the greatest antibacterial activity. The crude plant extract of *M. indica* showed very little inhibitory activity against the pathogens tested. Using broth dilution methods, the MIC for AgNPs is determined to be most effective against *E. coli*, followed by *S. aureus* and *C. albicans* (Fig. 3a). ZOI and MIC indicate that AgNPsrestrict the development of both bacteria and fungi. The percentage of colonies formed on agar plates as a function of AgNPs concentration is shown in Fig. 3b. After treatment with AgNPs, it was found that the number of colonies decreased significantly compared to the control. A substantial peptidoglycan layer in the cell wall of *S. aureus* is responsible for the organism's low susceptibility[26].

Table 2 shows a comparison of the antibacterial activity of AgNPs synthesized using *M. indica* bark extract with that of previously reported studies. The MIC results of AgNPs synthesized with *Banana peel extract*are lower than those observed for AgNPs synthesized from *M. indica*, while the MIC of *Solanum tricobatum and Terminalia arjuna* bark extract are comparable to our results[27–29]. This demonstrates that AgNPs synthesized from *M. indica*exhibit superior antibacterial and antifungal activity. The antimicrobial activity, dispels the notion that cell membrane communication is caused by electrostatic interactions[33, 34]. The size and shape of NPs are considered important parameters of antimicrobial activity. AgNPs accumulate in different parts of the cell and make the membranes of Gram-positive bacteria, Gram-negative bacteria and fungi less stable. This leads to cell lysis via the formation of pits and the accumulation of NPs in the cytoplasm. Furthermore, AgNPs having 20 nm size or smaller have more contact with cells than larger NPs leading to the internalization of NPs into cells and then the release of toxic ions[29]. Thus, the size of the NPs is an important parameter for their antimicrobial activities and the better antimicrobial activity of AgNPs synthesized from *M. Indica* could be attributed to their small size.

3.3. Photocatalytic Activity of AgNPs

Rhodamine B (RhB) is a popular water-soluble dye widely used in industrial sectors such as textile, leather, printing, paper and pharmaceuticals. The degradation of this dye in the presence of green synthesized AgNPs was monitored with a UV–Vis spectrophotometer. The highest absorption of RhB was observed at 663 nm. The degradation of RhB dye upon solar irradiation catalyzed by AgNPs is reflected by a gradual decrease in the absorption peak of the dye solutions. From Fig. 4a it can be seen that the absorption band of RhB at 663 nm decreases with time and eventually approaches the baseline, indicating the successful degradation of the dye in the presence of AgNPs. Fig. 4(b) shows the variation of the Ln (A_0/A_t) Vs time for RhB. The degradation rate constant calculated for RhB is 30 x 10^{-3} min^{-1}. The decrease in Ln (A_0/A_t) value with time indicates that the reaction process followed pseudo-first-order kinetics.

In this study, the percentage of RhB dye degradation calculated from the absorption spectra was 88.8%.Previous studies have reported thatAgNPssynthesized usingthe solid-state thermal decomposition method achieved 40% RhB degradation after 60 min of sunlight exposure[35]. Furthermore, Roy et al. observed that 75% of methyl orange dye was degraded in 480 minutes by AgNPs derived from *Solanum tuberosum* infusion[36]. Liang et al. reported that no significant orange G dye degradation activity was observed usingAgNPsprepared from *Lemon* fruit extract[37]. This evidence conclusively shows that the AgNPs synthesized from *M. indica* extract in the present study exhibit stronger photocatalytic activity than AgNPs synthesized from other sources.

Since there are more active sites on the larger surface area of NPs, a wider variety of dye molecules can be degraded by electron transfer. Fig. 4c shows the mechanistic view of dye degradation in the presence of AgNPs. When exposed to Sunlight, the electrons in Ag ions become excited and transfer from the valence band to the conduction band. This creates electron-hole pairs that serve as effective oxidizing and reducing agents.These excited electrons generate free radicals such as HO•, $O•_2^{2-}$ and HOO• on the catalyst surface, the active sites of AgNPs when they combine with the oxygen present in the reaction mixture[38]. The rate of degradation is significantly influenced by the structure of the dyes and the structure of the polycyclic dyes used in this study as shown in Fig. 4c. The rate of dye degradation is slowed down by the presence of sulfonyl and nitro groups. Since RhB dye does not have a sulfonyl group, it degrades faster. It is imperative that the catalyst is reusable.

As a result, AgNPs obtained from *M. indica* bark extract were collected after each run and reused five times to determine their potency after each run. As shown in Fig. 4d, the activity of the catalyst slightly decreased after it was successfully used three times. For instance, up to three times the degradation of the catalyst was 88%, then the 4^{th} run was reduced to 86.5% degradation and the 5^{th} run was further reduced to 86 % degradation. This result demonstrates that AgNPs can be successfully recovered and reused, making them suitable for wastewater treatment.

4. Conclusion

AgNPs were synthesized byplant extraction-assisted green synthesis using *M. indica* bark extractand microwave irradiation technique. The synthesized AgNPs were characterized using UV-Visspectrophotometer, SEM, EDX, XRD and FT-IR techniques and concluded that the formed AgNPs range in size from 15-20nm. The *in situ* coating with secondary plant substances is evidentfrom the FTIR spectra. Phytochemical-coated AgNPs showedpotent antimicrobial activity against *E. coli*, *S. aureus* and *C. albicans.* Adsorption studies with RhB dye have shown that AgNPsare able to remove 88.8 % of the dye within 70 min contact time. Overall, thiswork presents an environmentally friendly method for the rapid synthesis of AgNPs that can be used as antimicrobial agents and for treating wastewater.

Figures:

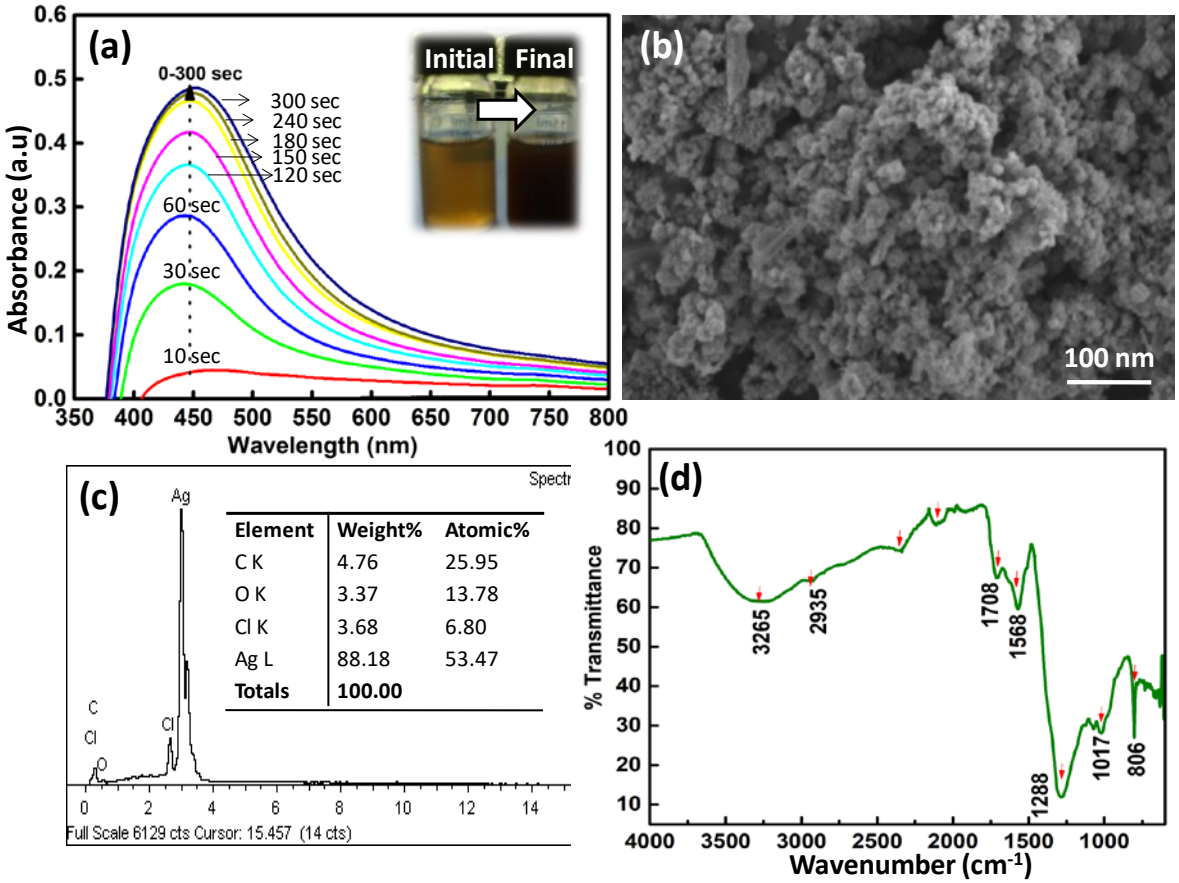

Fig. 1. (a) UV-Vis spectra of AgNPs formation at a different time interval (0-300 sec): insets hows the reaction mixture with *M. indica* bark extract at 10 and 300 seconds, (b) SEM image of AgNPs (c) EDX profile of AgNPs and (d) FTIR analysis of AgNPs.

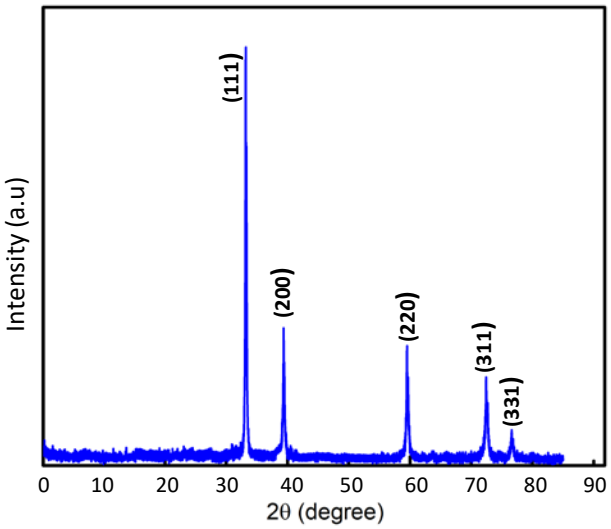

Fig. 2. XRD pattern of AgNPs

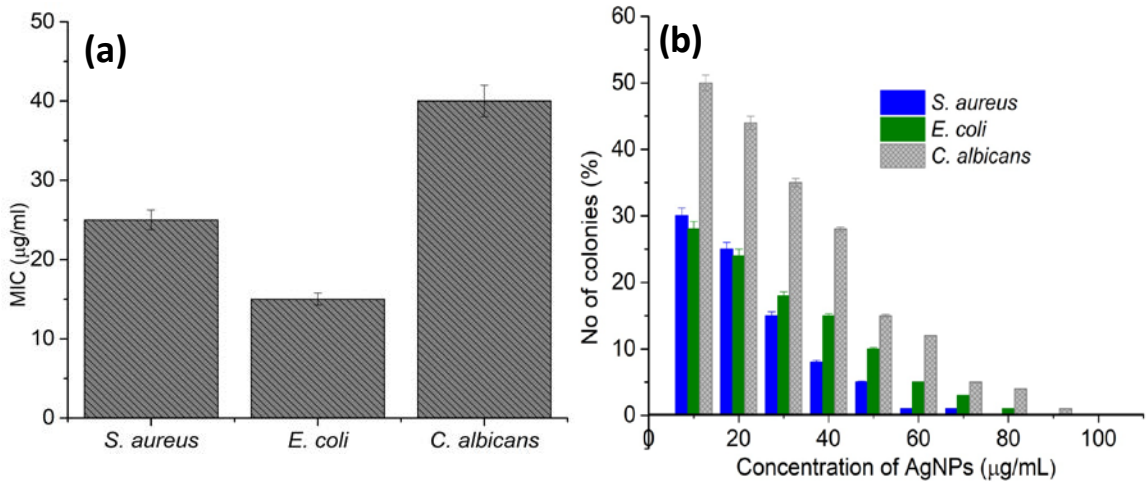

Fig. 3. (a) MIC of AgNPs against *S. aureus*, *E. coli* and *C. albicans* and (b) the number of colonies as a function of the concentration of AgNPs (µg/mL).

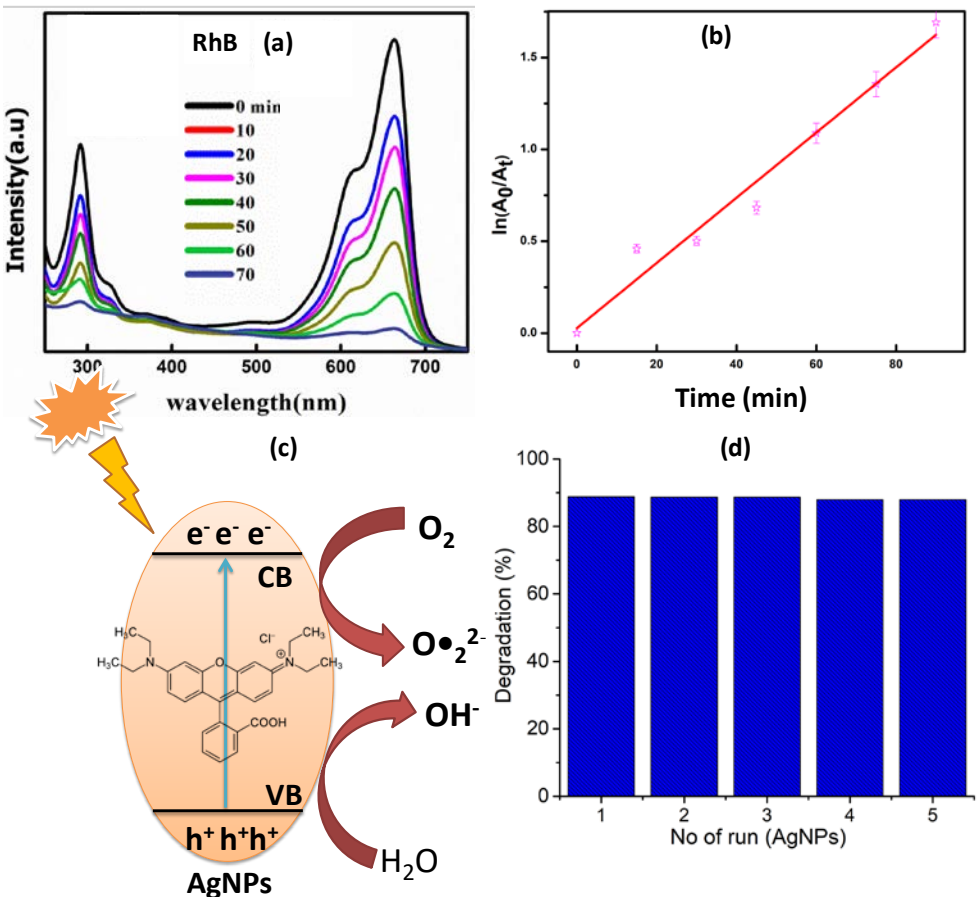

Fig. 4. (a) UV–Vis spectra of RhB dye in the presence of AgNPs, (b) Ln (A_0/A_t) Vs time plot, (c) the mechanistic view of dye degradation in the presence of AgNPs and (d) RhB dye degradation activity of AgNPsup to 5 runs.

Tables:

Table 1. Zone of Inhibition (mm) and MIC (µg/mL) of AgNPs synthesized from *M. indica* bark extract for tested strains.

Test pathogens	**AgNPs (50 µg/ml)**	**Standard (Ciprofloxacin/ Fluconozole)**	**Negative control (DMSO)**	**MIC (µg/ ml)**
	Zone of inhibition (in mm)			
S. aureus	15.37 ± 0.34	24	No Inhibition	25
E. coli	18.47 ± 0.47	25	No Inhibition	15
C. albicans	11.23 ± 0.27	17	No Inhibition	40

Table 2. Comparison of the antimicrobial activity of AgNPssynthesized using different plant parts

Different plant extract (leaves, bark, seeds)	**Test strains**	**Zone of Inhibition (mm)**	**Reference**
Solanum tricobatumleaves extract	*S. aureus* *E. coli*	17.0 8.00	[27]
Banana peel extract	*C. albicans*	10.10	[28]
Impatiens balsamina leaves extract	*S. aureus* *E. coli*	11.03 10.20	[30]
Terminalia Arjuna bark extract	*S. aureus* *E. coli* *C. albicans*	8.00 11.00 06.00	[29]
Dioscorea batatas rhizome extract	*C. albicans*	10.00	[31]
Withaniasomnifera leaves extract	*S. aureus*	11.00	[32]

	C. albicans	No Inhibition	
M. indica bark	*S. aureus*	15.37	*Present study*
	E. coli	18.47	
	C. albicans	11.23	

Acknowledgment

The authors thank the Environmental Research Laboratory, Indian Institute for Human Settlement, Bangalore, for conducting this research.

References

1. S. Sultana and M. Ilyas, *Phytochemistry* 25, 953, 1986.
2. D. T. M. Huonga, L. T. Anh, N. T. Cuc, N. X. Nhiem, B. H. Tai, P. Van Kiem, M. Litaudon, T. D. Thach, C. Van Minh, and V. C. Pham, *Phytochem. Lett.* 34, 39, 2019.
3. L. T. N. Vu, L. T. Anh, N. T. Cuc, N. X. Nhiem, B. H. Tai, P. Van Kiem, M. Litaudon, T. D. Thach, C. Van Minh, and H. D. T. Mai, *Nat. Prod. Res.* 35, 2123, 2021.
4. J. M. Joseph, *J. Med. Plants Res.* 8, 489, 2014.
5. S. Sultana and M. Ilyas, CHEMICAL INVESTIGATION OF MACARANGA-INDICA WIGHT, 1987.
6. M. T. Wingo, J. M. Huber, J. H. Szostek, S. L. Bornstein, J. A. Post, K. F. Mauck, and M. L. Wieland, *Am. J. Med.* 134, 854, 2021.
7. M. Shivakumar, K. L. Nagashree, S. Yallappa, S. Manjappa, K. S. Manjunath, and M. S. Dharmaprakash, *Enzyme Microb. Technol.* 97, 55, 2017.
8. S. Yallappa, J. Manjanna, S. K. Peethambar, A. N. Rajeshwara, and N. D. Satyanarayan, *J. Clust. Sci.* 24, 1081, 2013.
9. D. Hebbalalu, J. Lalley, M. N. Nadagouda, and R. S. Varma, *ACS Sustain. Chem. Eng.* 1, 703, 2013.
10. T. K. Dua, S. Giri, G. Nandi, R. Sahu, T. K. Shaw, and P. Paul, *Food Chem. Adv.* 100205, 2023.
11. N. T. T. Nguyen, L. M. Nguyen, T. T. T. Nguyen, R. K. Liew, D. T. C. Nguyen, and T. Van Tran, *Sci. Total Environ.* 154160, 2022.
12. C. Singh, S. K. Anand, R. Upadhyay, N. Pandey, P. Kumar, D. Singh, P. Tiwari, R. Saini, K. N. Tiwari, and S. K. Mishra, *Mater. Chem. Phys.* 127413, 2023.
13. T. Fazal, A. Razzaq, F. Javed, A. Hafeez, N. Rashid, U. S. Amjad, M. S. U. Rehman, A. Faisal, and F. Rehman, *J. Hazard. Mater.* 390, 121623, 2020.
14. S. Joseph and B. Mathew, *Mater. Sci. Eng. B* 195, 90, 2015.
15. D. Gola, N. Bhatt, M. Bajpai, A. Singh, A. Arya, N. Chauhan, S. K. Srivastava, P. K. Tyagi, and Y. Agrawal, *Curr. Res. Green Sustain. Chem.* 4, 100132, 2021.
16. Y. Y. Loo, Y. Rukayadi, M. A. R. Nor-Khaizura, C. H. Kuan, B. W. Chieng, M. Nishibuchi, and S. Radu, *Front. Microbiol.* 9, 1, 2018.
17. P. Lodeiro, E. P. Achterberg, J. Pampín, A. Affatati, and M. S. El-Shahawi, *Sci. Total Environ.* 539, 7, 2016.

18. Hemlata, P. R. Meena, A. P. Singh, and K. K. Tejavath, *ACS omega* 5, 5520, 2020.
19. S. Chouhan and S. Guleria, *Mater. Sci. Energy Technol.* 3, 536, 2020.
20. D. Baruah, R. N. S. Yadav, A. Yadav, and A. M. Das, *J. Photochem. Photobiol. B Biol.* 201, 111649, 2019.
21. M. S. Mehata, *Chem. Phys. Lett.* 778, 138760, 2021.
22. F. A. Qais, A. Shafiq, H. M. Khan, F. M. Husain, R. A. Khan, B. Alenazi, A. Alsalme, and I. Ahmad, *Bioinorg. Chem. Appl.* 2019 2019.
23. D. Thatikayala, N. Jayarambabu, V. Banothu, C. B. Ballipalli, J. Park, and K. V. Rao, *J. Mater. Sci. Mater. Electron.* 30, 17303, 2019.
24. A. Chakravarty, I. Ahmad, P. Singh, M. U. D. Sheikh, G. Aalam, S. Sagadevan, and S. Ikram, *Chem. Phys. Lett.* 795, 139493, 2022.
25. F. Al-Otibi, S. K. Alkhudhair, R. I. Alharbi, A. A. Al-Askar, R. M. Aljowaie, and S. Al-Shehri, *Molecules* 26, 6081, 2021.
26. P. A. Lambert, *J. Appl. Microbiol.* 92, 46S, 2002.
27. P. Logeswari, S. Silambarasan, and J. Abraham, *J. Saudi Chem. Soc.* 19, 311, 2015.
28. H. M. M. Ibrahim, *J. Radiat. Res. Appl. Sci.* 8, 265, 2015.
29. S. Yallappa and J. Manjanna, *J. Clust. Sci.* 25, 1449, 2014.
30. H. F. Aritonang, H. Koleangan, and A. D. Wuntu, *Int. J. Microbiol.* 2019 2019.
31. K. D. Lee and P. C. Nagajyothi, *J. Nanomater.* 2011 2011.
32. R. W. Raut, V. D. Mendhulkar, and S. B. Kashid, *J. Photochem. Photobiol. B Biol.* 132, 45, 2014.
33. F. Hossain, O. J. Perales-Perez, S. Hwang, and F. Román, *Sci. Total Environ.* 466, 1047, 2014.
34. S. Rajendran, A. Mukherjee, T. A. Nguyen, C. Godugu, and R. K. Shukla, *Nanotoxicity: prevention and antibacterial applications of nanomaterials*, Elsevier (2020).
35. K. Rokesh, S. C. Mohan, S. Karuppuchamy, and K. Jothivenkatachalam, *J. Environ. Chem. Eng.* 6, 3610, 2018.
36. K. Roy, C. K. Sarkar, and C. K. Ghosh, *Spectrochim. Acta Part A Mol. Biomol. Spectrosc.* 146, 286, 2015.
37. W. Liang, T. L. Church, and A. T. Harris, *Green Chem.* 14, 968, 2012.
38. H. Veisi, S. Azizi, and P. Mohammadi, *J. Clean. Prod.* 170, 1536, 2018.

Bio-accessibility of Pre-synthesized Abhrak, Naga and Tamra Bhasma

Shailesh Kantak*, and Nilima Rajurkar

Department of Chemistry, Savitribai Phule Pune University, Pune

*Email: kantakshailesh@gmail.com

Received: 20.4.23, Revised: 25.4.23 Accepted: 26.4.23

Abstract:

Ayurvedic bhasmas play an important role in ayurvedic medicines and are useful in the treatment of various diseases. Pharmacokinetic studies involving estimation of bio-accessibility of bhasma will be useful in prescribing proper dosage of bhasma. Present paper deals with bio-accessibility of Abhraka, Naga and Tamra Bhasmas which were synthesized in our laboratory. It is revealed that the bio-accessibility of elements viz. K, Ca, Al, Fe, Na and Si in abhraka bhasma is more in gastric digestion than in gastro-intestinal digestion. Bio-accessibility of lead was found to be more in gastric digestion than gastro-intestinal digestion in Naga bhasma prepared by pisti and putapaka method while in bhasma prepared by jarana method it is more in gastro-intestinal digestion. In case of Tamra bhasma, bio-accessibility of copper is more in Gastro-intestinal digestion and it is further enhanced with anupana process, especially using ghee.

Key Words: Abhrak Bhasma, Naga Bhasma, Tamra Bhasma, Bio-accessibility, Ayurvedic bhasma

1.Introduction:

Ayurvedic bhasmas which are organometallic preparations, form very significant part of ayurvedic medicines and are useful in the treatment of various diseases. They are rejuvenating and have specific pharmacological activity. Being prepared from metallic raw materials these bhasmas may not be absorbed completely for circulation and hence pharmacokinetic study of bhasmas will play important role in prescribing the proper dosage of bhasma. Bio-accessibility determination is one of the important parameters in these studies. It is defined as a fraction of a dose of bhasma that is absorbed from its site of administration and reaches the general circulation. It will depend on its transfer across the

 DOI: 10.59143/isas.jisas.1.4.ORPO1427

membrane lining of Gastrointestinal tract. It further depends upon several factors such as particle size, particle shape, chemical phase etc. Survey of the literature on bhasma reveals that there are several reports in the literature on synthesis of ayurvedic bhasmas[1-6] but relatively less reports are available on characterization[7-9] and bio-accessibility studies[10-12]. Previous reports from our laboratory dealt with synthesis and characterization of Abhraka [13], Naga [14], Tamra[15], Rajat [9], Mandur [8], Yasad [16] and Pittal[17] bhasmas using modern analytical techniques. Present paper deals with bio-accessibility of Abhraka, Naga and Tamra Bhasma which were synthesized in our laboratory.

In general, bio-accessibility is affected by the type, composition of food and by the simulated gastro-intestinal conditions which may affect the distribution of initial species. Many factors that affect the bio-accessibility of a compound may be divided into exogenous factors such as complexity of the food matrix, the chemical form of the compound of interest, structure and amount of co-ingested compounds[18] as well as endogenous factors including mucosal mass, intestinal transit time, rate of gastric emptying, metabolism and extent of conjugation and protein binding in blood tissues. There are two approaches to estimate bio-accessibility: in-vitro and in-vivo techniques.

In-vivo studies are both expensive and laborious, and possibility of measuring certain parameters during the experiments are often limited [19] In this technique, bio available amount of an element of interest is estimated as the difference in the concentration of elements in ingest and excreta, using radio tracers.

In-vitro methods are rapid and inexpensive [20].It involves the simulation of the gastric and Gastro-intestinal digestive conditions in laboratory as the experiments are carried out under simulated digestive conditions. The results obtained by in-vitro methods are based on the formation of the digestive products that are soluble or dialyzable. However, these methods are efficient to identify potential food products as nutrient supplements**[21].** In-vitro method is routinely used to estimate the bio-accessible concentrations of essential elements in the diet. It is shown that the bio-accessible values obtained by these methods can be well related with that of human subjects [22] and many animal models [23]

2. Experimental

2.1 Material for gastric and gastro -intestinal digestion.

For preparation of gastric and gastro -intestinal digestion, Hydrochloric Acid was procured from Merck Chemicals, NaCl, $NaHCO_3$ from Aquafine Injecta Pvt. Ltd. and Pepsin and Pancreatin Bile salt were procured from Otto chemicals.

2.2. Evaluation of Bio-accessibility of different bhasma by in vitro digestion method

Bio- accessibility of Abhrak, Naga and Tamra bhasmas was determined by in vitro gastric and gastro- intestinal digestion methods. For this purpose, gastric juice and intestinal juice were used.

2.2.1 Preparation of gastric juice

Freshly prepared solutions of digestive enzymes were used in all the experiments. All the solutions were prepared in deionized water. Solution of pepsin (1:3000) was obtained by dissolving 6 g of pepsin in 100 ml of 0.15 M NaCl. The pH of gastric juice was adjusted by adding drops of 6 M HCl.

2.2.2 Preparation of Intestinal juice

Pancreatic solution was prepared by mixing pancreatic juice 2% and bile salt 0.2 %. The mixture was shaken for 1 min and pH was adjusted to 6.8 by adding drops of saturated $NaHCO_3$.

The pancreatic juice (2%) and bile salt solution (0.2%) were prepared by dissolving 2 g of pancreatin and 200 mg of bile salt respectively in 100 ml of 0.15 M of NaCl.

The detailed procedure for estimation of Bio- accessibility is shown schematically in Fig.1

The % bio-accessibility (% B) of each element in the all the bhasma samples was calculated using the following equation

$$\% B = \{ ([GD] \text{ or } [GID]) / [T] \} x100 \qquad --1$$

Where,

GD = concentration of element in Gastric digestion

GID = Concentration of element in Gastro-intestinal digestion

T = Total concentration of element in the sample

2.3 Elemental analysis of Bhasma

Elemental analysis of bhasma was carried out using AAS /ICPOES technique. The step-wise procedure is shown in Fig. 2

3 Results and Discussion

Synthesis of bhasma mainly consists of three processes

Shodhana Process: This process is mainly used to remove physical and chemical impurities of the starting material and increase the bio-accessibility and brittleness. Material is treated with liquids such as- sesame oil, butter milk, cow urine, kanji, horse gram decoction, lemon juice.

Marana Process: In this process, the product obtained after Shodhana process is treated with -mercury, arsenic, sulphur or herbal products. The resulting product will show change in original structure, composition and colour. Original inorganic form changes to organometallic form and becomes bio-acceptable.

Amrutikaran Process: Toxic impurities in the obtained product are removed in this process and total purity of bhasma increases. For this purpose, bhasma is treated with cow ghee or aloe vera juice.

The present work deals with the bio-accessibility studies of Naga bhasma prepared by three methods viz. Jarana method, pisti (amalgam) method and putapaka (herbal media) method. The details of synthesis are described in our previous report[14]. The work also deals with the bio-accessibility studies of abhraka bhasma which was prepared by three different methods wherein shodhana process is carried out with cow milk (method 1), Cow urine(method 2) and triphala decoction(method 3) ; Marana process with Jaggery + Juice of Ricinus Communis(method(1), Cyperus rotundus (Musta) decoction+ Calotropis procera juice (method 2), turmeric powder decoction + Borax (Method 3) while dhanya abhrak process (with paddy) and Amritikaran process(with Cow ghee) are common for all the three methods. The details of synthesis are described in our previous paper[13]. The Tamra bhasma was prepared by traditional method and details are given in our previous report[15] The obtained results are discussed below.

3.1 Bio-accessibility of Abhrak bhasma

The Bio-accessibility of Abhrak bhasma prepared by three different methods was carried out using ICPOES method and is shown in Tables 1 and 2.

An examination of Tables 1 and 2 shows that bio-accessibility of elements viz. K, Ca, Al and Fe in abhraka bhasma was found to be more in gastric digestion than gastro-intestinal digestion. While in commercial samples, the bio-accessibility of these elements was found to

be more in gastro-intestinal digestion. K, Ca, Al and Fe require acidic medium for their absorption. Hence Abhrak bhasma prepared by method 1, 2 and 3 will be absorbed in better way than commercial samples. % bio-accessibility of sodium was found to be higher than 100% in all the samples as sodium was used for pH control

In Ayurveda, the Abhrak bhasmas prepared by different methods are used for treating different diseases. Abhrak bhasma prepared by method-1 is commonly used for treating anemia and tropical sprue. The above analysis shows that Abhrak bhasma prepared by method 1 shows greater bio-accessibility for Fe than other two methods, although other two methods contain greater elemental concentration than method 1. method-2 is commonly used for treating chronic cough while Abhrak bhasma prepared by method-3 is commonly used for treating asthma, the bio-accessibility of Mg is enough to treat chronic cough. From the study it appears that Abhrak bhasma prepared by method -1 is more bio-accessible than other two methods.

3.2 Bio-accessibility of Naga bhasma

The Bio-accessibility of Naga bhasma prepared by three different methods was studied using AAS technique and results are shown in Table 3.

As can be seen from Table 3 bhasma prepared by putapaka method shows more bio-accessibility than jarana and pisti method. It is also observed that bio-accessibility of lead is more in gastric digestion than intestinal digestion in putapaka and pisti method. In case of jarana method bio-accessibility of lead was found to be more in Gastro-intestinal digestion than gastric digestion. Commercial bhasma sample also shows same trend as that of bhasmas prepared by putapaka method.

Naga bhasma prepared by different methods are used for treating different diseases and have their own merits e.g. bhasma prepared by jarana method is commonly used for upper respiratory diseases, that prepared by pisti method is used for colitis and that prepared by putapaka method is used for treating diabetes mellitus.

Our earlier report[14] revealed that Bhasma prepared by jarana and pisti method show lead sulphide while putapaka method shows PbO i.e. lead oxide form. PbS form is relatively less toxic. The bio-accessibility of lead in putapaka method is more than other two methods.

3.3 Bio-accessibility of Tamra bhasma and in different anupana

In order to increase the bio-accessibility of bhasma, ayurvedic literature suggests the use of Anupana[24] process. Anupana is that material which is consumed along with the bhasma

which helps to increase the palatability of bhasma and improves the digestion and absorption. It acts as a vehicle which carries the bhasma particles to their target site. In this paper an attempt has been made to study bio-accessibility of tamra bhasma with different anupana.

The bio-accessibility of Tamra bhasma prepared in different anupanas was studied using AAS technique for elemental analysis and results are shown in Table 4.

As can be seen from Table 4, Tamra bhasma mixed with different anupana like honey and piper longum mixture, ghee and fermented juice of Aloe vera shows more gastric and gastro-intestinal bio-accessibility than used as alone. As per literature, anupana is used to enhance bio-accessibility of Tamra Bhasma. The above observation shows increased bio-accessibility in anupana than without anupana. It is found that Gastro-intestinal bio-accessibility is more than gastric digestion. The bio-accessibility is more in both gastric digestion and gastro-intestinal digestion by using ghee as a anupana.

Conclusions:

The bio-accessibility of elements: K, Ca, Al, Fe, Na and Si in abhraka bhasma was found to be more in gastric digestion than gastro-intestinal digestion as expected. Same trend is observed for lead in Naga bhasma prepared by pisti and putapaka methods while in bhasma prepared by jarana method, bio-accessibility of lead is more in gastro-intestinal digestion. The bio-accessibility of copper (Tamra) was found to be more in gastro-intestinal digestion than in gastric digestion. Further, it is enhanced in anupanas, ghee shows more bio-accessibility than other two anupanas.

Acknowledgement:

Dr. Rajurkar is thankful to BCUD, Savitribai Phule Pune University for financial assistance.

Figures:

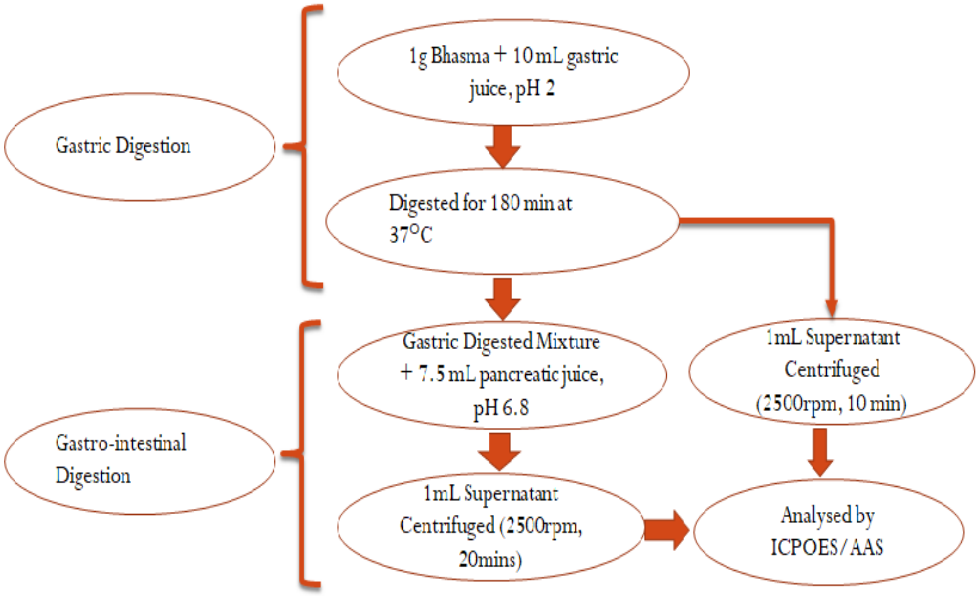

Fig.1 A Schematic diagram of Bio-accessibility estimation

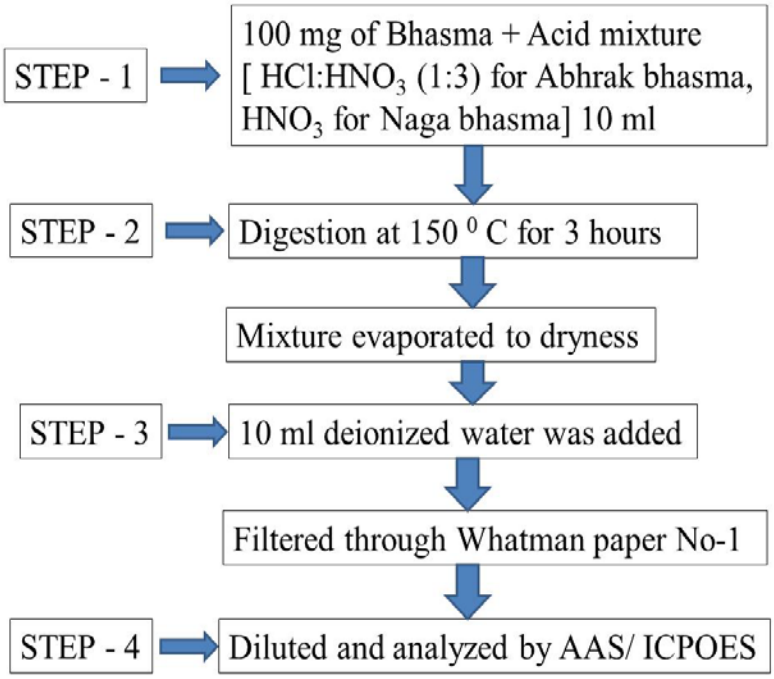

Fig.2. Schematic diagram for analysis by AAs/ICPOES

Tables:

Table 1: Bio-accessibility of elements in Abhrak bhasma

Method	Element	Concentration of Element / %	Bio-accessibility of Element / %	
			Gastric digestion	Gastro-intestinal digestion
Method -1	K	4.4	66.6	66.4
	Ca	6.2	67.1	52.7
	Al	2.64	44.3	0.7
	Mg	6.6	42.6	42.7
	Fe	7.4	12.9	0.4
Method-2	K	5.5	19.1	14.1
	Ca	7.3	26.2	9.0
	Al	7.2	23.7	0.02
	Mg	9.2	11.8	6.3
	Fe	11.4	1.84	0.01
Method -3	K	5.3	51.9	42.6
	Ca	5	20.2	8.9
	Al	4.5	36.4	0.03
	Mg	7.2	14.6	11.0
	Fe	14.3	0.2	0.02

Table 2: Bio-accessibility of elements in commercial Abhrak bhasma

	Elements	Concentration of Element / %	Bio-accessibility of Element / %	
			Gastric digestion	Gastro-intestinal digestion
Commercial -1	K	5.2	33.1	28.2
	Ca	5.5	35.3	38.7
	Al	5.3	22.3	17.4
	Mg	9.4	0.1	20.5
	Fe	11.8	3.5	1.4
Commercial -2	K	0.46	10.0	43.0
	Ca	11.4	0.1	26.5
	Al	0.01	10.0	16.5
	Mg	1.6	0.06	9.9
	Fe	37.5	0.002	0.05

Table 3: Bioaccessibility of Naga bhasma

Bhasma method		Concentration of lead / %	Bio-accessibility of lead / %	
			Gastric digestion	Gastro-intestinal digestion
Jarana method	with samanya shodhana	2.31	0.4	3.1
	without samanya shodhana	6.23	0.1	3.6
Pisti method	with samanya shodhana	5.56	5.6	1.6
	without samanya shodhana	2.69	3.1	3.7
Putapaka method	with samanya shodhana	2.28	8.7	2.1
	without samanya shodhana	2.90	8.9	8.7
Commercial -1		1.63	7.7	3.0
Commercial -2		1.45	7.3	4.8

Table 4 : Bioaccessibility of Tamra bhasma in different anupana

Anupana	Concentration of Copper / %	Bio-accessibility of Copper/ %	
		Gastric digestion	Gastro-intestinal digestion
Final Bhasma	59.8	0.4	1.0
Honey and Piper longum	59.8	1.4	4.1
Fermented juice of Aloe-vera	59.8	0.8	1.0
Ghee	59.8	1.0	1.4

References

1. S. M. Sondhi, V. K. Sharma and R. P. Verma, Indian Drugs, 33, 67, 1996.
2. S. K Singh, D. N. S. Gautam, M. Kumar and S. B. Rai, Indian J Pharm Sci., 72(10), 24, 2010.
3. M. D. Sangale, D.M. Suryavanshi, R.C. Chikate and B.R. Khot, Int. J. of Advance Scientific and Tech. research, 2(4), 336, 2014.

4. C.E. Lagad, R.S. Sawant and P.V. Bhange, Int. Research J. pharmacy, 3 (3), 162, 2012.
5. L. V. Krishnamurthy and R.T. Sane, Ind. Research J. of Chem. and Environ., 5, 65, 2001.
6. R. Chaturvedi and C. B. Jha, AYU., 32, 566, 2011.
7. T. K. Bhowmick, A. K. Suresh, S. G. Kane, A. C. Joshi and J. R. Bellare, J. of Nanoparticle Research, 11, 655, 2009.
8. N. S. Rajurkar, B. Kale and S.S. Kantak,Int. J of Pharm. & Bio. Archives, 6(3), 21, 2015.
9. N.S. Rajurkar, S.S. Kantak and V. Rathod, Environ.observer, 13, 209, 2013.
10. T. Patil Bhole and A. Wele, Int.J. Res. Ayurvedic Sci., II (4), 145, 2017.
11. C. S. Waghmare, S. Bidve, R. V. Gudi, M. B. Chwda, and S. Yadav, Int. J. Ayurvedic Med. 13 (2), 487, 2022
12. S. V. Rajan, H. Ankitha, S. Parhate and Rakesh Singh Thakur, J. Ayurveda integr. Med. Sci,1, 102, 2023
13. S. S. Kantak, N.S. Rajurkar and P.V. Adhyapak, J. Ayurveda Integr. Med Sci, 11, 236, 2020.
14. S. S. Kantak and N.S. Rajurkar, J. of Applicable Chem., 6 (2), 291, 2017.
15. S S. Kantak., T. Nesari and N.S. Rajurkar, Proceeding of DAE-BRNS Fifth symposium on Nuclear Analytical Chemistry [NAC-V], Mumbai, India, PP. 20, 2014.
16. B. Kale and N.S. Rajurkar The Pharma innovation journal, 7(1), 119, 2018.
17. B. Kale and N.S. Rajurkar, J. ISAS, 1(3), 77, 2023.
18. S. Scholz and G., Int J Vitam Nutr Res., 77(3), 224, 2007.
19. L. G Danielsson., A. Zarpen and A. W. Glynn, Analyst, 120, 713,1995.
20. D. Miller, B. Schricker, R. Ramussen and D. Van Campen, Am. J.Clin. Nutr., 34, 2284, 1981.
21. D. Van Campen, and R. P. Glahn, Field Crop Research, 60, 93, 1999.
22. E. Menson and J. Cook, American Journal of Clinical Nutrition, 32, 804, 1979.
23. A. Forbs, C. Adams, M. Arnuad, C. Chichester, J. Cook, and B. Harrison, American Journal of Clinical Nutrition, 49, 225, 1989.
24. A Kumar, A.G.C. Nair, A.V.R. Reddy, A.N. Garg, Biol.Trace Element Res. 109, 231, 2006.

Solution-Processed Nanostructured CdS Thin Film with Improved Optoelectronic Properties

Ravi Mudike[a], Sanjay R. Dhage[*b], Prasanna D Shivaramu[a], Dinesh Rangappa[*a]

[a]*Department of Applied Sciences (Nanotechnology), Visvesvaraya Technological University, Centre for Postgraduate Studies, Muddenahalli, Chikkaballapur-562 101, India.*

[b] *International Advanced Research Centre for Powder Metallurgy and New Materials (ARCI), Hyderabad, India.*

* dhage@arci.res.in, dineshrangappa@gmail.com

Received: 11.3.23, Revised: 27.4.23 Accepted: 28.4.23

Abstract

Nanostructured CdS thin films are essential for efficient electron transport and they act as an ideal buffer layer in CIGS/CZTS/CdTe thin-film solar cells. Herein, low-temperature processed CdS nanostructured thin film on a glass substrate by chemical bath deposition for its application in optoelectronic devices is reported. As synthesized, CdS nanostructured thin films are exhibited polycrystalline, confirmed using X-ray diffraction/transmission electron microscopy. Further, polycrystalline (hexagon/cubic) nature reconfirmed by Raman band at 305 cm^{-1} of as-grown films. The surface morphology and EDS of CdS thin films reveal uniformity on the surface with non-cuboid nanoparticles and nearly stoichiometric. The optical band gap of CdS nanostructured thin films was found to be 2.3 eV, properties indicating its suitability as a buffer layer in CIGS/CZTS thin-film solar cells.

Keywords: CdS thin film, nanostructure, chemical bath deposition, Raman Spectra.

1. Introduction

Cadmium sulfide (CdS) is the most promising n-type semiconductor material in thin-film (CdTe/CIGS/CZTS) solar cells and next-generation optoelectronic devices; because of its direct bandgap (2.42 eV)[1], high absorption coefficient[2,3], having an absorption edge at 510 nm[4,5]. Researchers have reported the confirmable coating of CdS nanostructured film via a solution-based approach on CdTe/CIGS/CZTS layer to fabricate a solar cell device[6–9]. It is

 DOI: 10.59143/isas.jisas.1.4.KDJF7931

inexpensive and forms a better interface with an absorber material layer. The better interface minimizes the recombination and leakage current at the junction[10,11]. The CdS nanostructured film as buffer layer used in solar cells have exhibited an efficiency of 23.35% for CIGS and 12.6% for CZTSSe[12,13].

CdS films are durable due to the lower lattice miss matching with the absorber layer and it offers faster electron transport at the interface. CdS layer can be deposited on the solar absorber layer using vacuum and non-vacuum techniques. Vacuum evaporation (VE)[14], chemical bath deposition (CBD)[15,16], spray pyrolysis (SP)[17], chemical vapor deposition[18], successive ionic layer adsorption and reaction[19] are some of the most effective methods for CdS thin film deposition. Among these, the CBD technique is more popular because of its cost-effective and low-temperature solution process. In addition, CdS films with high optical absorbance, low electrical resistivity, less recombination losses and better crystallinity can be obtained by this method which are very important for solar photovoltaic applications[20–22]. Electrical properties such as resistivity and the optical absorbance of CdS thin films strongly depend on the preparation and deposition conditions[23,24]. In this study, we have optimized the process conditions for the deposition of nanostructured CdS thin films to obtain high optoelectronic properties for its application in devices. The film's structural, electrical and optical properties were investigated and presented.

2. Experimental

2.1. Materials

Cadmium sulfate ($CdSO_4$, purity 99.99%), thiourea (CH_4N_2S, purity 99.0%) and ammonium hydroxide (25% NH_4OH) were purchased from Sigma-Aldrich and further used without purification.

CdS nanostructure film growth process and characterization

The CdS precursor solution was prepared by dissolving cadmium sulfate (0.16 M), thiourea (0.6 M) and ammonium hydroxide (7.5 ml) into DI-water at room temperature. Before the deposition of films, the soda-lime glass was cleaned following the standard procedure reported[25]. Subsequently, the as-prepared solution was used to grow CdS nanostructured films on a cleaned soda-lime glass substrate via chemical bath deposition process at 60 ^{0}C with various deposition times of 15 and 35 min and pH of the solution maintained at 10. For the 15 min deposition time of CdS thin-film and the 35 min deposition time CdS thin-film hereinafter called CdS-A and CdS-B, respectively. After the deposition reaction, the formed yellow precipitate (collected using the centrifugation process for analysis) and as grown

nanostructured films on soda-lime glass substrate were annealed at 300 ^{0}C for 2 h in the muffle furnace.

The morphology and elemental compositions of CdS powder and films were studied using scanning electron microscopy (Hitachi S-4300 SE/N, USA). The formation of the CdS phase was confirmed using the X-ray Diffraction (XRD) analysis (D8 Advance, Bruker) and the nanoparticle size was studied by Transmission Electron Microscopy (TEM) (FEI Tecnai G20 20 XTWIN). The film thickness was estimated using the X-ray Fluorescence Spectrometer (XRF). A Varian Cary 5E UV-Vis-NIR spectrophotometer was used to record the optical transmittance in the 250-2000 nm wavelength range.

3. Results and discussion

In photovoltaic devices, n-type semiconducting material plays a crucial role in transporting the charge carriers. It improves the open-circuit voltage of the device, here n-type CdS nanostructured films on a soda-lime glass substrate by a low-temperature solution process with variable time durations (15 and 35 min) and their digital photographs are shown in **Figure 1(a).** The crystallinity and phase of CdS nanostructured thin films and Nanoparticles' structural properties were investigated using TEM, XRD, and Raman spectroscopy. **Figure 1(b)** shows the XRD pattern of CdS nanostructured films on the glass substrate, it reveals the polycrystalline nature of CdS film. The peaks position at 25.1^0, 26.7^0, 28.2^0, 31.02^0, 44^0 and 52.03^0 indexed are corresponding to the (100), (111), (101), (200), (220) and (111) planes of cubic phase (JCPDS No.: 04-014-0285) and hexagonal phase (JCPDS No.: 01-074-9664), confirming the mixed-phase CdS film. Moreover, the diffraction peak corresponding to CdO can be seen in CdS-A and CdS-B samples. It is due to partial oxidation of cadmium and the evaporation of sulfur by annealing the films at 300 ^{0}C, supported by the earlier report [26]. However, the diffraction peaks corresponding to CdO have not appeared in the nanoparticle sample. The crystalline size was calculated using the Debye-Scherrer formula, and the average crystalline size of 8-12 nm was obtained. Interestingly, the CdS nanoparticle diffraction peaks have low-intensity broader peaks due to the apparent effect of crystalline size.

CdS nanostructured thin films were scratched and removed from the glass substrate and dispersed in the solvent to reconfirm the crystallinity and particle size by TEM **Figure 1(c)** shows the SAED pattern of CdS nanostructures indicating high crystallinity of the film. The SAED pattern reveals that the CdS nanostructure is polycrystalline and agrees with the XRD pattern. The reflected ring pattern was indexed and these rings correspond to the (111), (200),

(220) and (111) diffraction planes. Furthermore, CdS structural properties were also determined and reconfirmed using Raman spectroscopy. The Raman spectrum revealed two longitudinal optical (LO) phonon peaks at ~ 300 cm^{-1} and ~ 600 cm^{-1}, as shown in Fig. 1 (d). The hexagonal CdS Raman shift LO modes were observed at the same wavenumbers [18]. We observed that the 300 cm^{-1} peak is a significant phonon peak for all cases. FWHM reveals that CdS nanostructure films have higher crystallinity than CdS nanoparticles. However, the peak intensity is high and negligible spectral peak shift, reconfirming the identical quality of the film. It is worth mentioning here, the structural properties of the CdS nanostructured thin film grown on glass substrate are compared with the CdS nanoparticle, briefed in **Table 1**.

Figure 2. shows the surface morphology and elemental analysis of CdS nano-structured films at variable deposition times. The estimated particle size with a non-cuboid shape can be easily noticed from the surface morphology. **Figure 2(a),** the surface morphology of CdS-A nanostructured film deposited at 15 min reaction time, reveals a more agglomerate surface with an average particle size of 65 nm. Subsequently, elemental analysis was carried out at the particular area and the EDS spectra were inset of **Figure 2(a).** The EDS spectra provided the possible elemental composition with ratio, confirming the presence of Cd and S. Further increase in the reaction time from 15 to 35 min. The surface morphology/elemental composition of the CdS-B film is shown in **Figure 2(b),** indicating an increase in the particle size. In comparison, 35 min grown CdS nanostructured film has good adhesion, high particle size (an average particle size ~ 105 nm). However, it has more sulfur content (the EDS spectra inset **Figure 2(b)**) than the 15 min nanostructured film. TEM imaging was performed on the dispersed CdS nanoparticles to investigate the morphology, it reveals the particle size 10 nm and agrees with XRD data. CdS nanostructured thin film thickness was measured by X-Ray Fluorescence Spectrometer and found to be 125 nm and 194 nm for CdS-A and CdS-B thin films, respectively reiterate the increase in reaction time can lead to obtaining films with the higher thickness.

Figure 3.(a) shows the spectral transmittance curves of CdS-A & CdS-B nanostructured thin films recorded in UV-Vis-NIR spectrometer. The direct bandgap (E_g) of the films was determined by extrapolating the linear portion of the $(\alpha h\upsilon)^2$ versus $h\upsilon$ plot and taking the intercept on the X-axis, as shown in **Figure 3. (b).** The bandgap was calculated as 2.35 eV and 2.37 eV for CdS-A and CdS-B nanostructured thin films. Slight variation in bandgap

could be attributed to increasing deposition time, resulting in crystallinity improvement, in line with the earlier reported work[27].

4. Conclusion

The nanostructured CdS thin films via solution process were successfully prepared. The CdS nanoparticles are randomly oriented polytype structures or mixed type structures rather than hexagonal greenockite or cubic hawleyite structures. The hexagonal peaks are at 25.1^0 and 28.2^0 identified at the shoulder of the significant cubic (111) plane. Due to a longer reaction time, the grain size increased and nucleation enables lateral grain growth in the CdS-B film. The optical band gap energy of CdS film changes from 2.35 eV and 2.37 eV on increasing the deposition time from 15 to 35 min. The presented approach opens the possibility of growing crystalline CdS nanostructured architecture on the desired substrate at low temperatures for a range of optoelectronic applications such as solar cells.

Figures:

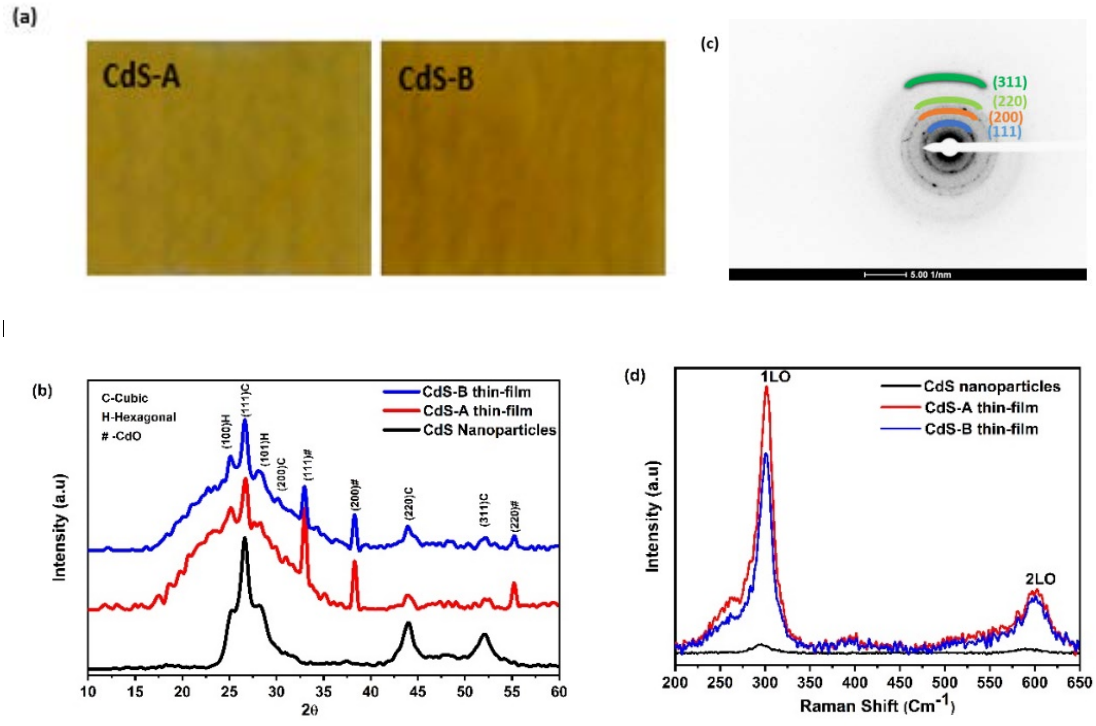

Figure 1. (a) Digital photographs, (b) XRD pattern, (c) TEM SAED pattern and (d) Raman spectra of CdS thin films deposited on glass at a variable time and of nanoparticles.

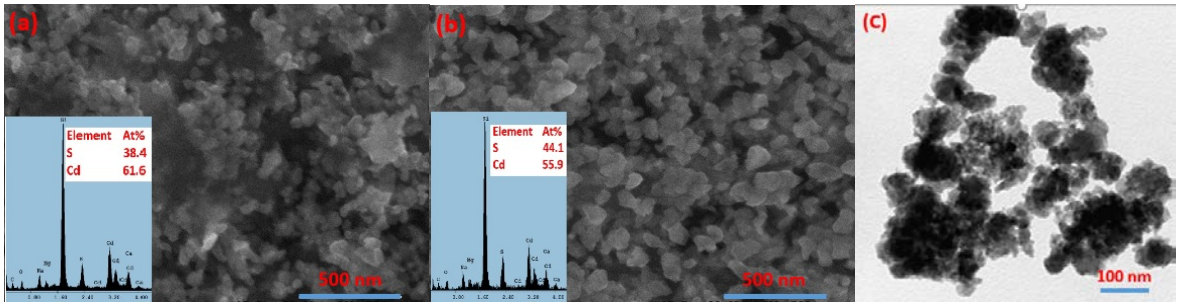

Figure 2. FESEM and EDS spectrum of CdS films deposited at (a) 15 min, (b) 35 min and (c) TEM morphology of CdS powder.

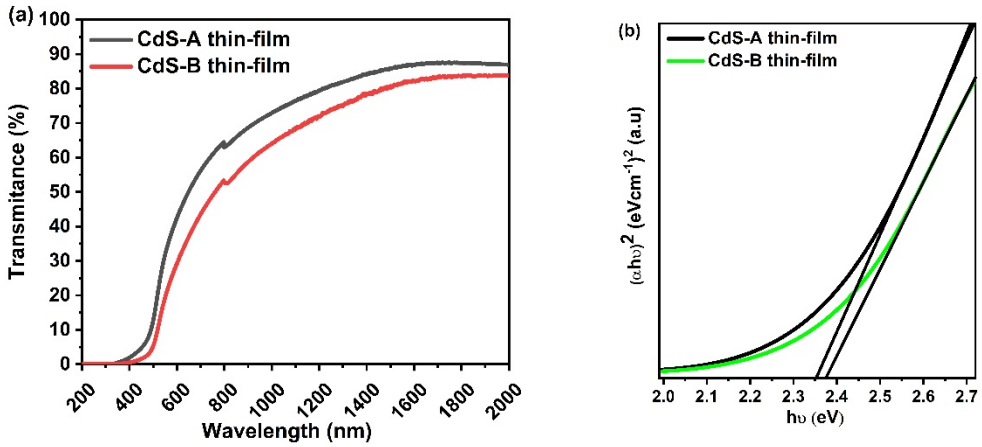

Figure 3. (a) Transmission spectra of CdS-A & CdS-B thin films and (b) $\alpha h\upsilon)^2$ versus $h\upsilon$ plot of CdS-A and CdS-B thin films.

Tables:

Table 1. Raman spectrum indexing of CdS NPs and CdS nanostructures films.

Sample Name	**Raman shift (cm^{-1})**	
	1LO	**2LO**
Standard CdS single crystal	306	604
CdS NPs	296	590
CdS-A nanostructured film	301	603
CdS-B nanostructured film	300	601

References

1 Y. Chen, W. Zhong, F. Chen, P. Wang, J. Fan and H. Yu, *J. Mater. Sci. Technol.*, **121**, 19, 2022.

2 M. Huang, C. Liu, P. Cui, T. Wu, X. Feng, H. Huang, J. Zhou and Y. Wang, *Environ. Sci. Technol.*, **55**, 13132.2021.

3 A. Hamid Rather, T. Umair Wani, R. Saleem Khan, A. Abdal-hay, S. Rather, J. Macossay and F. A. Sheikh, *Mater. Sci. Eng. B*, **286**, 116022, 2022.

4 Y. Lei, K. H. Ng, Y. Zhang, Z. Li, S. Xu, J. Huang and Y. Lai, *Chem. Eng. J.*, **434**, 134689,2022.

5 J. Yao, L. Wang, H. Zhou, Z. Xie, X. Zeng and C. Liu, *J. Colloid Interface Sci.*, **616**, 858, 2022.

6 R. Mudike, C. Sabbanahalli, J. B. Sriramoju, A. Bheemaraju, G. Halligudra, M. Muniyappa, M. P. Narayanaswamy, A. K. CS, P. D. Shivaramu and D. Rangappa, *Mater. Res. Bull.*, **146**, 111606, 2022

7 R. Mudike, A. Bheemaraju, T. Rasheed, N. Singh, S. R. Dhage, P. Doddakunche Shivaramu and D. Rangappa, *Ceram. Int.*, **48**, 35666, 2022.

8 G. K. U. P. Gajanayake, A. A. I. Lakmal, D. S. M. De Silva and B. S. Dassanayake, *J. Mater. Sci. Mater. Electron.*, **34**, 508, 2023.

9 O. Ahmad, I. Qasim, S. M. Hasnain, Z. ul Abdin, M. F. Nasir, M. I. Malik and A. Rashid, *Org. Electron.*, **117**, 106781, 2023.

10 H. Heriche, Z. Rouabah and N. Bouarissa, *Optik (Stuttg).*, **127**, 11751–11757, 2016.

11 M. T. Winkler, W. Wang, O. Gunawan, H. J. Hovel, T. K. Todorov and D. B. Mitzi, *Energy Environ. Sci.*, **7**, 1029, 2014.

12 M. Nakamura, K. Yamaguchi, Y. Kimoto, Y. Yasaki, T. Kato and H. Sugimoto, *IEEE J. Photovoltaics*, **9**, 1863, 2019.

13 W. Wang, M. T. Winkler, O. Gunawan, T. Gokmen, T. K. Todorov, Y. Zhu and D. B. Mitzi, *Adv. Energy Mater.*, **4**, 1, 2013.

14 S. Chander and M. S. Dhaka, *Thin Solid Films*, **638**, 179, 2017.

15 S. R. Dhage, H. A. Colorado and H. T. Hahn, *Mater. Res.*, **16**, 504. 2013.

16 P. Uday Bhaskar and S. R. Dhage, *Mater. Today Proc.*, **4**, 12525, 2017

17 M. Shkir, I. M. Ashraf, S. AlFaify, A. M. El-Toni, M. Ahmed and A. Khan, *Ceram. Int.*, **46**, 4652,2020

18 M. A. Buckingham, A. L. Catherall, M. S. Hill, A. L. Johnson and J. D. Parish, *Cryst.*

Growth Des., **17**, 907,2017.

19 C. E. Perez-Garcia, S. Meraz-Davila, G. Arreola-Jardon, F. De Moure-Flores, R. Ramírez-Bon and Y. V. Vorobiev, *Mater. Res. Express*, 7,015530,2020.

20 L. Guogen, C. Zimeng, B. R. B., P. Jingong, G. G. E. and C. K. K., *Conf. Rec. IEEE Photovolt. Spec. Conf.*, pp.003750,2011.

21 J. F. Akter, S. M. Zaman and R. M. Junaebur, *Mater. Renew. Sustain. Energy*, **8**, 1,2019

22 M. Abdulhur, K. Mankoshi, F. I. Mustafa, N. J. Hintaw, K. Kushiya, Y. Ohtake, P. U. Londhe and A. B. Rohom, in *Journal of Physics: Conf. Series*, pp. 1, 2018.

23 M. Maghouli and H. Eshghi, *Superlattices Microstruct.*, **128**, 327, 2019.

24 V. D. Moreno-Regino, F. M. Castañeda-de-la-Hoya, C. G. Torres-Castanedo, J. Márquez-Marín, R. Castanedo-Pérez, G. Torres-Delgado and O. Zelaya-Ángel, *Results Phys.*, **13**, 102238, 2019.

25 B. S. Yadav, A. C. Badgujar and S. R. Dhage, *Sol. Energy*, **157**, 507, 2017.

26 H. A. Colorado, S. R. Dhage and H. T. Hahn, *Mater. Sci. Eng. B Solid-State Mater. Adv. Technol.*, **176**, 116, 2011.

27 D. Petre, I. Pintilie, E. Pentia, I. Pintilie and T. Botila, *Mater. Sci. Eng. B Solid-State Mater. Adv. Technol.*, **58**, 238, 1999.

John- Sivanandan Achari Isotherm Method for the Determination of Surface Area of Porous Materials: Analysis of Granular Activated Carbons

Raichel Mary Lopez and V. Sivanandan Achari*
School of Environmental Studies
Cochin University of Science and Technology
Kochi-682022, Kerala, India
Email: vsachari@cusat.ac.in/raichel6lopez@gmail.com

Received: 11.4.23, Revised: 26.4.23, 28.4.23, 30.4. 23; Accepted: 30.4.23

Abstract

John –Sivanandan Achari isotherm equation*log log* C_e*= C+n log* q_e,has many advantages for the structural characterization of porous materials. Linear plot of *log logCe* versus *log* q_e conform to a straight line and subsequent extrapolation of amount adsorbed (q_e), to the *x*axis. This way one can directly determine the monolayerq_m*(J-SA)* and hence the specific surface area (SA m^2/g) of the material.This can be analytically proved by applying the method in any type of solid-liquid equilibrium adsorption data. In this study, adsorption of methylene blue (MB) dye molecules on modified granular activated carbon (GAC) has been attempted to determine the porosity, and surface area by the new method. The solids are GAC 383 (native carbon- coconut shell based), GACO383 (native carbon oxidized) and a new carbon (GACOLaO1273). This carbon is prepared in the laboratory by steam activation after incorporating GAC383with Lanthanum*(*La^{3+}*)* ions. Carbons are tested in batch reactors with fixed MB concentrations by adsorptive techniques. The isotherm model behavior of the carbons are hereby reported using John - Sivanandan Achari isotherm (J-SA) equation using specific adsorption data. Porous material category as IUPAC type, constants and parameters are further evaluated with Langmuir, Freundlich, Dubinin - Radushkevich isotherms. It is seen that the isotherm followed the features of micro porous materials on using John – Sivanandan Achari (J-SA) isotherm. Porosity and surface area determined are found to give agreeing results on comparing with other isotherm models. This research is intended to highlight the significance of John and John-Sivanandan Achari (J-SA) isotherms as a tool for material characterization studies- a model originated as Indian analytical scientific skill.

Keywords: *John-Sivanandan Achari (J-SA) Isotherm; Activated carbon; Methylene Blue (MB); Adsorption isotherms; Specific surface area.*\

1. Introduction

John & John – Sivanandan Achari isotherm model methods are known are developed by Dr. P. T. John (Formerly Scientist, National Physical Laboratory, New Delhi) applied by Dr. V. Sivanandan Achari (School of Environmental Studies, Cochin University of Science &Technology, Cochin) to study textural behavior of carbons & porous materials. Porosity and surface area are the prominent structural parameters of any kind of porous materials used in industrial applications. These are most pertinent textural properties to report the adsorption efficiency of materials when used in separation and purification[1] process.

Langmuir [2] in 1918 proposed the monolayer coverage concept by assuming a monolayer formation on the homogeneous surface in which the reciprocal slope of the plot gives the monolayer volume. Brunauer–Emmett–Teller (BET) [3] method is the widely used method for the determination of surface area of porous materials using the monolayer adsorption capacity (V_m) and molecular cross-sectional area (0.162 nm^2 or 0.162 x 10^{-18} m^2). Calculations of Specific surface area (SSA) in BET equation method consider the *C* value as a constant for type I porous material behaviour. Further evaluation of micropore volume involves the use of many methods. By which the prominent one is the *t*-plot method [4] comprises an empirical comparison of an isotherm with a non-porous reference material of similar composition. In order to overwhelm the use of a standard multilayer thickness curve, later on α_s isotherm was introduced. In which the standard isotherm is plotted in a reduced form $(n/n_x)_s$. The plot $(n/n_x)_s$ versus relative pressure (p/p_0) where n_x is generally taken as the amount adsorbed at p/p_0 0.4. The micropore capacity was found by extrapolating the linear section of α_s plot. Another method for the determination of micropore volume was centered on Dubinin's pore volume filling theory [5] plotted with $log\ q$ versus $log^2(p_0/p)$ provided the linear portion of the plot extrapolated to deliver the micropore volume. Later on, John isotherm [6–9] was introduced by a renowned Indian Scientist P.T. John, with proper scientific explanation for the phases in adsorption plots of porous materials. The isotherm displayed with distinct kinks corresponds to the pore filling mechanisms with amount adsorbed at each phase obtained by extrapolating each kink to abscissa. Constant *n* slope of the each phase is a measure of adsorption efficiency known as *adsorbablity* constant by John. Isotherm constants and parameters can reveal many features of materials. Constant *C* in BET isotherm later becomes known that which is actually not so. Hence, reported the introduction of *I* plot by Pomonis 2005 [10] ,considering a non-linear plot whose kink (point of inflection) will deliver the monolayer volume.

Material behavior is determined from equilibrium isotherm analysis of *solid –gas* or *solid-liquid* system using a set of model calculations and proper interpretation of parameters or constants. In adsorption methods, to ascertain monolayer volume (v_m) or monolayer quantity (q_m) adsorbed, we can apply different adsorption isotherm equations. John and John – Sivanandan Achari (J-SA) isotherm equations[7]are well-established mathematical models, from which we can directly obtain the adsorptionmonolayer (v_m/q_m) for adsorption system follows Type I, II & IV features. It is found that, the method is successful for determining adsorption efficiency, porosity and surface area of many porous materials according to the category to which both *solid-gas* and *solid-liquid* adsorption systemsbelongs[11].

Recent literature in chemistry, material science, separation & purification cites many carbon porous materials are tested for their efficiency using the John & John –Sivanandan Achari (J-SA) isotherm methods. Known are coconut shell based granular activated carbon incorporated with cerium compounds reported[12] to have phenol 224.2mg/g adsorbed onto cerium nitrate incorporated carbon (GAC CN1273) activated at 1273K. For *p*-nitrophenol molecules, the amount adsorbed was found to be 653.6mg/g and for methylene blue molecules the amount was 299.40mg/g. Zn^{2+}/nano ZnO[13] loaded coconut shell based granular activated carbon was taken for the adsorption study against *p*-nitrophenol solution and found that granular activated carbon incorporated with Zn^{2+} activated at 1073K (GACZC1073) has a higher adsorption capacity (490.2mg/g) than the basic carbon GAC383 (340.1mg/g) [14]. Zr^{4+}/nano ZrO_2[15] incorporated coconut shell based granular activated carbon steam activated at 1273K exhibited a 43% more removal of *p*-nitrophenol (478.5mg/g) than the basic carbon GAC383 suggests that, Zr^{4+} generates more accessible pores for the *p*-nitrophenol molecules. Method is particularly useful to apply for the performance evaluation of any porous material applied in adsorption treatment reactor systems described in the following sections.

Methylene Blue (MB) dye bears many industrial & analytical applications. Hence, has been used for the adsorption study of many porous solids like granular activated carbon (GAC), charcoal, graphite and silica. It is used mostly as a prominent organic molecular adsorbate used in analytical chemistry as is one with known cross-sectional area (1.20 nm^2) [16] applied in many adsorption studies. In this study, we make an attempt to explain how John – Sivanandan Achari (J-SA) isotherm method is suitably used to determine adsorption monolayer q_m and specific surface area *SA* m^2/g of granular activated carbon (GAC) using methylene blue (MB) dye in liquid phase under equilibrium batch reactor conditions.

2. Experimental

Commercially available coconut shell based granular activated carbon (GAC) obtained from Indo-German Carbons Limited, Kochi, India of size 12x40 mesh size (0.9-1.1mm) was used as the starting material.Specifications of the starting material used in the present study as supplied by the manufacturerwere: iodine number (110mg/g), surface area (1150 m^2/g), apparent density (0.50g/cc), moisture (5%), ash (4%) and pH 9-11. Before use, the GAC was washed with distilled water to remove impurities present on the surface and then dried at 383 K and marked as GAC383.

A portion of GAC383 was oxidized with 12.9% $HNO_3$and refluxed for 3 hours, thereafter filtered. The procedure was repeated by adding a fresh solution of HNO_3 and distilled water in the same ratio as the previous. A reaction time of 4 hours was then maintained.After oxidation, the samples were filtered and thoroughly washed with hot distilled water until the pH became neutral, then dried in an air oven for 24 hours at 383 K . The product obtained by the oxidation are labelled as GACO383.A portion (10g) of GACO383 carbons was taken in a conical flask and was impregnated within a dispersion of nano Lanthanumoxide (La_2O_3) and the content was then carbonized under steam activation at 1273 K in a specially designed temperature programmed furnace. The product was labelled as GACOLaO1273.

Methylene Blue (MB) ($C_6H_{18}N_3SCl.3H_2O$, MW: 319.85)of analar grade (Merck) of purity 99.9% was used to prepare different concentrations of MB ranging from 25-1500mg/L with GAC adsorbent dosage of 1.0g/L for the equilibrium batch adsorption tests. The amount adsorbed at equilibrium (q_e) was calculated using the equation (1).

$$q_e = \frac{(C_0 - C_e)V}{W} \quad \text{.....(1)}$$

where C_0 is the initial concentration in *mg/L*, C_e is the concentration at equilibrium *(mg/L), V* is the volume of the solution and *W* is the mass of the carbon (g).The quantity adsorbed was measured using spectrophotometer (Systronics) at 665 nm.The adsorption equilibrium data was used to fit John - Sivanandan Achari isotherm (J-SA) equation to evaluate the monolayer adsorption capacity, adsorption efficiency, porosity and surfacearea. From the monolayer adsorption capacityobtained q_m*(g/g)*,the surface area can becalculated[17]as

$$SA(m^2/g) = \frac{q_m(g/g) \times 6.023 \times 10^{23} \times 1.20 nm^2 \times 10^{-18}}{319.85} \quad \text{.....(2)}$$

Where$q_m$is the monolayer adsorption capacity,*1.20 nm^2* is the cross-sectional area of MB,and*319.85(g/mol)*is the molecular weight of methylene blue.Isotherm methods based on Langmuir, Freundlichand Dubinin- Radushkevich (D-R) isotherm methods are also used to

determine respective monolayer adsorption capacities. Hence, the surface area of the granular activated carbon under study were critically evaluated and agreement of test results are enumerated.

2. Results and Discussion

John (J) isotherm and *John–Sivanandan Achari* (*J-SA*) isotherm [18]are mathematical models, to test adsorption potential of porous materials from solid-gas and solid–liquid adsorption systems respectively. Though the research on *John* isotherm model had been live from early sixties onwards, more rigorous analysis of isotherm data by various adsorption systems in *solid- liquid*equilibria is a focus of recent research to promote Indian scientific analytical skills.Testing of this isotherm model for new carbonaceous materials which are either activated under a set of conditions, or commerciallyprocured productsor using the data from published literature for the study of the model are common practices of evaluation. In all studies, the same isotherm data is subjected to regression analysis using the John isotherm models and further compared to the other known isotherms.

Comparison of the isotherm constants and analyses of the adsorption phases on the linearization procedures and evaluation of pore volume and subsequent surface area determination are the common steps followed. Mathematical expressions of the new isotherms are shown as linear form in equations (3) and (5). Pore filling phenomena occurring on a porous material is very distinct in this isotherm plots as straight lines joined at kinks with lines with definite slopes, hence the method is otherwise called phase change method (Fig.1).

2.1. John Isotherm for (Solid-Gas) Systems

$$\log \log P = C + n \log V \quad \text{.....(3)}$$

$$\textit{Where;}\quad P = p/p_0 \times 10^N \quad \text{.....(4)}$$

and '*V*' is the amount adsorbed (cm^3/g) *STP* at relative pressure (p/p_0).

2.2. John–Sivanandan Achari (J-SA) Isotherm for (Solid-Liquid) Systems

John–Sivanandan Achari (*J-SA*) Isotherm for (solid-liquid) equilibrium adsorption systems are given by

$$\log \log C_e = C + n \log q_e \quad \text{.....(5)}$$

Where; $C_e = C_e \times 10^N$ .....(6)

$q_e$is the amount of MB adsorbed (*mg/g*) and C_e is the concentration of adsorbate (*mg/L*) is known to be an ideal isotherm model to describe solid-liquid adsorption reactor systems and characterization ofporous materials. *N* is an integer usually in between *3 to 8* so as to make *log* $C_e$positive and *log log*$C_e$can be made. Here N is taken as 4.

The John isotherm models are originated based on Polanyi potential theory. Many well-known adsorption equations like Langmuir equation, Dubinin-Radushkevich equation, Henry's equation, de Boer-Swikkers equation, Frenkel-Halsey-Hill equation and Temkin equation can be derived from John Isotherm equation with minor approximations. John and Achari (2002)[7] enumerated the advantages of John isotherm model on comparison to other conventional isotherm models.

Logarithm of monolayer capacity of any adsorbent material is related to equation by

$$\log q_e = \frac{(\log \log C_e - C)}{n} \quad \text{.....(7)}$$

where *C* and *n* are the intercept and slope respectively for the plots are drawn. If there are cases where equilibrium constants does not give a possible value in its *log* form, C_e is multiplied by an integer, that is $C_e = C_e \times 10^N$ where *N* is an integer so chosen that lowest *log log* C_e of the data is positive. The value of *log* $q_e$corresponding to the highest *log log* C_e on the extrapolated line is taken, whose antilogarithm gives the monolayer capacityq_m*(J-SA)*for the isotherm with one adsorption phase (for Type I isotherms as per IUPAC-2015 classification[19], given by most microporous materials).

The isotherms of carbonaceous microporous materials, GAC383, GACO383 and GACOLaO1273 (Fig.2) have a steep rise in the initial stage of adsorption at lower concentration ranges, progressed well to attain saturation at higher ranges. The steep rise is because of micropores. These pores are preferentially filled fast as evidenced by a steep adsorption front. After this, the sub-monolayers were filled as these higher energy sites are unoccupied. At equilibrium concentration every carbon undergoes selective pore filling, and mesopores were filled leading towards the formation of a narrow hysterias loop in their solid-gas equilibrium isotherms particularly adsorbed with N_2 at 77K.

Methylene blue (MB) isotherm of GAC383, GACO383 and GACOLaO1273 was constructed and showsGACOLaO1273 has a strong affinity to MB than that of GAC383 and GACO383 attains saturation at higher concentration ranges.

2.3. John - Sivanandan Achari (J-SA) Isotherm Model Evaluation

The J-SA equation is very much useful in determining the monolayer adsorption capacity of the adsorbent in liquid phase[8]. The J-SA isotherm plot is given by the equation

$$\log\log C_e = C + n\log q_e \qquad (4)$$

Where q_e is the amount of adsorbate adsorbed at equilibrium (mg/g), $C_e$is the Concentration of adsorbate is the liquid phase obtained from the equilibrium adsorption isotherm study and *'n'* is the adsorption constant known as John adsorption capacity, is a measure of adsorption efficiency of the material. John-Sivanandan Achari isotherm plot with *log log* C_e against *log* q_e shown in the Fig.3 gives a single phase corresponds to the micro porous Type I compounds [7]. The end point of the plot when extrapolated to the *x* axis gives the monolayer volume q_m*(J-SA)*228.3 mg/g (GACOLaO1273), 176.1mg/g (GAC383), 138.2 mg/g (GACO383).

2.4. Langmuir Isotherm Equation

Langmuir Isotherm assumes a monolayer adsorption onto a surface containing a finite number of adsorption sites of uniform strategies of adsorption with no transmigration of adsorbate in the plane of surface[2]. The linear form of Langmuir Isotherm is given by the following equation.

$$\frac{C_e}{q_e} = \frac{1}{K_L} + \frac{a_L}{K_L} C_e \qquad (5)$$

Where $C_e$is the equilibrium concentration (mg/L),q_e is the amount of adsorbate adsorbed at equilibrium(mg/g), $K_L$and a_L are Langmuir constants which are related to the energy of adsorption, K_L/a_L =b , is the monolayer adsorption capacity. When C_e/q_e was plotted against C_e, straight line with slope $a_L/K_L$and intercept $1/K_L$was obtained and theconstantsa_L and $K_L$were calculated from theisotherm plotted (Fig.4) and their values are given in Table I.

Langmuir isotherm shows a best fit among the isotherms used and theLangmuir isotherm parameters of the prepared carbons, GACOLaO1273, GAC383and GACO383 (Table 1). Among the series, GACOLaO1273 has the highest monolayer capacity *b* value of 229.4 mg/g followed by GAC383 (178.6mg/g) and GACO383 (131.8 mg/g). Langmuir isotherm fits best based on the regression analysis as the isotherm plot shows a higher regression of R^2 = 0.99.

2.5. Freundlich IsothermEquation

The well-known linear logarithmic form of Freundlich model used to study adsorption isotherm behavior from liquid phase is given by

$$\log q_e = \log K_F + \frac{1}{n}\log C_e \quad (5)$$

Freundlich models assumes heterogeneous surface energies. $C_e$is the equilibrium concentration (mg/L),q_e is the amount of adsorbate adsorbed at equilibrium(mg/g), n is the Freundlich constant related to the intensity of adsorption and whose value greater than 1 shows the favorability of the adsorption process and K_F(mg/g) is the adsorption capacity of the adsorbent[20]. The slope $^{1}/_{n}$ ranging between 0 and 1, is a measure of adsorption intensity or surface heterogeneity, becoming more heterogeneous as its value gets closer to zero[21].

The plot of *log* q_e *Vs log* C_e gives a straight line with slope $^{1}/_{n}$ (Fig.5) and intercept *log* K_F. The Freundlich isotherm parameter are given in Table 1.The Freundlich constant K_F is higher for GACOLaO1273 (K_F=58.5 L/g) confirms the higher adsorption capacity for MB dye than that of GAC383 (K_F=45.0L/g) and GACO383 (K_F=39.6L/g).The value of n is greater than 1 confirms the favorability of adsorption[22].

2.6. Dubinin-Radushkevich Isotherm Equation

To calculate the micro porevolume,Dubinin- Radushkevichmodel was used. Dubinin-Radushkevichlinear form can be applied on both homogenous and heterogeneous surfaces[23].

$$\ln q_e = \ln q_s - \beta\varepsilon^2 \quad (4)$$

Where q_e is the amount adsorbed at equilibrium (mg/g), q_s is the micro porevolume, andβ is a constant related to mean free energy of adsorption mol^2/KJ^2.

$$\varepsilon = [RT\ln(1+1/C_e)] \quad (5)$$

Where R is the universal gas constant J/mol/K, T is the absolute temperature (K).The plot lnq_e *Vs* $\mathcal{E}^2$ gives a straight line, which helps us to determine the q_s and β from the intercept and slope respectively. The D-R plot is given in Fig. 6(a-c), the micro pore volume from the D-R plot is obtained by linear fitting the lowest values of the isotherm plot. The intercept of the plot gives the micro pore volume (q_m*D-R)*.D-R micro pore volume of GACOLaO1273K $q_{m(}$*D-R* was obtained as 93.5 mg/g and micro pore surface area of 211.3 m^2/g which is higher than GAC383 (136.3 m^2/g) and GACO383(131.1 m^2/g) .

2. 7 Isotherm Model Analysis

John-Sivanandan Achari isotherm plot analysis, constants and parameters are given in Table (1). Reveals that, among the series, GACOLaO1273 has the highest monolayer capacity q_m

(J-SA) value of 228.3 mg/g (with specific surface area, SSA of 515.9 m^2/g). This carbon has plot with three distinct phases with slope *n* absorbability constants with n_1(0.21), n_2 (0.71) & n_3 (0.36). Followed by GAC383 has q_m 176.1mg/g (SSA of 397.9 m^2/g) with n_1 (0.39). Carbon GACO383 has two distinct phases with q_m 138.2 mg/g (SSA of 312.3 m^2/g) with n_1(0.49), n_2 (0.41) . It is seen that basic carbon GAC383 has a single phase (line plot without kink). GACO383 has a two phases with two lines in the graph with a kink in the J- SA plots. This confirms the microporous behavior with one type of homogenous porous structure with universal Type I character as per IUPAC (2015) guidelines for the basic carbon GAC383. Dr. P. T. John & V. S. Achari (2002)7 classified this type of porous materials are with monodisperse pores. There arises a question why the carbon GACO383 has a less *qm* and SSA regards to GAC383. We know that, GACO383 is an oxidized prodigy of GAC383 using HNO_3. This modification could widen the existing inherent micropores and leads to loss of porosity. Hence, monolayer capacity q_m is substantially reduced. This recorded a lower surface area. But both John-Sivanandan Achari & Langmuir isotherm fits best based on the regression analysis. Both isotherm plots show a higher regression of R^2 = 0.99, for the materials. This reveals that the homogeneity of the pores are retained even after the surface chemical treatment. This observation is further supported by the Dubinin- Radushkevich (D-R) model analysis. It is seen that in D-R plots, the three carbons have retained the microporosity with straight line plots. GAC383 with qm (D-*R*) 60.3 mg/g has micropore specific surface area (mSSA;136.3 m^2/g) and GACO383 qm (D-*R*) 58.0 mg/g (mSSA; 131.1 m^2/g) . Surface oxidation altered the dimension of micropores into width widening subsequently for a noticed reduction of micropore uptake capacity. As regards to GACOLaO1273K, q_m*(D-R)* obtained is 93.5 mg/g with a micro pore surface area, mSAA of 211.3 m^2/g. Here, the thermo chemical activation after doping with LaO at 1273 K, nearly double the micropore quantity adsorbed. Straight line plots indicate that the homogeneity of pores existed is retained during activation. New activation strategy generated more micropores on the native carbon surface.

John-Sivanandan Achari analysis of the plots of GACOLaO1273K gives very significant features. Plots are marked by three phases of adsorption separated by distinct kinks with definite slope (n) values. Each phase is controlled by a separate adsorption mechanism as the uptake occurs only in one type of pores restricted by pore geometry. These stages are finer pore filling/ uptake, micropore filling (uptake), monolayer coverage (adsorption). Each stages, the intensity of adsorption is decided by the dimension and availability of selective pores decided by their relative proportions. However, the monolayer adsorption is obtained at

the point of saturation in the case of micro and mesoporous materials. LaO doping and heat treatment followed at 10000C for the GACOLaO1273K, generated more proportion of micropores with good contribution by finer and wider micropores in addition to the existing micropores. This pore generation due chemo- thermal treatment is well reflected in the form and shape of John-Sivanandan Achari isotherm plots. The model evaluated GACOLaO1273 that treatment sufficiently tuned the material enough to attain a highest monolayer capacity *qm* (J-SA) 228.3 mg/g with SSA of 515.9

3. Conclusions

The adsorption parameters of the newly prepared carbon were evaluated by applying John-Sivanandan Achari Isotherm Equation and other standard adsorption isotherms. The monolayer capacity obtained from John-Sivanandan Achari Isotherm Equation was used to calculate the specific surface area of the adsorbent, which was very much comparable with Langmuir monolayer capacity and Surface area. The high porosity developed for the Carbon prepared by the chemical activation with La_2O_3 followed by the thermal activation at 1273K,increased the thermal degradation and volatilization process which leads to the development of pores with increase in surface area. These findings are a step forward to establish that, LaO activation at 1000^{o}C can insitu generate more micropores on the surface of a basic carbon through a set of proper surface tuning procedures. Porous materials with any type of porous structure can be texturally characterized by John & John-Sivanandan Achari Isotherm model methods.

Figures

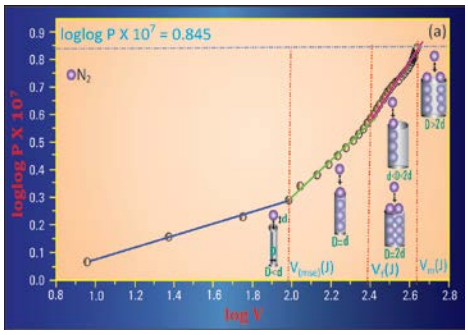

Fig 1: John isotherm plot for N_2 at 77K on micro porous carbon GC using equation *log log P = C +n log V).* Phases of adsorption are distinct with kink and slope (n) to identify process of pore filling.

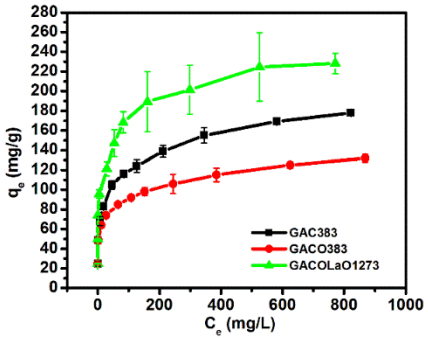

Fig 2 : General Isotherm of GAC383, GACO383 and GACOLaO1273

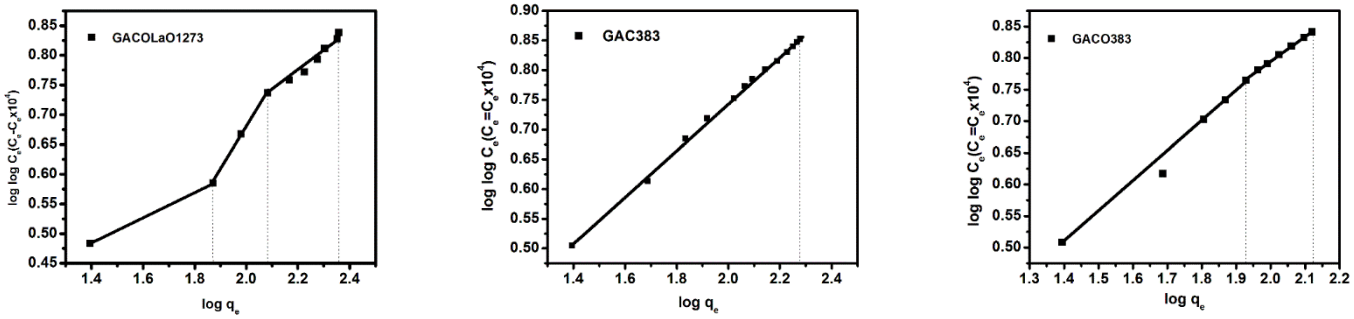

Fig. 3 : John- Sivanandan Achari isotherm of GACOLaO1273, GAC383, GACO383

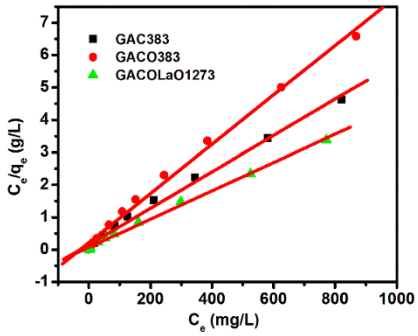

Fig 4 : Langmuir Isotherm of GAC383, GACO383, and GACOLaO1273

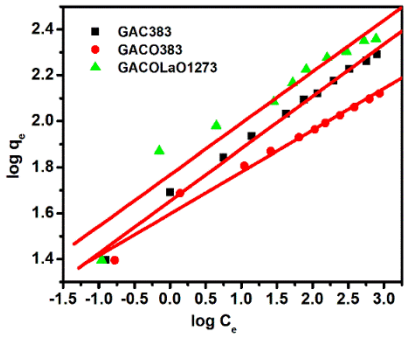

Fig 5 : Freundlich Isotherm of GAC383, GACO383 and GACOLaO1273

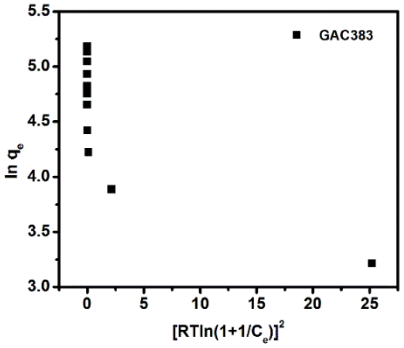

Fig. 6(a): Dubinin-Radushkevich isotherm plot for the adsorption of methylene blue onto carbon GAC383 at 303K. (C_0=25-1000mg/L, dosage=1g/L, equilibration period-10h)

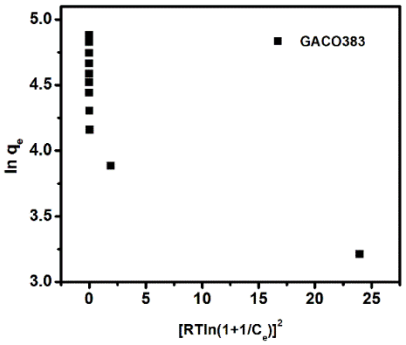

Fig. 6(b): Dubinin-Radushkevich isotherm plot for the adsorption of methylene blue onto carbon GACO383 at 303K. (C_0=25-1000mg/L, dosage=1g/L, equilibration period-10h)

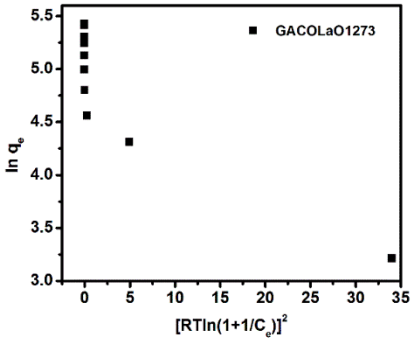

Fig.6(c): Dubinin-Radushkevich isotherm plot for the adsorption of methylene blue onto carbon GACOLaO1273 at 303K. (C_0=25-1000mg/L, dosage=1g/L, equilibration period-10h)

Table:

Table 1. John- Sivanandan Achari (J-SA) isotherm parameters, monolayer adsorptionq_m*(J-SA)*and specific surface area *(SA)* of the granular activated carbons studied along with Langmuir Isotherm, Freundlich and Dubinin- Radushkevich (D-R) isotherm constants.

Carbon samples	**Langmuir Isotherm**				**Freundlich isotherm**			**Dubinin-Radushkevich (D-R) isotherm**		**John–Sivanandan Achari Isotherm (J-SA)**	
	b (mg/g)	K_L (L/g)	SA (m^2/g)	R^2	K_F (L/g)	1/n	R^2	q_m*(D-R)* (mg/g)	SA_{micro} (m^2/g)	q_m*(J-SA)* (mg/g)	SA (m^2/g)
GAC383	178.6	6.24	403.6	0.999	45.0	0.227	0.992	60.3	136.3	176.1	397.9
GACO383	131.8	4.57	297.8	0.993	39.6	0.181	0.980	58.0	131.1	138.2	312.3
GACOLaO1273	229.4	13.6	518.4	0.996	58.5	0.224	0.931	93.5	211.3	228.3	515.9

Acknowledgement

The first author is thankful to University Grant Commission and Cochin University of Science and Technology, Kochi-22 for the financial assistance in the form of Research Fellowship and thecorresponding author is thankful to University Grants Commission (UGC), Government of India, New Delhi for the financial support by awarding the project UGC – SAP- DRS Phase II as per the order No: F4 -14/2015/DRS-II (SAP-II) Dated 19/12/2015.

References

1. V Sivanandan Achari,.; R M Lopez ; S. Jayasree,; A. S. Rajalakshmi,; O. M. Shibin,; D John,.; V Sekkar,. *Sep. Purif. Technol.*, *279* (September), 119626, 2021.
2. I Langmuir,.. *J. Am. Chem. Soc.*, *40* (9), 1361, 1918.
3. S. Brunauer,.; P. H Emmett,.; E Teller,. *J. Am. Chem. Soc. 60* (1), 309, 1938.
4. J. H. De boer, and B. Lippens, *J. Catal.*, *4* (3), 319, 1965.
5. M. M. Dubinin,. *Carbon N. Y.*, *23* (4), 373, 1985.
6. P.T.John, D.K.Suri, K. C. N. *J. Mater. Sci.*, *20*, 2071, 1985.
7. P. T. John,; V. S. Achari,. *J. Mater. Sci.*, *37* (4), 885, 2002.
8. V. S. Achari,; R. M. Lopez,; S. Jayasree,; A. S. Rajalakshmi, *Int. J. Chem. Kinet. 51*,

215, 2019.

9. V. S. Achari,; R. M. Lopez,; S. Jayasree,; A. S. Rajalakshmi, B. Ravindran,; V. Sekkar,. *J. Environ. Chem. Eng.*, 103670, 2020.
10. P. J. Pomonis, *Catal. Commun.*, *6*, 93, 2005.
11. V. S. Achari; M. Thomas,; S. Jayasree,; A. S. Rajalakshmi,; R. M. Lopez,; B. Ravindran, *Indian J. Chem. Technol.*, *25* (March), 123, 2018.
12. (B. Ravindran, Adsorption Isotherm Studies on Activated Carbon Prepared by Activation with Cerium Compounds, Cochin University of Science and Technology,Ph.D.thesisPh.D.Thesis 2016.
13. S Jayasree, Granular Activated Carbon Incorporated with Zn2+/Nano ZnO: Study of Adsorption Isotherms, Porosity, Kinetics and Thermodynamics, Cochin University of Science and Technology, Ph.D.Thesis2017.
14. V. S. Achari; S. Jayasree ; A. S. Rajalakshmi. Adsorption of p – Nitrophenol on Coconut Shell Granular Activated Carbon : Isotherms , Kinetics and Thermodynamics. *Indian Journal of Chemical Technology 24* (September), 471, 2017
15. A. S. Rajalakshmi, Adsorption Isotherm Studies of Granular Activated Carbons: Activation with Zr4+/Nano ZrO2, Porosity, Surface Area, Kinetics and Thermodynamics, Cochin University of Science and Technology, Ph.D.thesis2017.
16. J. C. Santamarina,; K. A. Klein,; Y. H. Wang,; E. Prencke,*Can.Geotech.J.*, *241*, 233, 2002.
17. S. Karago, Activated Carbons from Waste Biomass by Sulfuric Acid Activation and Their Use on Methylene Blue Adsorption. *Bioresour. Technol.*, *99*, 6214–6222, 2008.
18. M. Thomas, Adsorption Isotherm Characterisation of Porous Materials Using John Isotherm, Cochin University of Science and Technology, Ph.D.thesis,2016.
19. M. Thommes,; K. Kaneko,; A. V. Neimark,; J. P Olivier,.; F.Rodriguez-Reinoso,; Rouquerol, J.; K. S. W.Sing,. *Pure Appl. Chem. 87* (9–10), 1051 2015.
20. H. M. F. Freundlich, Over the Adsorption in Solution. *J. Phys. Chem.*, *57*, 385, 1906.
21. M. Jung,; K. Ahn,; Y. Lee,; K. Kim,; J. Rhee,; J. Tae,; K. Paeng, *Microchem. J.*, *70*, 123, 2001.
22. P. A. M. Mourao,; C. Laginhas,; F. Custodio,; J. M. V. Nabais,; P. J. M. Carrott,; M. M. L. R. Carrott, *Fuel Process. Technol. 92* (2), 241, 2011.
23. B. H.Hameed, A. A. Rahman,. J. Hazard. Mater., *160* (2–3), 576, 2008.

Recent Bio-medical applications of iron oxide magnetic nanoparticles

M. A. Bora

Department of Chemistry, BJS'S ASC College (Affiliated to S.P. Pune University), Wagholi, Pune, Maharashtra, India-412207

Email: bmanishabora@gmail.com

Received: 18.4.23, Revised: 24.4.23, 27.4.23 Accepted: 27.4.23

Abstract

In recent times, pronounced consideration has been dedicated to the amalgamation of several magnetic nanoparticles because of their widespread smart and encouraging biological solicitations. The magnetic IONPs, magnetite (Fe_3O_4), and maghemite (γ-Fe_2O_3) have shown some remarkable applications in nanomedicines, diagnosis tools, and pharmaceuticals. Iron oxide magnetic nanoparticles (IOMNPs) have been explored for an extensive collection of biomedical and healthcare solicitations built on their surface properties, biocompatibility, and exceptionally, great magnetic susceptibility. In this logic, the magnetic properties of IOMNPs permit their usage in numerous biomedical applications, such as targeted drug delivery, hyperthermia, magnetic tissue engineering, MRI contrast agents, in vitro magnetic bio-separation, bio-analysis, magnetic transducers, and theranostic platforms. The functionalized hybrid IOMNPs have also been utilized against fungal infections and numerous pathogenic strains of microorganisms. Iron oxides play a significant role in the field of bio-catalysis, nanotechnology, and bio-medicines; therefore they are the main focus of this review. Keeping in mind the state-of-the-art, this review is intended to report the latest information about IOMNPs from methods of synthesis to modern bio-medical applications. Moreover, in-vivo and in-vitro uses of IOMNPs have conversed in detail. The challenges and restrictions in the biological usage of IOMNPs are also highlighted. This review based on IOMNPs will deliver a convincing vision for the investigators in nano-biotechnology and pharmacy.

Keywords**:** *Magnetic, Bio-medical, Iron oxide, Hyperthermia, Drug delivery*

1. Introduction

Nanomaterials are at the forefront of speedy progress in nanotechnology. They have fascinated extensive devotion as these nanomaterials display rare possessions when related to bulk substance[1-3]. The physicochemical properties of nanomaterials are much reliant on their dimensions, shape, structure, morphology, and crystallinity. Metallic nanoparticles possess unusual thermal, chemical, optical, and physical properties[4-8]. Iron oxide magnetic nanoparticles (IOMNPs) like magnetite and maghematite have been extensively studied for their commercial applications in nano bio-medicines and diagnosis. Ferro-fluid usages in blended magnetic nano-biosensors and as intermediaries of heat in hyperthermia have been testified. Developments in the construction of magnetic nanoparticles have managed their innovative usages in cell tracking, cell separation, bio sensors, enzyme immobilization, hyperthermia treatment, immunology, drug delivery vehicles (Ferrofluids), diagnosis, etc. For these applications, the perfect IOMNPs should display a trivial size (<100 nm), splendid magnetism with negligible polydispersity, safe, biodegradable eco-friendly surface crust, and extraordinary magnetization properties[9-13]. IOMNPs are most popular in biomedical applications due to their low cost, less toxicity, and their unique magnetic properties. Magnetite and maghematite usually show super magnetic properties when possessing a size of less than 20 nm and are utilized for various biomedical applications. Mandarano et.al.[14] reported applications of SPIONPs as contrast agents in MRI and their potential applications to a range of pathologies and processes involving MRI. Kayal et.al.[15] reported applications of versatile IONPs for drug release and drug delivery. Chen et.al.[16] reported that functional magnetite-TiO_2 core-shell NPs act as killing mediators for pathogenic bacteria in presence of light. Zhang et.al.[17] reported applications of modified magnetic NPs for MRI of surgically induced endometriosis models in rats. Lee et.al.[18] summarized the recent advances in the design and fabrications of core shells and hetero-structured SPIONPs and progress in their applications for diagnosis and biophotonics. Nithya and coworkers[19] explained the in-vitro biological activity of iron oxide nanocomposites. Rani et.al.[20] reported Fe_3O_4/RGO for the extremely sensitive and selective sensing of dopamine. Gamarra et.al.[21] reported applications of hyperthermia induced by SPIONPs in glioma treatments. Wang et.al.[22] studied magnetic SiO_2 NPs for magnetically attributed suicide gene remedy of carcinoma of liver cells. Mahmoudi and coworkers[23] have reviewed the applications of super magnetic iron oxide nanoparticles in chemotherapy. Biocompatible SPIONPs with proper surface coating and in conjugation with proteins have fascinated abundant devotion for drug delivery uses. Kievit et.al.[24] reported the applications of surface -modified SPIONPs for targeted cancer chemotherapy. Ciobanu et.al.[25] has reported biomedical applications of IONPs@dextron thin films obtained by the maple technique

created by the co-precipitation technique. Dhanish et.al.[26] justified applications of magnetite nanoparticles for targeted drug delivery. IOMNPs play a noteworthy part in the arena of pharmacy and bio-medicines; therefore they are the main focus of this review. Keeping in mind the state-of-the-art, this review is proposed to report the latest facts about IOMNPs. Moreover, in-vivo and in-vitro uses of IOMNPs have been communicated in detail. The challenges and restrictions in the biological usage of IOMNPs are also highlighted. This review based on IOMNPs will deliver a convincing vision for the investigators in nano-biotechnology and pharmacy.

2. Synthesis Methods and Surface Modifications

2.1 Synthesis methods of IOMNPs

In the preceding decade, improved surveys with several types of iron oxides have been carried out in the arena of IOMNPs which typically comprises the magnetite (Fe_3O4), hematite (α-Fe_2O_3), maghemite (γ-Fe_2O_3), wüstite (FeO), ε-Fe_2O_3, β-Fe_2O_3. Consequently, iron oxide is found in numerous forms (Fig.1.) which might be magnetic or non-magnetic in nature[27-30].

For the production and surface management of IO nanoparticles primarily two methodologies viz., a top-down and bottom-up approach is expansively studied (Fig.2.). The bulk ingredients are sliced down by physical or chemical methods in top-down tactic till they attain desired size. The top-down approach results defects in surface structure, damages in the crystal structure as well stresses because of the harsh and severe reaction conditions used during synthesis of nano materials. It leads into the alterations in the morphological and surface properties of nanomaterials. The bottom up method is largely applied for the synthesis of materials having nanometer/micrometer size the fabrication as well as method. Further this method has wide applications and significance in the synthesis of nanomaterials as it possesses a homogeneous chemical composition[31-40]. A number of methods have been implemented for the synthesis of IOMNPs, namely, microemulsion, electro-chemical, hydrothermal/solvo-thermal, sol-gel, ultrasonic, and co-precipitation, etc. Among these, co-precipitation is the utmost general and exploited process (Fig.3.) for the synthesis of magnetic iron oxide nanoparticles[41-45]. These approaches have the capacity to make IOMNPs by adjusting reaction settings. Magnetite (Fe_3O_4) and maghematite (γ-Fe_2O_3) are magnetic iron oxides which are found to have extraordinary bio medical applications. Magnetite has positively charged Fe ions occupying tetrahedral and octahedral situates of a cubic inverse spinel assembly. Maghematite has an inverse spinel structure like Fe_3O_4 however has an imperfect lattice structure. Pure magnetite is typically black while maghemite is brown in colour[46]. Several man-made green paths have been established in order to attain suitable control of size, polydispersity, shape, morphology and the magnetic nature of IOMNPs. A number of synthesis methods to attain nature, type, shape, size, dispersity,

crystallinity and magnetic performance of IOMNPs have been established. Each synthetic approach has its own benefits and difficulties. Even though physical dry approaches are stress-free, monitoring the nano size is a challenging task. Although in a wet approach, nano size can be fairly organized by altering the synthetic conditions. The chemical synthesis approaches include electrochemical, hydrothermal, chemical coprecipitation, sol-gel, sonochemical decomposition, supercritical fluid method, flow injection, and nonreactors. The chemical approaches are typically accepted also due to small fabrication cost and greater yields[27]. A common reaction sequence which occurs during IOMNP synthesis is as follows,

$$Fe^{3+} + 3OH^- \longrightarrow Fe(OH)_3\ (s) \quad \text{---------- (1)}$$

$$Fe(OH)_3\ (s) \longrightarrow FeOOH\ (s) + H_2O \quad \text{----------(2)}$$

$$Fe^{2+} + 2OH^- \longrightarrow Fe(OH)_2\ (s) \quad \text{----------(3)}$$

$$2FeOOH\ (s) + Fe(OH)_2\ (s) \longrightarrow Fe_3O_4\ (s) + 2H_2O \quad \text{-------(4)}$$

$$2FeOOH \longrightarrow \text{alpha } Fe_2O_3 + H_2O \quad \text{-------(5)}$$

In general, magnetite (Fe_3O_4) nanoparticles are prepared by addition of an alkali to a mixture of Fe^{2+} and Fe^{3+} salts at 1:2 molar ratios, ensuing in a black nanomaterial. The general reaction may be written as follows:

$$Fe^{2+} + 2Fe^{3+} + 8\,OH^- \longrightarrow Fe_3O_4 + 4H_2O \quad \text{---------- (6)}$$

Magnetite, is a mixture of Fe_2O_3 and FeO, is unstable and can easily suffer from oxidation i.e. conversion of Fe^{2+}into $Fe^{3+}$to form maghemite in the presence of air, moisture and light[12-13].

$$\underset{\text{Magnetite}}{Fe_3O_4} + 2H^+ \xrightarrow{(O_2)} \underset{\text{Maghemate}}{\text{Gamma } Fe_2O_3} + Fe^{2+} + H_2O \quad \text{---------- (7)}$$

The phase changeover of γ-Fe_2O_3 into α-Fe_2O_3 occurs during calcination at about 400-500°C. Manipulation of synthesis factors is essential to achieve controlled nanoparticles with respect to particle size, shape, morphology, purity, agglomeration and crystallinity.

A nanomaterial synthesis path must assist control over various reaction constraints such as temperature, concentration, pH, speed of stirring, particle size distribution, shape control, configuration and composition, which comprises crystallinity, purity, quick assay and various other modifications[28].

The biological application of IOMNPs is regarded by the practice of coating particle surface with diverse coating materials. IOMNPs can be encapsulated with various biomaterials like nucleotides, proteins, antibodies, drugs, surfactants etc. for their biological applications.[29-32]

2.2 Surface modification of IOMNPs

Recently, widespread research has been committed to the capping and functionalization of IOMNPs. The exterior alterations are found to be crucial features for improved control of particle morphology and shape, as well as to yield mono-dispersed IOMNPs, having a straight impact on their various properties and solicitations. The biocompatibility and toxicity of IOMNPs are the most vital measures to be considered for their biomedical applications. The IOMNPs must have extraordinary magnetization as their movement in the blood can be controlled with an exterior magnetic field till it is halted near the directed tissue[33-36]. The IOMNPs with an extensive biodegradability blood retention period and stumpy toxicity have arisen as the basic criteria aimed at in-vivo and in-vitro biomedical applications. Selected biological applications necessitate superficial capping, particularly core-shell type IOMNPs. There are four important reasons for the surface modification of IOMNPs; they are as follows:

for improving the dispersion of NPs, to enhance the surface activity, in order to boost the physicochemical and mechanical properties, and to increase the biocompatibility.

3. Biomedical solicitations of IOMNPs

3.1 In-vivo biomedical solicitations

3.1.1 Targeted Drug Delivery

Thermotherapy/Hyperthermia is the most encouraging biological solicitation of IOMNPs in sarcoma chemotherapy. Targeted drug delivery states the magnetically aided delivery at the location of concern. In this technique, magnetic nanoparticles are persuaded into the body by injection. Then, IOMNPs are exposed to an outer magnetic meadow produced by induction coils to create heat in the body. The induction coils produce distress on IOMNPs and the resulting electromagnetic energy is carried to the neighboring cells in the form of heat, which raise the temperature of cancer cells by about $2-3℃$. In order to improve or increase the heating efficiency of IOMNPs, they may be directly injected to targeted tumor cells. Typically, it is expected that the surface belongings of IOMNPs are most significant than the core properties, owing to the straight association of surface materials with the biotic surroundings. Henceforth, it's crucial to maintain the IOMNPs surface coating with biocompatible constituents. Functionalized IOMNPs as an exporter can deliver a varied array of drugs to most of the body parts. In a drug hauler scheme, the dimensions, surface assets, and firmness are the vital topographies. Not only cancer diagnosis, but diverse types of IOMNPs have been established for new biomedical

applications, such as the revealing of brain swelling or the premature identification of thrombosis etc. Furthermore, targeted drug delivery of drugs to the brain has massive prospective for the treatment of quite a few neural ailments like Alzheimer's syndrome and brain cancers[37-40.]

3.1.2 Magnetic Resonance Imaging (MRI)

Magnetic Resonance Imaging is an influential nonionizing method that delivers body structural pictures with great perseverance and without depth restraint in the entity. IOMNPs have been established as a clever alternative to conservative contrast agents (CAs) for MRI. Within body cells finding or labeling by MRI can offer the scrutiny of biotic practices and display cell remedy directly, which is an additional prevalent solicitation of IOMNPs in MRI. Magnetic Particle Imaging is a comparatively fresh tracker imaging technique that hires IOMNPs and received substantial awareness from medical investigators. MRI is one of the leading in-vivo imaging modalities, besides Positron Emission Tomography (PET), Computed Tomography (CT), and ultrasound imaging. In order to perform as a contrast agent, IOMNP must be covered with polar coating agents. These coatings must be hydrophilic, comprising small polar groups, polymer, protein, etc. to disperse in an aqueous solution. Moreover, the simplicity of surface functionalization with diverse kinds of ligands unlocks the prospect of bringing out MRI. Multicomponent iron oxide nanoparticles offer novel prospects for MRI diagnosis, as well as combined therapies[41-44.]

3.1.3 Antimicrobial and Fungicidal Activity

Ferro-fluids are the emulsions or sols of IOMNPs in aqueous or non-aqueous solutions that display robust magnetic characteristics. Moreover, ferro-fluids have demonstrated as active agents against microbial and fungal infections. They are active against Staphylococcus species, E. coli, Xanthomonas, and Proteus vulgaris. Magnetite/silver nanocomposite ferro-fluids coated with oleic acid have too displayed antibacterial bustle against Bacillus subtilis, Staphylococcus aureus, and pathogenic C. albicans. Moreover, ferro-fluids have been operative in diminishing the advancement of fibroid-associated soreness. IOMNPs are believed to constrain the development of microorganisms by generating oxidative stress and responsive oxygen species that restrict the production of amino acids, triglyceride peroxidation, and DNA duplication. It also alters the corpuscle plasma membrane penetrability and creates irreversible destruction[45-50].

3.2 Ex-vivo biomedical solicitations

The surface modified IOMNPs have tremendous demand for developing novel investigative products. Some of the innovative in vitro applications are discussed below,

3.2.1 Theranostic systems

The term “theranostic” means a substance that syndicates the methods of remedy and diagnostic imaging. Magnetite IONPs are possibly the most exploited forum for theranostic schemes. The foremost advantages of biocompatible stabilized IOMNPs are, extraordinary drug stuffing as per their physico-chemical characteristics, capacity of magnetic control through mutual stimuli-sensitive and careful generates, adaptive pharmacokinetics, bio distribution, with boosted half-life, and opportunity to custom the particles for regulating targeted drug deliveries and the various therapeutic responses.

3.2.2 Enzyme Immobilization

In bio-catalytic methods, the parting of immobilized enzymes from the reaction muddle is biggest challenge that must overcome. In order to solve this challenge, linking bio-molecules with IOMNPs offers a simplistic split-up of the bio-catalyst with the help of an exterior applied magnetic field. Recently, IOMNPs have attracted an excessive courtesy as hopeful support transporters in enzymes arrest due to the enormous outer surface domain. The presence of polar hydrophilic groups on the surface permits their stress-free capping and powerful binding of the enzyme. For enzymatic cripple, IOMNPs are frequently altered with polymeric materials like peptides, chitosan, PAA, polyethylene imine and poly-dopamine owing their remarkable bio-degradability and bio-compatibility characteristics[30-43.]

3.2.3 Bio-separation

Bio-separation is another vital type of ex-vivo applications of IOMNPs which involves separation of antibodies, tissue, DNA, RNA, enzymes, genetic material and, micro-organisms, etc. For getting enhanced separation, the surface-altered IOMNPs with suitable materials are generally cast-off. To host various functional assemblies (e.g., −COOH, $-NH_2$, −OH and −SH) over the surface a number of ligands, polymeric materials and surfactants are used through careful surface assimilations. Furthermore, the greater aspect ratios, adsorption characteristics, chemical arrangements, stumpy toxicity, surface structures, stability, magnetic properties, size and its dissemination are extremely vital in the IOMNPs established magnetic bio-separation[35-45.]

3.2.4 Bio-sensors

Bio-sensing is a current manifesto for the identifying microorganisms, bio-molecules, tissues, genetic materials, etc. with focused thoughtfulness for early detecting premature ailments. Bio-sensors are diagnostic strategies exploited in the medical field. Their chief purpose is altering bio-chemical response into electrical signals. Furthermore, IOMNPs functionalized with appropriate capping agents are advantageous for detecting targeted bio-molecular connections[35-44.]

3.2.5 Rapid detection of bacteria

Lateral flow immunoassay (LFA) bands, demonstrate the combination of the benefits of nanomaterials and chromatographic separation and have turned out to be a quick, economical, and accessible point-of-care testing tool (POCT) for numerous bio-analysis uses. In recent times, certain new signal labels, with quantum dots, magnetic nanoparticles (MNPs), and surface-enhanced Raman scattering nano-tags, were used in LFA bands as an alternative to the usually used colloidal gold to create a stronger and legible signal for the assessable recognition of targets. C. Wang et. al. [45a] reported the application of magnetic quantum dots PEI-mediated electrostatic adsorption technique for the selective and rapid detection of bacteria.

3.2.6 Biodegradable Micro-robots for drug delivery

Molecularly targeted treatment has been projected to elucidate the struggle of lack of specificity in existing chemotherapy treatments. Micro-robots have been newly anticipated and aggressively investigated as a means to overawe the restrictions of the drug treatments. Mostly, micro-robots comprise an anti-cancer medicine and IO magnetic nanoparticles for their electromagnetic actuation. The newly projected micro-robots contain a gelatin-based hydrogel, IOMNPs, and modified poly lactic-co-glycolic acid (PLGA) particles. The biodegradable hydrogel micro-robot reaches a pre-determined target abrasion and thereafter, the gelatin hydrogel micro-robot is decomposed. The IOMNPs and PLGA drug particles are left in the target area and then lastly, the anti-cancer medication can be released to generate a therapeutic effect in the target lesion[45b].

Following are few recent ex-vivo and in-vivo bio-medical solicitations of IOMNPs,

3.3 Challenges in Bio-medical applications of IOMNPs

IOMNPs are extensively cast-off biocompatible nanomaterials to improve plentiful biomedical solicitations. Nevertheless, undecorated IOMNPs have revealed inadequate claims due to columbic forces that upturn the accumulation, causing in increased size. Consequently, altering the surface charge and design of IOMNPs are of considerable concern when thinking about their claims in remarkably established biomedical technologies[52-56]. Another limitation of IOMNPs is their aqua-phobic non-polar surface which makes them suitable only to be solvable only in non-polar solvents, like n-hexane, toluene, etc. The exterior surface of IOMNPs needs to be transformed into a polar, hydrophilic surface to overawe this limitation. Surface functionalization also consequences a bio-compatible surface for bio-conjugation functions, but also delivers added physical properties like improved amplitude. Another important limitation of IOMNPS is their toxicity and bio-compatibility. The ex-vivo and in-vivo toxicity of IOMNPs may disclose critical evidence regarding the danger of these nanoparticles. Nevertheless, the toxicity of IOMNPs may hinge on several elements such as, physico-chemical properties like composition, particle size,

solvability, and surface chemistry, biotic accomplishments like bio-degradability, pharmaco-kinetics, and circulation in the body, drug delivery etiquette with reference to the dosage and its path.

Furthermore, when IOMNPs are employed as nano-transporters, the toxicity of the drug may be altered as a concern of an adjustment of its bio dispersal. For these motives, an in-depth assessment of the cell toxicity is hence required for each case about the planned solicitation[57-62].

4. Future Scope of IOMNPs in Biomedicines and pharmaceuticals

At present, IOMNPs have been productively applied in bio-medicines and diagnostics as a probe for revealing diseases or illnesses, drug deliveries, etc. Furthermore, with progressions, nowadays IOMNPs are set in combinations to attain multiple utilities in a solitary stage like MRI, and PET/CT imaging, etc. Recently IOMNPs based nano-hybrids were altered for hyperthermia and PTT, where even small concentrations are capable to boost the heat generation at the tumor spot and can be competently cast-off for cellular remedies. Recent advances in nano-hybrid IOMNPs synthesis paved the path to introduce enzyme mimetic, oxidase, and catalase activities. In addition, the conjugated IOMNPs made it easy finding of biomolecules in a solo step and put down the foundation to generate novel nano-sensors and nano-devices. Moreover, to overcome the obstacles in diseases like cancer and multi-drug resistant diseases, multifunctional IONPs were being designed for diagnosis, targeting, nano-carrier, chemo/ phototherapy agents. In conclusion, more progression in the novel synthesis of nanocomposites with multifunctional modalities can find better ways to use IONPs as nano-theranostic entities in biomedicine. The future of IONPs in biomedical applications holds great promise, especially in the area of disease diagnosis, early detection, cellular and deep tissue imaging, drug/gene delivery as well as multifunctional therapeutics. Custom-made medicine is also gaining courtesy and it is anticipated that the amalgamation of nanotechnology could result in predominant outcomes. In coming years, multifunctional IOMNPs would be smart materials for pharmaceutical requests and may change the typical commercial model of pharmaceutical industries[62-63]. IOMNPs physicochemical properties have to be custom-made in order to boost anti-tumor properties at a lesser magnetic field, growing the acceptability of the treatment and improving effectiveness for deep-rooted tumor growths. Desperate and productive exploration is necessary to plan and formulate IOMNPs for assorted solicitations in varied arenas in mandate to overcome challenges[64-66].

5. Conclusions

Original methods of production and solicitations of IOMNPs have been of concern in the field of nano-technology. Diverse synthetic methods have been improved, but the main challenge in the synthesis meadow that remains is the care of size and phase controlled synthesis with

reproducibility. Reusability and robustness are tough to accomplish in the prevailing synthesis approaches. The undesired reactions disturb the desired properties of the IOMNPs.

To overawe the current disputes faced with IOMNPs the subsequent particulars ought to be achieved such as , straight active and comprehensive mixing of chemical constituents, robotics and automation of processes, acceptable reaction constraints organized specifically, accurate characterization tools to categorize and approve the oxide phase of iron, knowing the perfect reaction mechanism is furthermore significant as it enables thorough consideration of the reaction so as to achieve good control over the synthesis parameters and hence control of the nanoparticle size, morphology, shape, magnetic properties, etc. Several functionalized and hybrid IOMNPs can offer wonderful opportunities in detection tools like hyperthermia, MRI, photo-thermal therapies, etc. In addition to the above state-of-the-art different arenas such as bio-medicine tools, nano-medicines, bio-catalysis, and innovative diagnostic tools etc.

Figures:

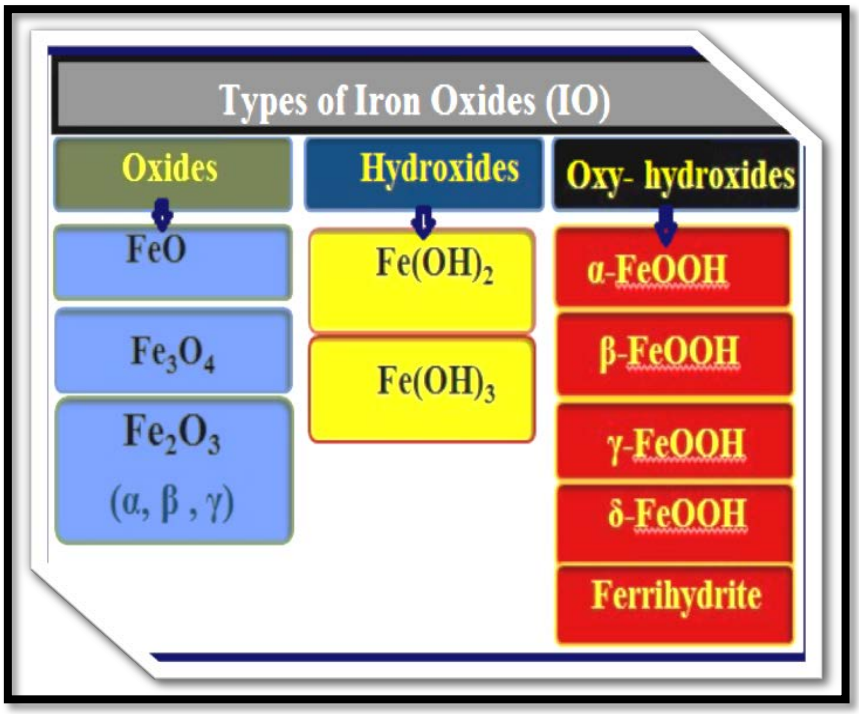

Fig.1. Types of Iron Oxides

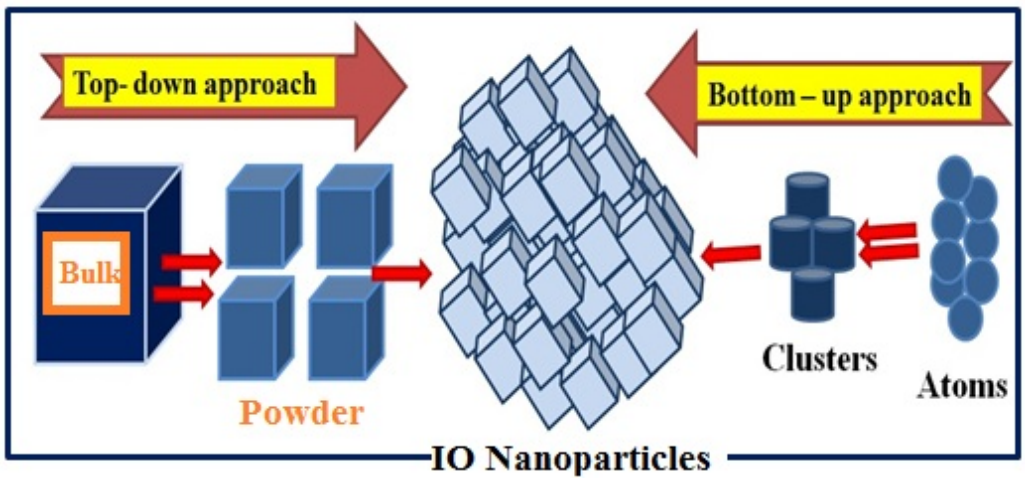

Fig.2. Top-down and bottom-up approach

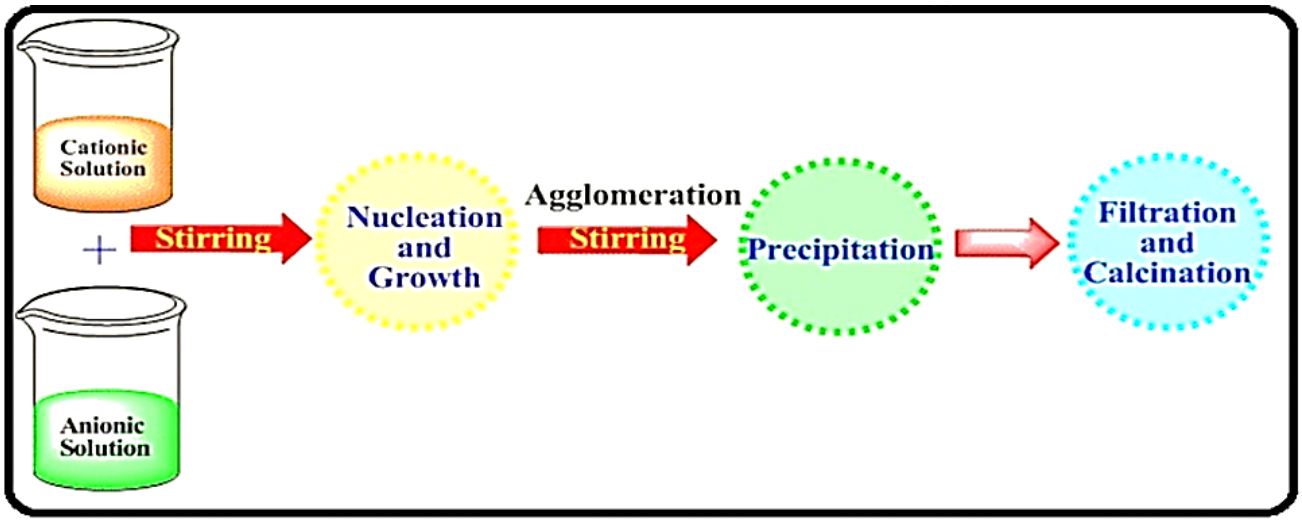

Fig.3. Co-precipitation method of synthesis

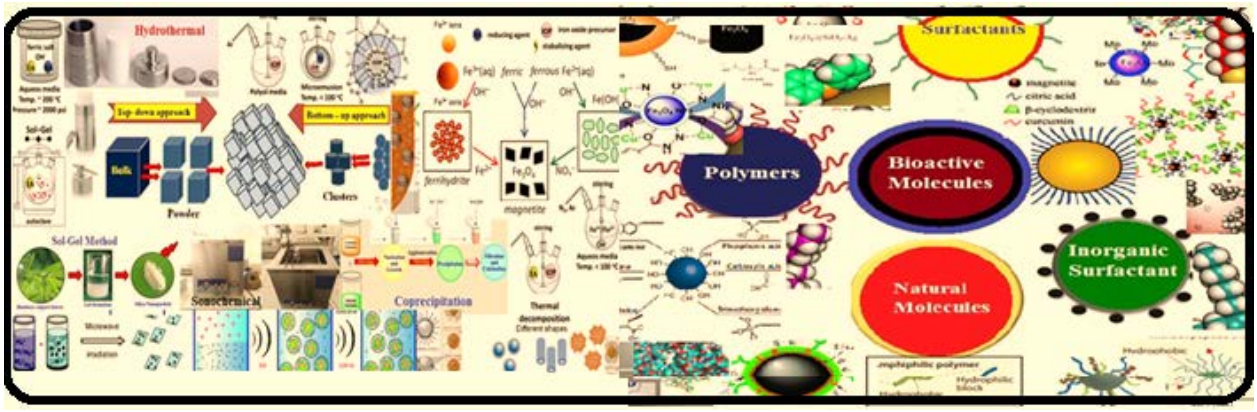

Fig.4. Common methods of synthesis and stabilization of IONPs

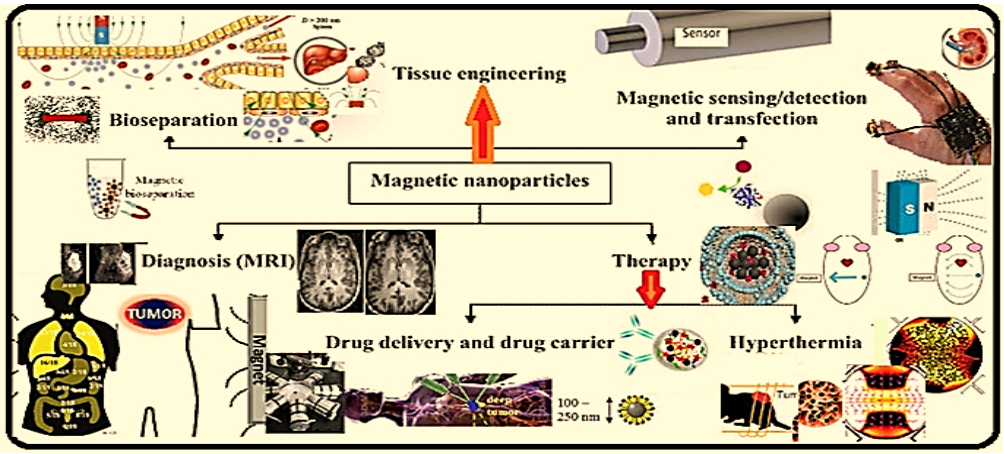

Fig.5. In-vivo and ex-vivo applications of IOMNPs

Tables:

Table1. Common methods of synthesis of IOMNPs

S. No.	Synthesis method	Temp.(°C)	Solvent	Size distribution	Shape control	Yield
1	Coprecipitation	25-90	Water	Relatively narrow	Not good	High
2	Thermal	100-350	Organic	Very narrow	Very good	High
3	Hydrothermal	200-250	Water/ Organic	Very narrow	Medium	Medium
4	Micro-emulsion	20-50	Organic	Relatively narrow	Good	Low
5	Polyol	253-300	Polyol solvents	Relatively narrow	Good	Low

Table2. Method of synthesis, functionalization and bio-medical applications of IOMNPs

S. No.	Nanoparticles	Surface Modification	Method of synthesis	Ex-vivo/ In-vivo bio-medical application	Reference
1	Fe_3O_4	Chitosan	Co-precipitation	Lipase immobilization	Liu et. al.[27]

2	IOMNPs	17β-estradiol	Molecular imprinting	Selective separation and detection of estrogen	Wang et.al.[28]
3	Magnetite	RGO	Ultrasonic	Biosensor	Lu et. al.[29]
4	Fe_3O_4	Sodium carbonate-oleic acid	Co-precipitation	Cancer therapy	Jadhav et. al.[30]
5	IOMNPs	Sodium citrate	Co-precipitation	CA/MRI of liver fibrosis	Saraswathy et. al.[31]
6	Magnetite	Polymer assembly	Co-precipitation	Dual drug delivery	Pothayee et. al.[32]
7	IOMNPs	Graphene	Co-precipitation	Bio-seperation/ Alzheimer's disease biomarkers	Demeritte et. al.[33]
8	Fe_3O_4	Polymers	Co-precipitation	Targeted drug carriers	Ulbrich et.al.[34]
9	IOMNPs	PMAA-graft-PEG copolymer	Co-precipitation	Cis-Platin delivery	Vermesh et. al.[35]
10	IOMNPs	-	Multiple approaches	Antifungal	Nazanin et.al.[36]
11	IOMNPs	Chitosan	Co-precipitation	Cancer therapy	Catalano et. al.[37]
12	Magnetite	Doxorubicin	Co-precipitation	magnetic drug targeting and tumor regression	Nigam et.al.[38]
13	Magnetite	sodium dodecyl sulphate @ oleic acid	Co-precipitation	Nano carriers for drug delivery	Dutta et.al.[39]
14	Magnetite	Fe3O4-MTX@HBc	Co-precipitation	MRI/Photo-thermal therapy	Zhang et. al.[40]
15	Maghematite	-	Sol-gel	MRI contrast enhancement	Marashdeh et.al.[41]
16	Maghematite	-	Hydrothermal	Bio-sensor	Hijiri et.al.[42]
17	IOMNPs	PEG-Arg@IONPs	Co-precipitation	MRI contrast agents	Nosrati et al.[43]
18	Magnetite	Chitosan-ampicillin	Co-precipitation	Antibacterial therapeutics	Allafchian et.al.[44]
19	IOMNPs	-	Co-precipitation	Positive contrast in MRI	Fernández et.al.[45]
20	IONPs	Various capping Agents	Multiple approaches	Cell Labeling	Nene et.al.[46]
21	IOMNPs	-	Extraction Method	Detection of SARS-CoV-2	Zhao et.al.[47]

22	Magnetite	PMAO	Thermal decomposition	Diagnosis	Vuongaf et.al.[48]
23	Magnetite	-	Bacteria mediated	Biomedicine	Rosenfeldt et.al.[49]
24	IOMNPs	Diethyl-amino ethyl-dextran	Co-precipitation	In vitro MRI	Cortés et.al.[50]
25	IOMNPs	-	Bacteria mediated	Antioxidant	Majeed et.al.[51]

References

1. S. P. Senthila, M. Kumar, P. Venkatesan, Res. J. Pharm. and Tech. 14(10), 5508, 2021.
2. J. Wallyn, N. Anton , T. F. Vandamme, Pharmaceutics.,11,601, 2019.
3. P. Jain, G. Parkhe, Research J. Pharm. and Tech., 13(11), 5562, 2020.
4. K. Praveen,K. Balamurugan, Research J. Pharm. and Tech., 13(7) 3524, 2020.
5. M. A. Dheyab, A. A. Aziz, M. S. Jameel, O. A. Noqta, B. Mehrdel, SyChin. J. Phys., 64,305, 2020.
6. P. S. Salve, Asian J. Pharm. Res. 1(4), 91, 2011.
7. S. Kumbhar, V. Salunkhe, C. Magdum, Asian J. Pharm. Res. 3(1), 40, 2013.
8. B. Kshitij, S. Makeshwar, S. R. Wasankar, Asian J. Pharm. Res. 3(1), 15, 2013.
9. V. Majethiya, S. Chandrashekhara, C. Nagesh, B. Vaghasiya, M. Sidhappara, B. Sutariya, Research J. Pharma. Dosage Forms and Tech., 4(3), 143, 2012.
10. Y. Mehta, S. Nirban, S. Kumar, K. Malodia, P. Rakha, M. Nagpal, Research J. Pharma. Dosage Forms and Tech., 3(1), 06, 2011.
11. M. Racuciu, L. Barbu-Tudoran, S. Oancea, Morosanu, C., M. Grigoras, F. Brînza, D. E. Creang, Nanomaterials, 12, 1151, 2022.
12. H. Gu, K. Xu, K. Xu, B. Xu, Chem. Commun., 20, 06, 941, 2006.
13. X. Zhang, F. Chen, Drug Delivery, 16(5), 280, 2009.
14. P. Grodzinski, M. Kircher, M. Goldberg, A. Gabizon, ACS Nano., 13, 7370, 2019.
15. R. Manchanda, A. Fernandez-Fernandez , S. L. A. Paluri, B. R. Smith Adv. Pharmacol., 91, 293, 2021.
16. W. J. Chen, P. J. Tsai, Y. C. Chen, Small, 4(4), 485, 2008.
17. H. Zhang, J. Li, W. Sun, Y. Hu, G. Zhang, M. Shen, X. Shi, PLOS ONE, 9(4), e94718, 2014.
18. H. J. Lee, J. M. Lee, Y. Chang, S. T. Woo, Magnetic Resonance Imaging, 30(6), 860, 2012.
19. G. Nithya, R. Sudha, Research J. Pharm. and Tech., 12(11), 5524, 2019.

20. G. J. Rani, K. J. Babu, G. Kumar, M. Rajan, Journal of Alloys and Compounds, 688, 500, 2016.
21. L. Gamarra, A. C. Silva, T. R. Oliveira, J. B. Mamani, S. M. Malheiros, F. Malavolta, L. Gamarra, International Journal of Nanomedicines, 591, 2011.
22. Z. Wang, Z. Chang, M. Lu, D. Shao, J. Yue, D. Yang, D.,W. Dong, Biomaterials, 154, 147, 2018.
23. M. Mahmoudi, S. Sant, B. Wang, S. Laurent, T. Sen, Advanced Drug Delivery Reviews, 63(1-2), 24, 2011.
24. F. M. Kievit, M. Zhang, Accounts of Chemical Research, 44(10), 853, 2011.
25. R. Manchanda, A. Fernandez-Fernandez, S. L. Paluri, B. R. Smith, Adv. Pharmacol. , 91, 293, 2021.
26. D. Joseph, M. Jose, Research J. Pharm. and Tech., 12(10), 4651, 2019.
27. Y.Liu, S. Jia, Q. Wu, J. Ran, W. Zhang, S. Wu, Catal. Commun., 12(8), 717, 2011.
28. S. Wang, Y. Li, M. Ding, X. Wu, J. Xu, R. Wang, J. Chromatogr. B, 879, 2595, 2011.
29. T. Lu, J. Guo, J. Dong, Z. Cui, T. Lu, C. Zhu, D. Zhang, J. Ma, J. Ultrason. Sonochem., 20, 872, 2013.
30. N. V. Jadhav, A. I. Prasad, A. Kumar, R. Mishra, S. Dhara, K. Babu, C. Prajapat, N. Misra, R. Ningthoujam, B. Pandey, Colloids Surf. B: Biointerfaces., 108,158, 2013.
31. A. Saraswathy, S. Nazeer, M. Jeevan, N. Nimi, S. Arumugam, V. S. Harikrishnan, P. H. Varma, R. S. Jayasree, Colloids Surf. B: Biointerfaces., 117, 216, 2014.
32. N. Pothayee, S. Balasubramaniam, N. Pothayee, N. Jain, N. Hu, Y. Lin, R. M. Davis, N. Sriranganathan, A. P. Koretsky, J. S. Riffle, J. Mater. Chem. B, 1, 1142, 2014.
33. T. Demeritte, B. P. Nellore, R. Kanchanapally, S. S. Sinha, A. Pramanik, S. R. Chavva, ACS Appl. Mater. Interfaces, 7, 13693, 2015.
34. K. Ulbrich, K. Hola´, V. Subr, A. Bakandritsos, J. Tuˇcek, R. Zboˇril, Chem. Rev., 116, 5338, 2016.
35. O. Vermesh, A. Aalipour, T. J. Ge, Y. Saenz, Y. Guo, I. S. Alam, S.-M. Park, C. N. Adelson, Y. Mitsutake, J. Vilches-Moure, E. Godoy, M. H. Bachmann, C. C. Ooi, J. K. Lyons, K. Mueller, H. Arami, A. Green, E. I. Solomon, S. X. Wang and S. S. Gambhir, Nat. Biomed. Eng., 2, 696, 2018.
36. S. Nazanin, S. Salari, A. Raza IET Nanobiotechnol., 11, 7, 883, 2017.
37. E. Catalano, A. Benedetto, Journal of Physics: Conference Series, 841, 1,2017.
38. S. Nigam, D. Bahadur, Nanomed. Nanotechnol. Biol. Med., 14, 759, 2018.

39. B. Dutta, N. G. Shetake, B. K. Barick, K. C. Barick, B. N. Pandey, K. I. Priyadarsini, P. A. Hassan, Colloids Surf. B Bio interfaces, 162, 163, 2018.
40. Q. Zhang, W. Shan, C. Ai, Z. Chen, T. Zhou, X. Lv, X. Zhou, S. Ye, L. Ren, X. Wang, Nanotheranostics, 2, 87, 2018.
41. M.W. Marashdeh , B. Ababneh, O. M. Lemine, A. Alsadig, K. Omri, L. El Mir, A. Sulieman, A., E. Mattar, Results Phys., 15, 102651, 2019.
42. M. Hjiri, M. Aida, G. Neri, Sensors, 19, 167, 2019.
43. H. Nosrati, M. Salehiabar, M. Fridoni, M. A. Abdollahifar, H. Kheiri Manjili, S. Davaran, H. Danafar, Sci. Rep., 9, 7173, 2019.
44. A. Allafchian, S. Hosseini, IET Nanobiotechnol., 13, 786, 2019.
45. I. Fernández-Barahona, M. Muñoz-Hernando, J. Ruiz-Cabello, F. Herranz, J. Pellico,. Inorganics, 8, 28, 2020.

45a. C. Wang, S. Wanzhu, R. Zhen, L. Xiaoxian B. Gu, R. Xiao, S. Wang, Nanoscale, 12, 795, 2020.

45b. D. Kim, H. Lee, S. Kwon, H. Choi, S. Park, Sensors and Actuators B: Chemical, 289, 65, 2019.

46. A. Nene, Y. Xuefeng, P. Kaithal, H. Luo, P. Somani, S. Ramakrishna, Materials, 13, 4644, 2020.
47. Z. Zhao, H. Cui, W. Song, X. Ru, W. Zhou, X. Yu, bioRxiv, 2020.

47a. D. Zhang, L. Huang, B. Liu, H. Ni, L. Sun, E. Su, H. Chen, Z. Gu , X. Zhao, Biosens. Bioelectron., 106, 204, 2018.

48. T. K. Vuongaf, T.T. Le, H. D. Do, X. T. Nguyen, T.T. Vu, L. D. Tran, Mater. Chem. Phys., 245, 122762, 2020.
49. S. Rosenfeldt, F. Mickoleit, C. Jörke, J. H. Clement, S. Markert, V. Jérôme, S. Schwarzinger, R. Freitag, D. Schüler, R. Uebe, Acta Biomater.,120, 293, 2021.
50. B. Cortés-Llanos, S. M. Ocampo, L. Cueva, G. F. Calvo, J. Belmonte-Beitia, L. Pérez, G. Salas, A. Ayuso-Sacido, Nanomaterials, 11, 2888, 2021.
51. S. Majeed, M. Danish, M.N. Ibrahim, J. Clust Sci,32, 1083, 2021.
52. C. Iacovita , I. Fizeșan , A. Pop ,L. Scorus , R. Dudric, G. Stiufiuc ,N. Vedeanu, R. Tetean, F. Loghin , R. Stiufiuc, Pharmaceutics., 12, 424, 2020.
53. G. Wei, Y. Wang, G. Yang, Y. Wang , R. Ju, Theranostics.,11, 63,2021.
54. N. Talebloo, M. Gudi, N. Robertson, P. Wang, J. Magn. Reson. Imaging, 51, 1659, 2020.
55. H. Mansouri ,E. Gholibegloo, T. Mortezazadeh, M. H. Yazdi ,F. Ashouri, R. Malekzadeh, A. Najafi, A. Foroumadi, M. A. Khoobi, Carbohydr. Polym., 254, 117262, 2021.

56. P. Y. You, F. C. Li, M. H. Liu, Y. H. Chan, ACS Appl. Mater. Interfaces, 11, 9841, 2019.
57. L. S. Ganapathe, M. A. Mohamed, R. M. Yunus, D. D. Berhanuddin, Magnetochemistry, 6, 68, 2020.
58. I. Muzahidul, M. Anik, K. Hossain, I. Hossain, A. M. Mahfuz, M. Rahman, I. Ahmed, Nano Select, 2, 1146, 2021.
59. P. Nimtrakul, D. B. Williams, W. Tiyaboonchai, C. A. Prestidge, Pharmaceuticals, 13, 121, 2020.
60. S. Deodhar, P. Rohilla, M. Manivannan, S. P. Thampi, M. G. Basavaraj, Langmuir, 36, 8100, 2020.
61. I. Ban, J. Stergar, U. Maver, Nanotechnol. Rev.,18, 7, 18, 2018.
62. P. Sangaiya, R. Jayaprakash, J Supercond Nov Magn., 31, 3397, 2018.
63. N. V. Srikanth Vallabani, S. Singh, Biotech, 8, 279, 2018.
64. M. G. Schneider, M. J. Martín, J. Otarola, E. Vakarelska, V. Simeonov, V. Lassalle, M. Nedyalkova, Pharmaceutics, 14, 204, 2022.
65. M. Kermanian, S. Sadighian, A. Ramazani, M. Naghibi, M. Khoshkam and P. Ghezelbash, ACS Biomater. Sci. Eng.,7, 2701, 2021.
66. C. Pucci, A. Degl'Innocenti, M. B. Gümüş, G. Ciofani, Biomater. Sci., 10, 2103, 2022.

Determination of Spectral Interference of Zirconium On Some Critical Analytes By CCD Based Inductively Coupled Plasma – Atomic Emission Spectrometric Technique

Vijayalaxmi C. Adya
Radiochemistry Division (Former)
Bhabha Atomic Research Centre, Mumbai, India
E-mail: vcadya@rediffmail.com

Received: 19.4.23, Revised: 28.4.23, 29.4.23; Accepted: 29.4.23

Abstract

Inductively coupled plasma atomic emission spectrometry (ICP-AES) is multi elemental, rapid, simple technique for the determination of trace level analytes, but suffers from spectral interference of matrix elements like U, Pu, Zr, Th etc. originating from their line rich emission spectra causing detrimental effect on the determination of analyte elements at trace levels in the nuclear materials. This can be overcome by using carrier distillation technique wherein carrier selectively distills analytes into D.C. arc-AES leaving behind the matrix into the electrode crater, being physical separation of the matrix. This technique is generally used to determine common metallic elements. For the determination of rare earth elements being refractory in nature like U, Th, etc. at sub-ppm levels, carrier distillation technique cannot be used. Hence, chemical separation of the matrix followed by their determination by AES technique is the usual practice, which may involve contamination of the sample during pre-treatment. Charged Coupled Detector (CCD) with flexibility of the choices of additional analytical lines of analytes, e.g., for Ce, 413.38 nm, 413.765 nm, 418.66 nm and 448.691 nm lines were selected and studied which may have lesser interference from Zr, facilitating direct determination of analytes at trace levels without any type of separation. Present paper involves the detailed study of spectral interference of zirconium on different analytical lines of Ba, Bi, Ce, Er, La, Lu, Mo, Nd, Pr, Sb, Sc, Ti, Tl, U, W, Y, Yb to select suitable analytical lines based on contributions of Zr on each analytical line, detection limits and sensitivity. Zirconium being major matrix, it's determination by ICP-AES was performed by identifying four suitable analytical lines, namely, 339.198 nm, 343.823 nm, 257.139 nm and 272.262 nm including monitoring of sensitivity, detection limits etc. Based on these interference studies,

DOI: 10.59143/isas.jisas.1.4.HKTW9530

it is possible to determine 17 analytes under investigations in Zr matrix on ppm basis by ICP-AES using their appropriate analytical lines without any chemical/physical separation.

Keywords Zirconium, Spectral interference, CCD based ICP-AES, Detection limits, Sensitivity

Introduction

In nuclear industry, the determination of trace metallic impurities is one of the important steps for chemical quality control of nuclear fuels and associated materials. To achieve desired burn-up, successful life span of the fuel in the reactor and also for smooth running of the reactor, it is essential to have stringent physical and chemical quality control and quality assurance measures for the nuclear materials. Some of the trace metal constituents in nuclear materials can affect its performance significantly due to their metallurgical and neutron absorption characteristics. The Inductively Coupled Plasma – Atomic Emission Spectrometric (AES) technique being simultaneous multi-elemental with acceptable analytical performance (detection limit, sensitivity, large linear dynamic range, etc.) is routinely used for the determination of trace metals in nuclear fuels and associated materials which forms an important and integral part of the chemical quality control at different stages of fuel fabrication.

The major matrix constituents in nuclear fuels, viz. U, Pu, Th and associated nuclear materials like graphite, etc. have rich emission spectra and hence it is essential to obtain trace elemental (analyte) spectrum devoid of interferences from that of U, Th and/or Pu, etc. The well-known established technique is D.C.arc -AES using carrier distillation method. In this technique the major matrix gets suppressed whereas the analytes are smoothly swept into the arc. Thus it is a direct technique, with minimum chances of contamination owing to less sample handling. However the technique offers poor precision. This technique is used for the determination of analytes with reasonable specification limits [1-6]. ICP-AES technique is generally used for the determination of rare earth elements after chemical separation of the matrix to achieve sub-ppm levels of specification limits for analytes by preconcentration as they cannot be determined directly by feeding higher amounts of the matrix solution due to the less tolerance of solid material which can be fed into the plasma causing chocking of the nebuliser. Hence in this method there are chances of contamination of the sample but has superior detection limits and precision than D.C. arc – AES carrier distillation technique. In ICP-AES, a suitable extractant and feed conditioning are required resulting in preferential extraction of the major matrix without loss of the analytes even at trace levels [7-12]. Therefore,

a method needs to be developed where sample handling is minimum and the analytical performance of the method (precision, detection limits, linear dynamic range, sensitivity, etc.) is superior. In our previous study, an attempt was made to understand the spectral interference of Uranium on other analytes using CCD-based ICP-AES [13-15].

Zirconium finds its applications in nuclear industry as a cladding material, while U-Zr, U-Pu-Zr, Zr-Nb and binary and ternary alloy materials are useful as nuclear fuels. This is mainly due to its many unique characteristics such as low thermal neutron absorption cross section (0.18barn), have good mechanical properties and corrosion resistance. In order to become suitable as nuclear material, one of the criteria is to conform to trace metal impurities as per the specifications laid down by fuel designer [16-22]. Using D.C. arc-AES technique based on carrier-distillation method, we have reported determination of trace common metallic elements in Zr matrix without chemical separation [23-25]. In U-Zr and Zr-Nb alloys, trace metals were reported after chemical separation by ICP-AES [26-27]. Owing to multi-electronic configuration of Zr has rich emission line spectra, which might cause spectral interference on analytes thereby leading to higher limits of detection. In order to achieve lower detection limits especially in case of rare earths, it becomes inevitable to perform chemical separation of Zr prior to determination of trace metallic elements by ICP-AES technique along with common metallic elements. In this process, it was observed that the presence of Zr even at micro-gram levels may cause spectral interference on analytes leading to their in-accurate determinations. Hence it was essential to understand Zr contributions on various emission lines for analytes in detail. Using CCD-based ICP-AES technique, we have reported the spectral interference of Zr on some of the critical common analytes and rare earths [28-29].

The present study is the continuation of the previous work, wherein some more elements, namely, Ce, Nd, Lu, Pr, Er, Y, U, Ba, Bi, Tl, Yb, La, Mo, Sb, W, Sc and Ti have been studied in detail for their determination using charged coupled device (CCD) based detector without any physical or chemical separation from major matrix zirconium [30]. This detector offers choice of additional analytical lines, free from the major matrix, which were explored and identified. These analytes with interference free emission lines from Zr can be used for their direct determinations on ppm basis using 1mg/ml of Zr sample solution by ICP-AES depending upon the specification limits requirements for these trace elements. This necessitated determination of Zr by using suitable analytical lines and it’s quantification to

understand it's tolerance on each analyte under study including analytical performances (detection limits, sensitivity etc.) for the identified lines.

Experimental Details

Instrument

An atomic emission spectrometer instrument Spectro Arcos procured from Germany having dual excitation sources, ICP as well as D.C. arc was used, the details for which are mentioned elsewhere [28-29]. Also, the main features of this unit being that it is provided with charged coupled detectors with which one can choose suitable additional analytical lines during study.

Reagents and standard solutions

CertiPUR® ICP multi standard solutions (E-Merck, Darmstadt, Germany) at 1 mg/ml were used for the preparation of solutions of rare earth, common metallic elements in the range of 0.05 μg/ml-20 μg/ml and for Zr in the range of 0.05 μg/ml -1000 μg/ml were prepared by suitable dilutions with supra-pure 0.5M HNO_3. Appropriate amount of nuclear grade U_3O_8 received from NFC was dissolved in minimum amount of concentrated HNO_3 and was made up in 4M HNO_3 to get 10 mg/ml U stock solution. From this, U standards were prepared in the range of 0.05 - 20 μg/ml in 0.5M HNO_3. Multi-point standardization was carried out using 0.5M HNO_3 as lower standard and 0.05 μg/mL - 5 μg/mL of the corresponding higher elemental standard for various analytes and for Zr in the concentration range of 0.05 μg/mL - 1000 μg/mL after proper peak search using 20 μg/mL of each analyte separately. For all the analytes including Zr, calibration plots were obtained. Blank correction was carried out using 0.5M HNO_3.

Results and Discussion

The entire study has been classified into four categories, which is discussed below:

(a)Determination of Zirconium by ICP-AES

In order to understand the extent of interference from Zr on each analyte, quantification of the same was essential. Hence the calibration curves for Zr using four analytical lines, namely, 339.198 nm, 343.823 nm, 257.139 nm, and 272.262 nm were obtained which are shown in Fig.1 . It was found that except for Zr-339.198 nm, the upper limit of detection for Zr is 200 μg/mL, while Zr- 343.823 nm, Zr-257.139 nm, and Zr-272.262 nm lines can be used for their determinations up to 1000 μg/mL with less than 5% RSD (Relative Standard Deviation). The

detection limits for these analytical lines of Zr were found to be 0.02 μg/mL, 0.09 μg/mL, 0.34 μg/mL and 0.12 μg/mL respectively. Based on the analytical performances, namely, detection limits, sensitivity, the emission line of Zr at 343.823 nm was found to be the best for its determination.

(b)Identification of analytical lines for elements under study free from spectral interference of zirconium

From the directory of the wavelength tables provided within the instrument, the best analytical lines which can be considered for the determination of analytes were identified and are shown in Table 1.

(c) Contributions of Zr on various analytical lines for the analytes and the performance of the analytes

Spectral interference of Zr on various analytes

In ICP-AES, the spectral interference is quite significant which is mainly due to various transitions of the complex matrix system. Generally, to determine an analyte at trace levels, the most sensitive line is chosen for analysis. But, if this line is overlapped by some other interfering line leading to erroneous estimates for analyte, one needs to select another line which may be less sensitive and with poorer detection limits but will give accurate determination for the analyte. Two analytical lines cannot be resolved in mainly two situations: (a) when the resolution of the instrument is poor and (b) when there is overlap between the two analytical channels which can never be separated regardless of the best resolution used in the instrument. In the first case, an instrument with better resolution can solve the problem while for the 2nd case the spectral interference needs to be studied and the correction factor evaluated, or otherwise one needs to choose alternative analytical lines for their determination. Improvement of the resolution of the instrument may resolve the lines only if the optics are responsible for the spectral overlap. If overlap of the lines is from a broadening process in the plasma, improvement of the instrumental resolution will be inefficient. Therefore, alternative emission lines were needed to be investigated for analytical applicability. In some cases, it may happen that only the analytical line free from spectral interference needs to be chosen. If this is the case, appropriate correction factors need to be evaluated. Due to the advancement of the CCD detector (i.e., array of pixels) and the ability to choose an alternate analytical line, this lessens spectral interference.

In Table 2A and Table 2B, the contributions of 1000 μg/mL of Zr on the analytical lines of all the elements under study including sensitivity and detection limits in presence of Zr matrix have been presented. These contributions of Zr using 1000 μg/mL of Zr were recorded at the blank levels for each analyte having many analytical lines (0.5M HNO_3). It was observed that the spectral interference of Zr on various analytical lines was found to increase linearly with Zr concentrations. Also, the choice of the best analytical line for analytes was based mainly on the extent of contribution from Zr at 1000 microgram /mL level followed by it's detection limit.

Accordingly, a detailed study was carried out to choose the appropriate emission line/s for the trace determinations of 17 analytes in the presence of Zr matrix which is discussed in detail below:

Ba (Barium)

Three lines of Ba namely, 230.424 nm, 233.527 nm, 455.404 nm were studied. Amongst these three lines, Ba 233.527 nm analytical line was found to be the best with respect to detection limit and practically no spectral interference, while Ba 455.404 nm analytical line showed detection limit comparable with the best line and having moderate spectral interference from Zr which can be overcome using correction factor mentioned. Ba 230.424 nm was found to have severe spectral interference with 100 times poor detection limit than the best line and hence should not be used.

Bi (Bismuth)

For Bi, six analytical lines namely, Bi 143.683 nm, 153.317 nm, 190.241 nm, 222.825 nm, 223.061 nm and Bi 306.772 nm were studied. Amongst these six lines, Bi 223.061 nm analytical line was the best requiring moderate correction factor, while Bi 306.772 nm was also found to be useful with detection limit 100 times higher than the best line, to be used after incorporating moderate correction factor. The remaining four lines of Bi 143.683 nm, Bi 153.317 nm, Bi190.241nm and Bi 222.825 nm cannot be used due to severe spectral interferences from Zr.

Ce (Cerium)

For Ce, four analytical lines, namely, Ce 413.38 nm, Ce 413.765 nm, Ce 418.66 nm and Ce 448.691 nm were investigated. Ce 413.765 nm was found to be the best analytical line with negligible correction factor, while Ce 413.38 nm line was found to be the next most suitable

line with detection limit comparable with the best line but requires moderate correction factor. Ce 448.691 nm and Ce 418.66 nm lines showed severe spectral interferences from Zr; hence both the lines cannot be used for analysis.

Er (Erbium)

Amongst the four lines of Er, namely, Er 323.058 nm, Er 326.478 nm, Er 337.271 nm and Er 349.91 nm, the best analytical line was found to be Er 337.271 nm with negligible correction factor while two analytical lines, Er 323.058 nm and Er 349.91 nm were also found to be useful with moderate correction factors and detection limits ten times higher than the best line. Er 326.478 nm showed significant spectral interference from Zr and hence cannot be used.

La (Lanthanum)

For La, three analytical lines namely, La 333.749 nm, La 379.478 nm and La 408.672 nm were studied. La 379.478 nm line was found to be the best analytical line with negligible correction factor, while La 333.749 nm showed detection limit comparable with the best line and moderate correction factor. La 408.672 nm with detection limit ten times higher than the best line, required negligible correction factor. Thus, all three analytical lines of La are useful for analysis.

Lu (Lutetium)

For Lu, four analytical lines namely, Lu 219.554 nm, Lu 261.542 nm, Lu 291.139 nm and Lu 307.76 nm were studied. All these lines can be used for the analysis with negligible correction factor, the best being Lu 261.542 nm line. Lu 291.139 nm, Lu 307.76 nm have detection limits ten times higher than the best line while Lu 219.554 nm has detection limit hundred times higher than the best line.

Mo (Molybdenum)

For Mo, four analytical lines, namely, Mo 202.095 nm, Mo 203.909 nm, Mo 204.664 nm and Mo 281.615 nm were studied. Amongst these lines, Mo 202.095 nm and Mo 281.615 nm were found to be the best analytical lines with lowest detection limits and negligible spectral interferences from Zr and hence does not require any correction factors for analysis. Remaining two lines, Mo 203.909 nm and Mo 204.664 nm were also found to be equally suitable lines with detection limits comparable to the best lines and showed negligible spectral interferences from Zr and hence does not require any correction factor for analysis.

Nd (Neodynium)

For Nd, four analytical lines, namely, Nd 401.225 nm, Nd 406.109 nm, Nd 417.73 nm and Nd 430.358 nm were investigated. Nd 406.109 nm and Nd 430.358 nm were found to be the best and equally good analytical lines with incorporation of moderate correction factors for

analysis. Nd 417.73 nm line was also found to be good with detection limits ten times higher than the best line required to use moderate correction factor. Nd 401.225 nm line cannot be used due to significant spectral interferences from Zr.

Pr (Praseodynium)

For Pr, two analytical lines, Pr 411.846 nm and Pr 414.311 nm were found to be useful. The best line was Pr 411.846 nm with negligible correction factor, while Pr 414.311 nm had detection limit comparable with the best line but requires moderate correction factor for analysis.

Sb (Antimony)

For Sb, three analytical lines, Sb 181.115 nm, Sb 206.833 nm and Sb 217.581 nm were investigated. Amongst these, Sb 206.833 nm analytical line was found to be the best with moderate correction factor, whereas Sb 217.581 nm was found to have detection limit comparable with the best line requiring moderate correction factor for analysis. Sb 181.115 nm showed detection limit ten times higher than the best line and can be determined after incorporating moderate correction factor.

Sc (Scandium)

For Sc, four analytical lines, namely, Sc 335.373 nm, Sc 356.770 nm, Sc 361.384 nm and Sc 424.683 nm were studied. Amongst these four lines, Sc 424.683 nm was found to be the best analytical line having very much insignificant spectral interference from Zr, hence can be used directly without the need for any correction factor. The next two useful lines were Sc 335.373 nm and Sc 361.384 nm with detection limits comparable with the best line but as there was no spectral interferences from Zr was observed, can be used directly for determination without incorporating correction factors. Sc 356.770 nm line showed the detection limit 100 times higher than the best line and requires moderate correction factor for the analysis of Sc.

Ti (Titanium)

For Ti, two useful analytical lines, Ti 334.187 nm and Ti 336.121 nm were studied and were found to be equally useful for analysis due to good detection limits and requiring negligible correction factor to take care of interference from Zr for analysis.

Tl (Thalium)

For Tl, two analytical lines, namely, Tl 190.864 nm and Tl 276.787 nm were studied. Tl 190.864 nm was found to be the best analytical line with moderate correction factor required to be used for analysis. Tl 276.787 nm with detection limit 30 times higher than the best line with significant spectral interference from Zr, cannot be used for analysis.

U (Uranium)

For U, four analytical lines, namely, U 279.394 nm, U 367.007 nm, U 385.958 nm and U 409.014 nm were studied. U 385.958 nm was observed to be the best line which can be used after incorporating moderate correction factor. U 279.394 nm and U 367.007 nm were found to have detection limits comparable with the best line but have significant spectral interferences from Zr hence, can be used after incorporating the correction factors for the analysis of U. U 409.014 nm showed severe spectral interferences due to Zr, hence cannot be used.

W (Tungsten)

For W, four analytical lines, namely, W 207.911 nm, W 220.448 nm, W 224.875 nm and W 239.709 nm were studied. Both the analytical lines for W, namely, W 207.911 nm and W 224.875 nm were found to be useful with good, comparable detection limits with negligible spectral interference from Zr and hence does not require any correction factor for analysis. W 220.448 nm and W 239.709 nm were found to have detection limits comparable with the best line but due to contributions from spectral interferences of Zr, requires moderate correction factor for the analysis.

Y (Yttrium)

For Y, eight analytical lines, namely, Y 224.306 nm, Y 320.332 nm, Y 324.228 nm, Y 360.073 nm, Y 362.871 nm, Y 371.030 nm, Y 377.433 nm and Y 442.259 nm were studied. Amongst these, Y 377.433 nm line was found to be the best analytical line with negligible spectral interference from Zr and hence does not require to incorporate any correction factor for analysis. The next suitable analytical lines being Y 320.332 nm, Y 360.073 nm and Y 371.030 nm with negligible spectral interferences from Zr and hence does not require any correction factors. In the context of detection limits, Y 360.073 nm showed detection limit being comparable with the best line while for Y 320.332 nm and Y 371.030 nm, the detection limits were ten times higher than the best line; all the three lines have negligible spectral interferences for Zr which can be used directly for analysis. For Y 224.306 nm, Y 324.228 nm, Y 362.871 nm and Y 442.259 nm, the detection limits were ten times higher than the best line and showed moderate spectral interferences due to Zr which can be rectified using appropriate correction factors.

Yb (Ytterbium)

For Yb, four analytical lines, namely, Yb 222.446 nm, Yb 289.138 nm, Yb 328.937 nm and Yb 369.419 nm were studied. Yb 328.937 nm line was found to be the best analytical line with negligible spectral interference and hence does not require any correction factor for analysis. Yb 222.446 nm, Yb 289.138 nm and Yb 369.419 nm were also found to have

negligible spectral interferences from Zr with detection limits comparable with the best line except for Yb 222.446 nm which has detection limits ten times higher than the best line.

The above discussions on the effect of Zr on various analytical lines of elements under study leads to three main scenarios: (1) significant contribution from Zr matrix– the line cannot be used for analytical purpose; (2) insignificant contribution from Zr matrix – the line is suitable for its analytical application without any correction factor; (3) moderate contribution from Zr matrix – the line can be used for analytical purposes but needs to incorporate appropriate correction factor. In Table 3, the comparison of the spectral interference of Zr on different analytical lines of the elements mentioned earlier and their analytical performance including the most suitable analytical lines which can be selected for analytical purposes for the determination of analytes in presence of Zr matrix without physical or chemical separation have been presented.

(d)Finalizing best analytical lines for analytes for their direct determinations in presence of zirconium without chemical and/or physical separation on ppm basis.

In Table 4, the analytical results for the direct determination of the analytes under study on ppm (μg/g) basis have been shown based on better detection limits and negligible interference from Zr requiring negligible correction factor for their determinations. Depending upon the specification limits being led down by the sample providing agency, it is possible to get the results just by aspirating 1 mg/ml of the Zr sample solution into ICP using appropriate wavelengths for the analytes mentioned therein on ppm basis, thus providing simple method for the direct determination of analytes in actual zirconium samples using CCD based ICP-AES technique.

Conclusions

A systematic study was carried out to understand the spectral interference of zirconium on 17 trace metals (Ba, Bi, Ce, Er, La, Lu, Mo, Nd, Pr, Sb, Sc, Ti, Tl, U, W, Y, Yb) in Zr matrix, crucial from the viewpoint of requirements in nuclear industry using CCD based ICP-AES technique. The most suitable analytical lines for various elements after detailed studies have been mentioned in Table 4. Also, for all the analytes, sensitivity, detection limits and the tolerance limits of Zr on these analytes were recorded. This data was used to identify additional analytical lines for the determinations of trace metals. The present method also

included the determination of Zr by ICP-AES technique in the range of 0.05 μg/mL to 1000 μg/mL using 257.139 nm, 272.262 nm, 339.198 nm and 343.828 nm, analytical lines of Zr which were suitable, except for 339.198 nm which gets saturated at 200 μg/mL. Based on the calibration curves, detection limits for Zr were found to be 0.34 μg/ml, 0.12 μg/ml, 0.02 μg/mL and 0.09 μg/ml respectively. These studies are helpful in arriving at accurate determinations of trace metals studied in presence of zirconium up to 1000 μg of zirconium on ppm (μg/g) basis for actual samples directly without any separation steps.

Acknowledgement:

The author acknowledges the constant support and encouragements from Dr. P.K. Mohapatra, Head, Radiochemistry Division; Associate Director, Radiochemistry and Isotope Group and also to Dr. S. Kannan, Group Director, Radiochemistry and Isotope group, Bhabha Atomic Research Centre, Mumbai.

Figure:

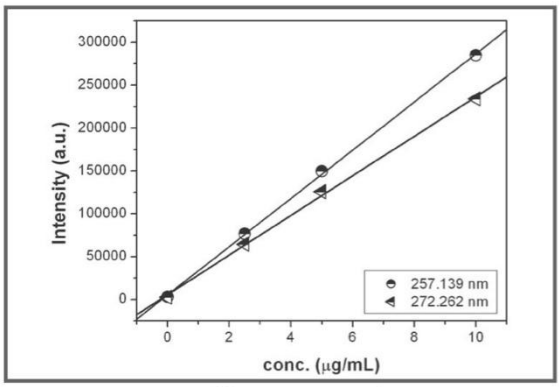

Fig. 1(A). Calibration curves for Zr : 257.139 nm and 272.262 nm.

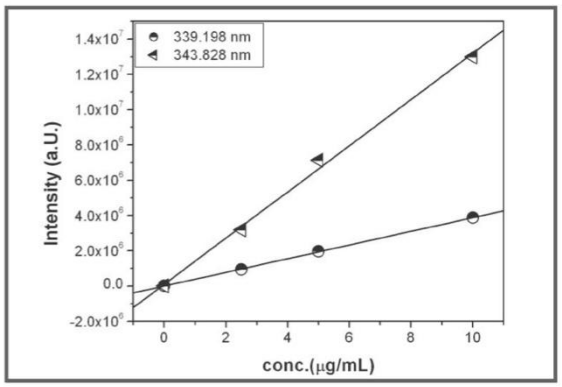

Fig. 1(B). Calibration curves for Zr : 339.198 nm and 343.828 nm.

Tables:

TABLE 1: Interference free lines for analytes in Zr matrix

Element	Analytical Line (nm)
Ba	233.527
Bi	223.061
Ce	413.765
Er	337.271
La	379.478
Lu	261.542
Mo	202.095, 281.615
Nd	406.109
Pr	411.846
Sb	206.833

Sc	424.683
Ti	336.121
Tl	190.864
U	385.958
W	207.911
Y	377.433
Yb	328.937

TABLE 2A: Spectral interference of Zirconium on various analytes

Element	Anal. Line(nm)	Contribution (µg/mL)	Correction factor	Detection Limit (µg/mL)	Sensitivity (Counts/ µg/mL)
	230.424	>17.8	NA	$6.031x10^{-1}$	0.014587
Ba	233.527	0.019	$1.9x10^{-5}$	$1.472x10^{-3}$	$1.775x10^{-5}$
	455.404	0.238	$2.38x10^{-4}$	$1.015x10^{-3}$	$2.4172x10^{-5}$
Bi	143.683	> 10.527	NA	$4.76x10^{-1}$	0.01917
	153.317	> 41.262	NA	1.808	0.075808
	190.241	5.194	$5.194x10^{-3}$	$1.781 x10^{-1}$	0.0018522
	222.825	1.826	$1.826x10^{-3}$	$7.159 x10^{-2}$	0.001356
	223.061	0.194	$1.94x10^{-4}$	$5.227 x10^{-3}$	0.00015129
	306.772	0.343	$3.43x10^{-4}$	$1.306 x10^{-1}$	$9.7139x10^{-5}$
Ce	413.380	0.747	$7.47x10^{-4}$	$6.523 x10^{-3}$	$3.8528x10^{-5}$
	413.765	0.085	$8.5x10^{-5}$	$3.573 x10^{-3}$	$3.9952x10^{-5}$
	418.66	> 22.712	NA	$4.895 x10^{-3}$	$4.0382x10^{-5}$
	448.691	2.466	$2.466x10^{-3}$	$7.605 x10^{-2}$	0.00077383
Er	323.058	0.197	$1.97x10^{-4}$	$1.333 x10^{-3}$	$4.5941x10^{-5}$
	326.478	8.946	$8.946x10^{-3}$	$5.669 x10^{-4}$	$9.9324x10^{-6}$
	337.271	0.042	$4.2x10^{-5}$	$1.592 x10^{-3}$	$3.7098x10^{-6}$
	349.910	0.642	$6.45x10^{-4}$	$1.45 x10^{-3}$	$1.3441x10^{-5}$
La	333.749	0.116	$1.16x10^{-4}$	$1.408 x10^{-3}$	$6.9697x10^{-6}$
	379.478	0.045	$4.5x10^{-5}$	$1.608 x10^{-3}$	$8.2075x10^{-6}$
	408.672	0.049	$4.9x10^{-5}$	$2.664 x10^{-4}$	$9.8999x10^{-6}$
Lu	219.554	0.034	$3.4x10^{-5}$	$1.507 x10^{-3}$	$3.0806x10^{-5}$
	261.542	0.004	$4x10^{-6}$	$4.779x10^{-5}$	$1.4908x10^{-6}$
	291.139	0.028	$2.8x10^{-5}$	$9.035 x10^{-4}$	$1.3165x10^{-5}$
	307.760	0.016	$1.6x10^{-5}$	$2.952 x10^{-4}$	$7.906x10^{-6}$
Mo	202.095	0.024	$2.4x10^{-5}$	$3.079 x10^{-3}$	1.9838E-005
	203.909	0.044	$4.4x10^{-5}$	$4.141 x10^{-3}$	3.8155E-005
	204.664	0.069	$6.9x10^{-5}$	$2 x10^{-3}$	5.4118E-005
	281.615	0.046	$4.6x10^{-5}$	$6.747 x10^{-4}$	2.9765E-005

Nd	401.225	2.075	$2.075x10^{-3}$	$4.601 x10^{-3}$	2.7236E-005
	406.109	0.2	$2x10^{-4}$	$3.702 x10^{-3}$	3.984E-005
	417.731	0.254	$2.54x10^{-4}$	$1.561 x10^{-2}$	4.6427E-005
	430.358	0.24	$2.4x10^{-4}$	$7.256 x10^{-3}$	3.2077E-005
Pr	411.846	0.064	$6.4x10^{-5}$	$5.511 x10^{-3}$	3.3374E-005
	414.311	0.184	$1.84x10^{-4}$	$2.978 x10^{-3}$	2.3725E-005

NA – Not applicable

TABLE 2B: Detection limits and sensitivity for various emission lines of analytes

Element	Wavelength (nm)	Contribution (µg/mL)	Correction factor	Detection Limit (µg/mL)	Sensitivity (Counts/ µg/mL)
Sb	187.115	0.349	$3.49x10^{-4}$	$1.803 x10^{-2}$	0.00036385
	206.833	0.143	$1.43x10^{-4}$	$5.697 x10^{-3}$	0.00014288
	217.581	0.39	$3.9x10^{-4}$	0.007853	0.00011591
Sc	335.373	0.047	$4.7x10^{-5}$	0.0002637	9.2255E-007
	356.770	0.12	$1.2x10^{-4}$	0.01793	6.0168E-006
	361.384	0.091	$9.1x10^{-5}$	0.0001354	8.5068E-007
	424.683	0.004	$4x10^{-6}$	0.0002889	9.585E-007
Ti	334.187	0.046	$4.6x10^{-5}$	0.004604	5.6556E-006
	336.121	0.043	$4.3x10^{-5}$	0.001748	1.6637E-006
Tl	190.864	0.443	$4.43x10^{-4}$	0.027	848
	276.787	3.588	$3.588x10^{-3}$	0.83	27
U	279.394	1.218	$1.218x10^{-3}$	0.02528	0.00085538
	367.007	2.684	$2.684x10^{-3}$	0.00514	0.00025145
	385.958	0.278	$2.78x10^{-4}$	0.01497	0.00016145
	409.014	10.645	$10.645x10^{-2}$	0.02018	0.00020043
W	207.911	0.061	$6.1x10^{-5}$	0.003288	7.805E-005
	220.448	0.107	$1.07x10^{-4}$	0.007447	0.00012411
	224.875	0.085	$8.5x10^{-5}$	0.006307	6.6452E-005
	239.709	0.108	$1.08x10^{-4}$	0.003162	7.2284E-005
Y	224.306	0.146	$1.46x10^{-4}$	0.007314	5.4535E-005
	320.332	0.05	$5x10^{-5}$	0.001759	5.8651E-006
	324.228	0.187	$1.87x10^{-4}$	6.811E-005	2.5883E-006
	360.073	0.087	$8.7x10^{-5}$	0.0002023	3.1694E-006
	362.871	0.209	$2.09x10^{-4}$	0.002476	2.9604E-005
	371.030	0.061	$6.1x10^{-5}$	9.471E-005	1.4163E-006
	377.433	0.027	$2.7x10^{-5}$	0.0006185	2.2761E-006
	442.259	0.104	$1.04x10^{-4}$	0.006534	4.0566E-005

Yb	222.446	0.042	$4.2x10^{-5}$	0.001962	2.5171E-005
	289.138	0.022	$2.2x10^{-5}$	0.0003137	7.7288E-006
	328.937	0.015	$1.5x10^{-5}$	0.0001766	5.13E-007
	369.419	0.023	$2.3x10^{-5}$	0.0001183	1.7341E-006

NA – Not applicable

TABLE 3: Comparison of types of spectral interference and analytical performance of various analytical lines for the elements under study

Element	**Anal. Line (nm)**	**Level of spectral interference**	**Analytical Performance**
Ba	230.424	Bad line, should not be used	D.L. 100 times higher than best line
	233.527	Negligible (correction factor not required)	Best
	455.404	Moderate (correction factor required)	D.L. comparable with best line
Bi	143.683	Bad line, should not be used	D.L. 100 times higher than best line
	153.317	Worst line, should not be used	D.L. 1000 times higher than best line
	190.241	Significant, should not be used	D.L. 100 times higher than best line
	222.825	Significant, should not be used	D.L. 10 times higher than best line
	223.061	Moderate (correction factor required)	Best
	306.772	Moderate (correction factor required)	D.L. 100 times higher than best line
Ce	413.38	Moderate (correction factor required)	D.L. comparable with best line
	413.765	Negligible (correction factor not required)	Best
	418.66	Bad line, should not be used	D.L. comparable with best line
	448.691	Significant, should not be used	D.L. 10 times higher than best line
Er	323.058	Moderate (correction factor required)	D.L. 10 times higher than best line
	326.478	Significant, should not be used	D.L. 10 times higher than best line
	337.271	Negligible (correction factor not required)	Best
	349.91	Moderate (correction factor required)	D.L. 10 times higher than best line
La	333.749	Moderate (correction factor required)	D.L. comparable with best line
	379.478	Negligible (correction factor not required)	D.L. 10 times higher than best line

	408.672	Negligible (correction factor not required)	Best
Lu	219.554	Negligible (correction factor not required)	D.L. 100 times higher than best line
	261.542	Negligible (correction factor not required)	Best
	291.139	Negligible (correction factor not required)	D.L. 10 times higher than best line
	307.76	Negligible (correction factor not required)	D.L. 10 times higher than best line
Mo	202.095	Negligible (correction factor not required)	D.L. 10 times higher than best line
	203.909	Negligible (correction factor not required)	D.L. 10 times higher than best line
	204.664	Negligible (correction factor not required)	D.L. 10 times higher than best line
	281.615	Negligible (correction factor not required)	Best
Nd	401.225	Significant, should not be used	D.L. comparable with best line
	406.109	Moderate (correction factor required)	Best
	417.73	Moderate (correction factor required)	D.L. 10 times higher than best line
	430.358	Moderate (correction factor required)	D.L. comparable with best line
Pr	411.846	Negligible (correction factor not required)	Best
	414.311	Moderate (correction factor required)	D.L. comparable with best line
Sb	187.115	Moderate (correction factor required)	D.L. 10 times higher than best line
	206.833	Moderate (correction factor required)	Best
	217.581	Moderate (correction factor required)	D.L. comparable with best line
Sc	335.373	Negligible (correction factor not required)	D.L. comparable with best line
	356.770	Moderate (correction factor required)	D.L. 100 times higher than best line
	361.384	Negligible (correction factor not required)	D.L. comparable with best line
	424.683	Very much insignificant, correction factor not required	Best
Ti	334.187	Negligible (correction factor not required)	D.L. comparable with best line

	336.121	Negligible (correction factor not required)	Best
Tl	190.864	Moderate (correction factor required)	Best
	276.787	Significant, should not be used	D.L. 30 times higher than the best line
U	279.394	Significant (to be used after incorporating correction factor)	D.L. comparable with best line
	367.007	Significant (to be used after incorporating correction factor)	D.L. comparable with best line
	385.958	Moderate (correction factor required)	Best
	409.014	Major (cannot be used)	D.L. comparable with best line
W	207.911	Negligible (correction factor not required)	Best
	220.448	Moderate (correction factor required)	D.L. comparable with best line
	224.875	Negligible (correction factor not required)	D.L. comparable with best line
	239.709	Moderate (correction factor required)	D.L. comparable with best line
Y	224.306	Moderate (correction factor required)	D.L. 10 times higher than best line
	320.332	Negligible (correction factor not required)	D.L. 10 times higher than best line
	324.228	Moderate (correction factor required)	D.L. 10 times higher than best line
	349.609	Worst line, should not be used	D.L. 10 times higher than best line
	360.073	Negligible (correction factor not required)	Best
	362.871	Moderate (correction factor required)	D.L. 10 times higher than best line
	371.030	Negligible (correction factor not required)	D.L. 10 times higher than best line
	377.433	Negligible (correction factor not required)	D.L. comparable with the best line
	442.259	Moderate (correction factor required)	D.L. 10 times higher than best line
Yb	222.446	Negligible (correction factor not required)	D.L. 10 times higher than best line
	289.138	Negligible (correction factor not required)	Good and comparable with best line
	328.937	Negligible (correction factor not required)	Good and comparable with best line
	369.419	Negligible (correction factor not required)	Best

TABLE 4: Detection limits for various analytes on ppm (μg/g) basis

Element	Wavelength (nm)	Detection Limit (μg/g)
Ba	233.527	1.5
Bi	223.061	5.23
Ce	413.765	3.57
Er	337.271	1.6
La	408.672	0.27
Lu	261.542	0.048
Mo	281.615	0.68
Nd	406.109	3.70
Pr	411.846	5.51
Sb	206.833	5.7
Sc	424.683	0.3
Ti	336.121	1.75
Tl	190.864	27
U	385.958	15
W	207.911	3.3
Y	360.073	0.20
Yb	369.419	0.12

REFERENCES

1. Bourdon F. Scribner and Harold R. Mullin: Journal of research of the National Bureau of Standards, RP 1753, 37, 379, 1946.
2. J. Mika, T. Torak, Analytical emission spectroscopy, fundamentals Ed. By the utterworth Group, London 1974.
3. A.G. Page, S.V. Godbole, Madhuri J. Kulkarni, S.S. Shelar, B.D. Joshi Fresenius Z. Anal. Chem. 297, 388, 1979.
4. M.K. Bhide, Vijayalaxmi R. Bhandiwad, Mithilesh Kumar, A.G.I. Dalvi and M.D. Sastry, Radiochemistry Division, BARC Report -1355 ,1987.
5. T.R. Bangia, V.C. Adya, B.A. Dhawale, B. Rajeswari, M.D. Sastry and P.R. Natarajan Analytical Letters 23(1), 147, 1990.
6. T.R. Bangia, B.A. Dhawale, V.C. Adya and M.D. Sastry , Fresenius Z. Anal. Chem. 332, 802, 1988.
7. A. Sengupta, M. J. Kulkarni, S. V. Godbole, J Radioanal. Nucl. Chem, 289, 3, 961, 2011.
8. Arijit Sengupta, M.J. Kulkarni, S.V. Godbole, V. Natarajan, and P.N. Pathak, Atomic Spectroscopy, 35(2), 60, March/April 2014.

9. A. Sengupta, V.C. Adya, Mithlesh Kumar, S.K. Thulasidas, S.V. Godbole and V.K.Manchanda, Atomic Spectroscopy 32(2), 49, March/April 2011.
10. S.K. Thulasidas, V.C. Adya, T.K. Seshagiri, Mithlesh Kumar, M.K. Bhide and S.V. Godbole, Atomic Spectroscopy 33(5), 158, September/October 2012.
11. A. Sengupta, B. Rajeswari, V.C. Adya and R.M. Kadam, Atomic Spectroscopy, 4, 127, July/August 2019.
12. V.C. Adya, Arijit Sengupta, Sudipta Chakraborty, K. Vimalnath and S.K. Thulasidas, J. ISAS, 1(2), 58, Oct.'22.
13. A. Sengupta, V.C. Adya and S.V. Godbole, J. Radioanal. Nucl. Chem. 298, 1117, 2013.
14. A.Sengupta, V.C. Adya, T.K. Seshagiri and S.V. Godbole, Atomic Spectroscopy, 34(2), 53, March/April 2013.
15. A. Sengupta and V.C. Adya, J. Radioanal. Nucl. Chem. 299, 2023, 2014.
16. Michiko Banno, Eiichi Tamiya, Yuzura Takamura, Analytica Chimica Acta 634(2), 153, 23 Feb. 2009.
17. Xiaoguo Ma, Yibing Li , Anal. Chim. Acta 579, 47, 2006.
18. G. Radha Krishnan, H.R. Ravindra, B. Gopalan, S. Syamsunder, Anal. Chim. Acta 309, 333, 1995.
19. Raparthi Shekhar, J. Arunachalam, G. Radha Krishna, H.R. Ravindra, B. Gopalan, Journal of Nuclear Materials 340 (2-3), 284, 15 April 2005.
20. Tasaku Akagi, Yukihiro Nojiri, Masahiro Matsui, and Hiroki Haraguchi, Applied Spectroscopy 39(4), 662, 1985.
21. Dirk Merten, Jose A.C. Broekaert, Rolf Brandt and Norbert Jakubowski, Jl. Anal. At. Spectrom. 14, 1093, 1999.
22. Amol D. Shinde, Raghunath Acharya and Annareddy V.R. Reddy, Nuclear Engineering and Technology 49, 562, 2017.
23. Nimai Pathak, V.C. Adya, S.K. Thulasidas, Arijit Sengupta, T.K. Seshagiri and S.V. Godbole, Atomic Spectroscopy 35(1), 17, Jan./Feb. 2014.
24. [24] B. Rajeswari, V.C. Adya, S. Pathak, Sk. Jayabun, N. Pathak, M. Mohapatra and R.M. Kadam 14th Biennial DAE-BRNS Symposium on Nuclear and Radiochemistry (NUCAR-2019), Jan. 15-19, BARC, Mumbai; B-24, 35, 2019.
25. B. Rajeswari, S. Pathak, Sk. Jayabun, N. Pathak, M. Mohapatra, Arijit Sengupta, and R.M. Kadam, At Spectroc., 40(6), 221, 2019.

26. A. Sengupta, B. Rajeswari, R.M. Kadam, S.V. Godbole, Atomic Spectroscopy, 33(2), 48, 2012.
27. S. Pathak and A. Sengupta, Atomic Spectroscopy 38(6), 174, Nov./Dec. 2017.
28. A. Sengupta and V.C. Adya, Atomic Spectroscopy 34(6), 207, Nov./Dec. 2013.
29. V.C. Adya**,** Arijit Sengupta and S.V. Godbole, Atomic Spectroscopy 34(6), 25-32, Jan./Feb. 2014.
30. V.C. Adya, Arijit Sengupta, S.K. Thulasidas and V. Natarajan , Proceedings of the BRNS-AEACI first symposium `Current Trends in Analytical Chemistry' (CTAC-2015) Conference paper, 2015.